Modulated Surface Texturing on Temporary Aluminium Substrate for Flexible Thin-Film Solar Cells

A FlamingoPV project

D. Rajagopal
Photovoltaic Materials & Devices
July 2020

TU Delft

Modulated Surface Texturing on Temporary Aluminium Substrate for Flexible Thin-Film Solar Cells

A FlamingoPV project

by

D. Rajagopal

In partial fulfilment of the requirements for the degree of

Master of Science
in Electrical Power Engineering

at the Delft University of Technology,
to be defended publicly on Thursday July 23rd, 2020 at 13:30

Student number: 4894960

Thesis committee:	Prof. dr. A. H. M. Smets,	TU Delft, ESE- PVMD, Supervisor
	Dr. ir. R. Santbergen	TU Delft, ESE- PVMD, Assistant Professor
	Dr. ir B. Gholizad	TU Delft, ESE- DCES, Assistant Professor
	Dr. G Limodio	TU Delft, ESE-PVMD, Daily Supervisor
	Dr. D. Bartesaghi	HyET Solar, Daily Supervisor

TU Delft PVMD Delft University of Technology HyET Solar Flexible light weight solar modules EKL Else Kooi Laboratory

Contents

List of Figures

List of Tables

Acknowledgements

When I started writing my thesis, people told me that writing the literature review would be the hardest part. However, as I look back at these two wonderful years in the university, I am in loss of words to express my heartfelt gratitude to everyone who helped me reach this point.

Dr. Gianluca Limodio, for being the best daily supervisor one can wish for. You have gone above and beyond to guide, support and encourage me throughout my thesis. I will be forever grateful for your calmness, without which this would not have been achievable. You are the boss.

Prof. Dr. Arno Smets, thank you for being a great teacher. You have inspired me to specialise in PV even before joining Delft. I thank you for giving me the opportunity to work with you on this exciting project and for your timely assurances. As Mark Twain once said: “I can live for two months on a good compliment”. It has been an honour working with you and I hope we get an opportunity to work together in the future.

My sincerest gratitude to Dr. Davide Bartesaghi, who not only gave me an opportunity to work at HyET Solar but has been guiding me and giving me the freedom to experiment. I am extremely thankful for your critical examination of my work and for providing new perspectives. I would also like to thank Dr. Edward Hamers for letting me be part of the HyET group.

I would like to thank Thierry de Vrijer for his valuable suggestions and support throughout the project, Dr. Rudi Santbergen for all his help with the optical measurements and GenPro simulations, Nasim Rezaei and Ana Rita for helping me improve my presentation. I would also like to thank the EKL and Kavli Nano lab team, especially Lodi Schriek and Martijn Tijssen for taking the time to help me with the measurements and equipment.

Three of us started this journey together. To Eric and Sajith, my fellow FlamingoPV members, I am thankful for your support and for being part of this journey.

None of this would have been possible without a support system in place. I want to thank my fellow office-mates- Annanta, Harsh, Georgia, Linton, Kyriakos, Nithin for all those crazy conversations, Nitish, Omkar and Ajay for helping me out with the subjects. I thank Bibin, Saran, Thamban, Adeep, Alekhya and my beloved KSA team for making Delft my second home.

It is you who have dealt with the rockiness at close quarters - Anand, Ginu, Soorya, Madhu, Revathi and Mahroof. You have been exceptional. Thank you for cheering me on from miles away and for being the best people on this planet.

None of this would have been possible without my parents. I can never thank you enough for the unparalleled love, and for giving me the strength to pursue my dreams. These two years were highly challenging, and I am extremely grateful for your endless patience and your unwavering confidence in me. I dedicate this work to both of you.

Devika Rajagopal
Delft, July 2020

Abstract

Thin-film photovoltaic technologies are gaining momentum over the currently dominated crystalline silicon technologies. In addition to the competitive prices, flexible thin-film technology especially has the added advantage such as in building integrated photovoltaics (BIPV) due to its flexibility and light weight. HyET Solar B.V. is a company based in the Netherlands which state-of-the-art Roll to Roll (R2R) technology to produce such flexible solar cells. A temporary aluminum foil is used as substrate on to which FTO/p-i-n solar cell stack is deposited. The temporary foil is etched away, and the layers are encapsulated in low cost polymer foils. This thesis is part of the on-going FlamingoPV (Flexible Lightweight Advanced Materials In Next Generation of PV) project in collaboration between HyET Solar and TU Delft, to develop single, tandem and triple junction cells with 12, 13 and 14% efficiencies and a lifetime longer than 35 years. This thesis is inspired by the work of Tan *et. al* [8] where record efficiency cells were achieved on solar cells deposited on 'Modulated Surface Textured' (MST) glass substrates. In MST, increased light scattering is obtained by superposition of various scattering mechanisms which is achieved by introducing different textures at different interfaces and stacking them together. The requirements of the MST are two-fold: to provide efficient light trapping and to aid in the growth of high-quality layers.

The aim is to introduce MST in the R2R process by developing micro sized crater-shaped features on the temporary Al foil on to which naturally nano sized V-shaped textures of FTO is deposited. The crater-shaped features are developed on the Al foil (~110 μm) using wet chemical etching techniques. Various acid and alkaline based etchants are experimented. The etching parameters- concentration and temperature of the etchant and the etching time are varied to achieve the optimum recipe. These parameters should be varied such that the features have a correlation length (an estimate of how wide the feature is) 3-4 μm and an aspect ratio (ratio of RMS roughness to correlation length) of 12-14%. These features are characterized using SEM and AFM to measure the aforesaid parameters and reflectance and angular intensity distribution measurements to measure its effectiveness of scattering.

Alkaline based etchants (KOH and NaOH) resulted in crater-shaped features unlike acid etchants which resulted in pyramidal features. It was observed that there is an initial 'induction period' before which the etching started. For lower temperature, time and concentration, the induction period is longer. To ensure mechanical stability during deposition stages, the foil needs to be thicker than 70 μm on lab-scale. The above-mentioned etching parameters were varied, and the best recipe was found to be 1.78M KOH at 70°C for an etching time of 2 minutes, 1.78M KOH at 60°C for 3 minutes and 1.42M NaOH at 70°C for 2.5 minutes. These samples displayed a correlation length 4-4.6 μm and aspect ratios from 12-14% which is close to the targeted values and are higher than the existing texturing at HyET ('factory baseline') which had correlation length and aspect ratios of 500 nm and 5.7% respectively. These samples also showed higher scattering compared to the factory baseline. The nc-Si:H and a-Si:H/nc-Si:H layers deposited on to these samples resulted in dense high-quality layers. The TCO/p-i-n layers deposited also adapted the texturing pattern of the Al foil, unlike the factory baseline where the Al surface morphology was not adapted by the other layers as the features were significantly smaller. Further, to enhance the uniformity of texturing, various 'chelating agents' and 'surfactants' such as gluconic acids and glycols as well as varying the speed of etching to ensure homogenous

contact of etchant with the foil was carried out. Both these techniques resulted in in an increased etch rate as well as an increase in the density of the craters on the foil.

Considering the limitations of the R2R process, the best lab recipes were adapted (50°C, 1.42M NaOH, 1.8 minutes) to implement on the R2R etching machine. The resulting Al foil had higher surface morphology parameters and scattering compared to the factory baseline. The cells deposited on this texturing adapted the morphology of the Al foil. Optical simulations were done using GenPro4 where the AFM data of the textures were given as the input. The best lab samples as well as the R2R testing recipe showed larger absorption in the higher wavelengths in both nc-Si:H single junction and a-Si:H/nc-Si:H tandem cells, compared to the standard factory baseline texturing.

1 Introduction

1.1 Solar Energy

Solar energy is the most abundant source of energy on Earth. However, the current power grid runs on conventional energy sources such as fossil fuels, nuclear etc. According to the Renewables 2019 Global Status Report by the Center for Climate and Energy Solutions (C2ES), the percentage of renewable energy was estimated to be at 18.1 % of the global total energy consumption as on 2017, of which solar photovoltaics accounted for only 2%. 2018 witnessed the highest rise (~2.3%) of global energy demand in a decade due to which, the carbon dioxide emissions grew by approximately 1.7% [1]. This results in global warming where the years between 2009-2018 has seen a rise of 0.93 ± 0.07 °C with respect to the years between 1850 and 1900 [2]. With the current trend of rapidly increasing population, which is estimated to be 9 billion by 2040, the humankind faces energy shortage, in other words, a problem of supply and demand [3]. Thus, due to the increasing energy demand for industrial and residential applications, these conventional sources are depleting fast and due to its detrimental effects on the environment, the focus needs to be shifted to a cleaner generation of power. The distribution of energy consumption is shown in Figure 1.

There are numeral sources of renewable energy-wind, solar, biomass etc. The current capacity of renewable energy is 2350GW of which 485GW is accounted by solar energy. This can be converted to electricity by semiconductor based devices called solar cells (480GW solar photovoltaics) or to heat (5.45GW concentrated solar power (CSP)) [4]. Solar energy can also be converted to chemical energy referred to as solar fuels. Solar energy that falls on the Earth's surface in an hour is said to be sufficient to cater to one's energy requirements for a whole year [5].

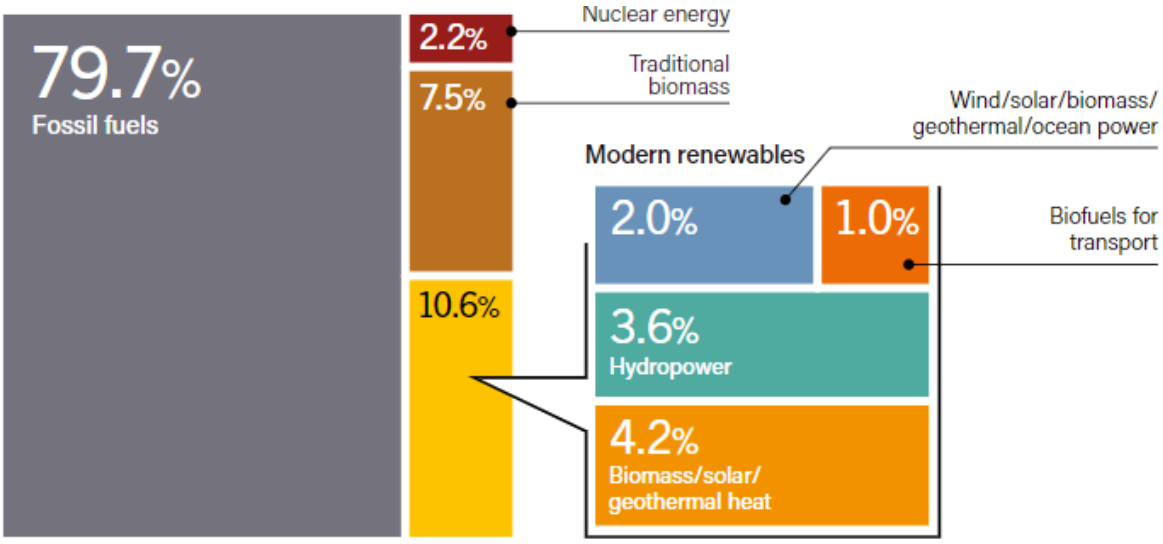

Figure 1: Energy consumption 2017 [1]

1.2 FlamingoPV

FlamingoPV stands for Flexible Lightweight Advanced Materials In Next Generation of PV which is an on-going project in collaboration between TUDelft and HyET Solar. The highlight of this project is flexible and light weight PV modules. The project aims to develop PV modules with stabilized efficiencies higher than 12% and a lifetime longer than 35 years. The objective of this project is the development of a tandem solar module with an efficiency higher than 13% and a triple junction module with conversion efficiencies higher than 14%. These flexible PV modules have advantages over the crystalline modules in areas of Building Integrated PV (BIPV) such as facades, roofing membranes etc. and in large scale floating applications. Also, HyET solar uses fluorine doped tin oxide which is moisture resistant which in turn results in reduced cost as it doesn't need additional moisture resistant encapsulants [6].

The single junction modules developed consists of hydrogenated amorphous Silicon (a-Si:H) as the absorber layer made on 1.67m^2 module area currently has a stabilized of 7%. A 10% efficiency was recorded in the best tandem made of amorphous and nanocrystalline silicon (a-Si:H/nc-Si:H) as absorber layers. The structure of this tandem is depicted in Figure 2 [6].

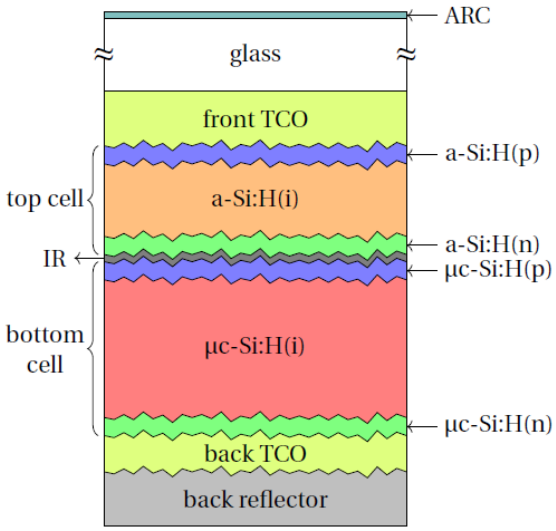

Figure 2: Structure of tandem solar cell developed at HyET [7]

HyET Solar has state-of-the-art Roll to Roll (R2R) technology for developing these modules (explained in section 2.5.1). The technology is suited for single junction and double junction devices. The technology currently operates on 35 cm wide foils. The technology also has been realized for 130cm wide foils as well. A temporary aluminium foil (~110 µm thick) used as a temporary substrate. This will be textured to induce micro sized craters. Subsequent TCO layer will be deposited on top these textures to achieve modulated surface texturing (MST) (explained in section 1.3). This is a similar approach used in record efficiency of micromorph modules on glass substrates developed at TU Delft [8]. The TCO (SnO_2:F) will be further studied and optimized to fully achieve MST which will contribute to an increase in efficiency. As stated, a triple junction with a-Si:H/nc-Si:/H/nc-Si:H will be developed and tested for the purpose of better spectral utilization and improved stability (as a-Si is prone to Staebler Wronski Effect where the efficiency drops to 85-90% of its initial value after 1000 hours of illumination) [3] [6].

The FlamingoPV project aims to develop a flexible lab scale 5 cm^2 tandem cell (a-Si:H/nc-Si:H) with a stabilized efficiency of 13% and a-Si:H/nc-Si:H/nc-Si:H cell with 14% efficiency. The project aims to upscale it to implement it in the roll to roll production and achieve 30 x 30 cm^2 modules with 12% aperture area stabilized efficiency.

1.3 Modulated Surface Texturing

As stated in section 1.2, this project is inspired by record efficiency cells developed on textured glass substrates as shown by [8]. To achieve high efficiencies, light trapping becomes important in thin film solar cells. For this, textures are introduced on surfaces which aids in scattering of light (given in detail in section 2.5.2). This increases the optical path length of the light by multiple reflections at rough interfaces and thus improves the absorption of light. Efficient light trapping becomes important in multijunction approaches in thin film solar cells especially at higher wavelengths (red and infra-red) for better spectral utilization [9]. The developed textures have two functions: it should aid in effective light trapping and it should have an appropriate morphology which helps in growing high quality nc-Si layers on it. For example, in a tandem of a-Si:H/nc-Si:H, sharp nano textures will aid in effective light trapping for the a-Si:H layer which will result in a thinner layer. However, micro-textures with smooth U shape aids in dense defect free growth of the nanocrystalline silicon layer which results in better electrical performance [10] [11]. The micro U-shaped textures becomes important in cells with nanocrystalline silicon at high deposition rate, as its performance is more prone to the morphology of the substrate [12] [13]. In the HyET tandem cells, it was also found that proper texturing is needed for stress management as device grade nanocrystalline silicon shows significant internal stress [6]. Thus, U shaped smooth micro-textures are needed for efficient light trapping especially in the red and Infra-red range without compromising the electrical performance of the nanocrystalline solar cells leading to higher short circuit current densities without reduction in the fill factor and open circuit voltage.

In a-Si:H/nc-Si:H tandem cell, the top amorphous crystalline layer contributes to two-third of the total output power [3]. As mentioned in section 1.2, a-Si:H layer suffers from light induced degradation (SWE) due to the formation of metastable defects as a result of recombination of light induced charge carriers. Hence it is not possible to have a thicker a-Si:H layer as it can result in a higher light induced degradation [3]. Thus, sharp nanotextured structures/ textured TCOs are used which will aid in multiple scattering and thus increasing the optical path length, which can result in lower absorber layer thicknesses. In this case reduced thickness of the a-Si:H layer implies it is less susceptible to SWE which improves the stability. However, these sharp nanofeatures are not suitable for the bottom nc-Si:H cells as explained in the previous paragraph.

Therefore, the concept of Modulated Surface Texturing (MST) was introduced where *"enhanced scattering is achieved by superposition of different scattering mechanisms caused by the different geometrical features integrated in a modulated surface texture"* [9]. This is achieved by introducing different textures at different interfaces and stacking them together. To ensure that the morphology of one layer is transferred to the subsequent layer, the layers should be thin enough. Thus, one obtains as result, a surface which has the superposition of all the morphological features of the individual layers. "By combining appropriate geometrical features introduced at the individual interfaces one can take advantage of superimposing the scattering mechanisms caused by these different geometrical features and achieving higher scattering levels in a broad wavelength range in comparison

to the scattering contributions from individual morphologies" [9]. A pictorial example of the concept of MST is shown in Figure 3.

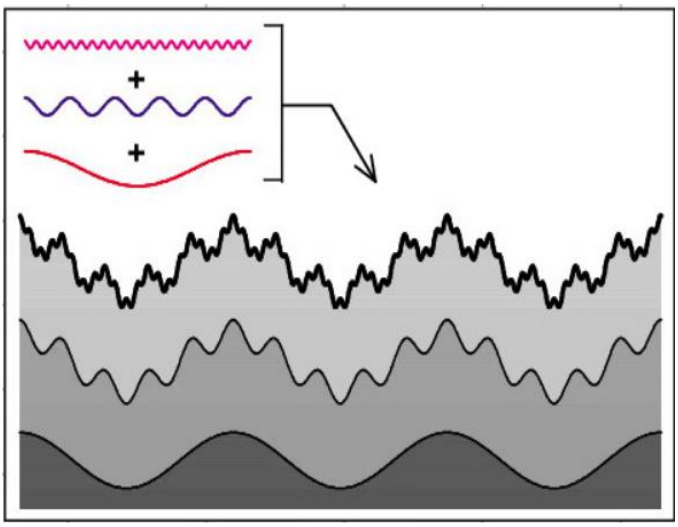

Figure 3: Example of superposition of textures resulting in MST [9]

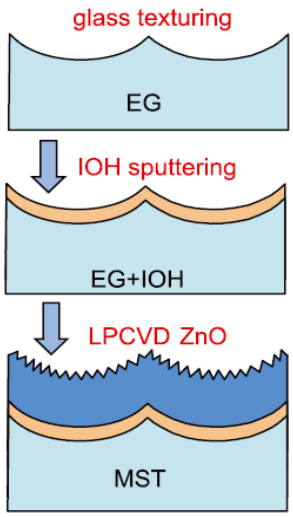

Figure 4: Fabrication of highly transparent MST electrode [8]

World record initial efficiency of 14.8% has been achieved by Tan et al. [11] in a-Si:H/nc-Si:H tandem solar cells and a stabilized efficiency of 12.5% which is close to the world record efficiency of 12.69% as demonstrated by [14]. In [8] micro textures were developed on Corning glass (Eagle XG) using a process called wet chemical etching (explained in section 3.1). The glass was first sputtered with a thin layer of ITO which acts as a catalyst for the glass etching (sacrificial layer). The glass was etched with a mix of 49% aqueous solution of hydrogen fluoride and 31% of peroxide (volume ratio of H_2O: HF: H_2O_2 = 10:1:2). After the ITO was fully removed from the from the glass, a highly transparent and conductive IOH (hydrogenated indium oxide) was sputtered onto it. A layer of zinc oxide (ZnO) was further deposited on to this layer which is naturally nano textured. This bilayer of IOH and ZnO (nano textured) acts as a TCO providing which effectively traps light for the a-Si:H top cell while ensuring reduced parasitic absorption and concurrently, good conductivity for the front window layer. The suitable growth of nc-Si:H cell and sufficient light trapping in the red and IR range is ensured by the U-textured glass. The combination of nanotextured and microtextured layers forms a highly transparent MST front electrode for the tandem solar cell. This method has given a higher efficiency as stated above compared to single texturing. The texturing process is depicted in Figure 4.

The performance of the solar cell and its quality of the materials are influenced by the shape and size of the features. These can be characterized using the root mean square roughness, autocorrelation length, aspect ratio and slope of the features. It was found that varying the thickness of the sacrificial layer (ITO in this case) influences the crater size developed on the glass- higher the thickness, higher the crater size. Figure 5 shows different substrates: (A) low pressure chemical vapour deposition of zinc oxide, (B) wet etched sputtered aluminium doped zinc oxide (E-AZO) on a flat glass, (C)(D), wet etched glass substrates having increasing micro features which is further coated with an AZO layer as the front electrode. Further details of the experiment are available in [8].

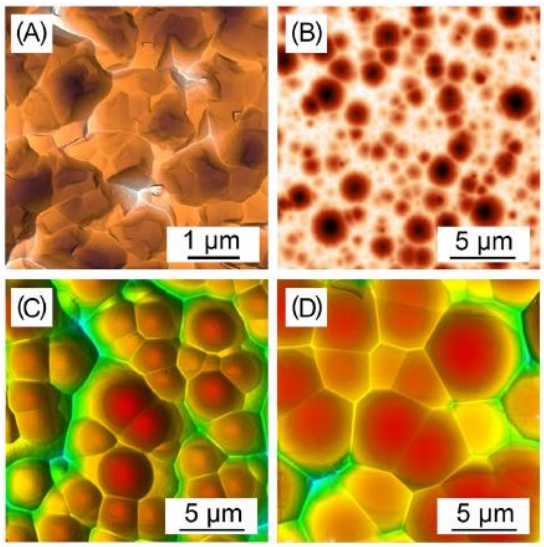

Figure 5: AFM image (A) LPCVD ZnO (B) E-AZO on flat glass (C-D) microtextured glass [8]

These samples were used as substrates for deposition of nc-Si:H solar cells with an i layer thickness of 3µm. From Table 1 it can be observed that the substrate with the highest aspect ratio (ratio of RMS roughness to correlation length) has the highest short circuit current density J_{SC}, however, the lowest open circuit voltage V_{OC} and fill factor FF (due to the formation of defects resulting in recombination and can act as shunts [15]), resulting in the lowest efficiency [8]. The aspect ratio can be a direct indication of the sharpness of features, higher the aspect ratio, sharper the feature. As aspect ratio decreases, the feature becomes smoother. From sample A it can be stated that the sharp features proved as an excellent light trapping source, however it is not suitable for the quality growth of nc-Si:H which resulted in the lowest V_{OC}. Sample C has the best V_{OC} and FF from the data set and the lowest aspect ratio. However, it cannot be concluded that the lowest aspect ratio gives the highest efficiency since a lower aspect ratio implies a very smooth surface which will not aid in light trapping. But it can be noted that the best values (V_{OC}, FF and efficiency) resulted when the substrates correlation length was comparable to that of the absorber layer thickness [8]. For the cells developed on C and D due to the micro sized U-shaped craters, the absorber layers are grown uniformly without any defects [11]. Therefore, to achieve the best results for a given cell thickness, a combination of optimum aspect ratio and correlation length is essential.

	R_{rms} (nm)	L_c (µm)	R_{rms}/L_c	V_{oc} (V)	J_{sc} (mA/cm^2)	FF (%)	Eff (%)
A	126	0.45	0.28	0.526	27.7	51.1	7.4
B	178	1.09	0.16	0.538	25.8	68.2	9.5
C	370	2.72	0.14	0.552	25.6	72.6	10.2
D	546	3.59	0.15	0.545	24.4	70.7	9.4

Table 1: Performance of the nc-Si:H solar cells deposited on substrates A-D along with RMS roughness, correlation length, and aspect ratio [8]

Similarly, a-Si:H layer has been optimized for MST substrates. In addition to depositing on MST substrates with different thickness of front electrode (AZO in this case), it is also subjected to plasma treatments. It is shown is studies that the deposition of a-Si:H on naturally textured TCOs (ZnO:B) results in poor V_{OC} and FF values because of the defective formation of a-Si:H layer due to the sharp texturing [16] [17]. As shown in Figure 6, the inclination angle of the texture facet θ increases when

it is deposited on microtextured glass. As θ increases, the deposited layers become highly non-uniform, voids are formed in the valleys which will result in recombination centers [8]. Plasma treatments are done to smoothen out the sharp peaks with a reduction in the roughness. This influences the scattering property as well. But subjecting the TCO to long exposure to plasma can result in a very high reduction in roughness which will lead to reduced light trapping and thus a very low J_{SC}. An optimized plasma exposure is chosen which will enable optimized roughness with sufficient scattering resulting in better cell performance [16]. The thickness of the TCO needs to be optimized as well. Table 2 shows that the best performance values are for layers deposited on MST substrate exposed to 4 minutes of argon plasma treatment.

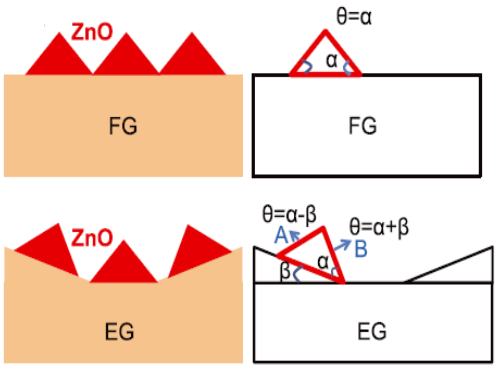

Figure 6: Inclination angle of AZO on flat glass and etched glass [8]

Substrate	ZnO layer	Treatment time (min)	V_{oc} (V)	J_{sc} (mA/cm^2)	*FF* (%)	*Eff* (%)
FG	iZ1	0	0.936	12.9	73.6	8.9
EG		0	0.946	11.6	70.1*	7.7
MST	iZ0.5	0	0.937	13.0	71.3	8.7
MST	iZ1	0	0.892	12.5	60.4	6.7
MST	iZ1	4	0.943	13.0	74.0	9.1
MST	iZ2.3	0	0.655	7.7	38.5	1.9
MST	iZ2.3	4	0.825	10.8	50.9	4.5
MST	iZ2.3	15	0.938	12.6	68.6	8.1

Table 2: Performance of the a-Si:H solar cells deposited on flat glass, etched glass and MST substrates subjected to different argon plasma treatment times [8]

a-Si:H/nc-Si:H tandem cell is deposited on the optimized MST substrate. Figure 7 shows the cells deposited on a single textured (nano-texturing by TCO) and on MST substrates. Cracks are visible in (A) which causes a decrease in the solar cell performance. Table 3 summarized the performance of these cells deposited on A and B. The design is further improved and optimized to achieve initial efficiency of 14.8% and 12.5% of stabilized efficiency [8].

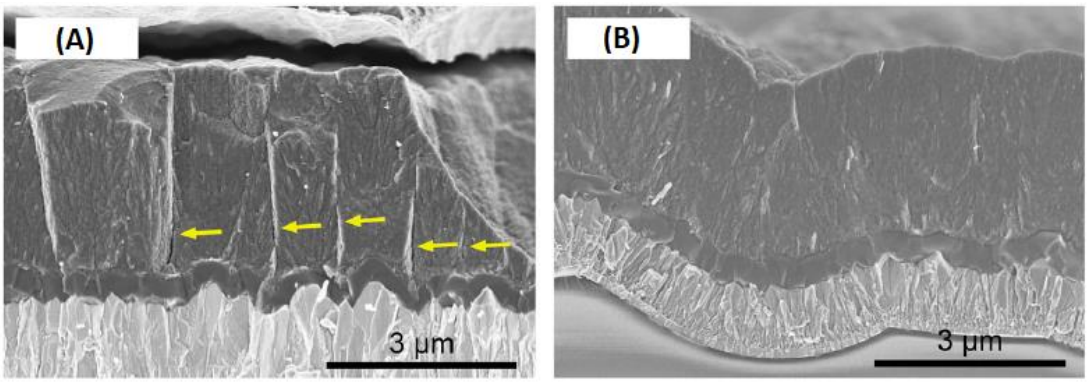

Figure 7: Cross section of tandem cells deposited on (A) single texturing by TCO (B) MST [8]

Substrate		V_{oc} (V)	J_{sc} (mA/cm^2)	J_{sc} top/bottom	*FF* (%)	*Eff (%)*	Degradation ratio (%)	R_{oc} (Ωcm^2)
B	Initial	1.401	12.9	13.7/12.9	74.4	13.4		7.2
	Stabilized	1.373	12.5	13.0/12.5	67.0	11.5	14.2	10.5
A	Initial	1.371	11.5	14.1/11.5	72.1	11.4		8.5
	Stabilized	1.314	11.8	13.1/11.8	49.3	7.6	33.3	26.9

Table 3: Performance of the tandem solar cell deposited on single textured substrate A and MST substrate B [8]

Similar work has been done in [18] where MST is achieved through ITO induced texturing (IIT) for craters/ U shaped features greater than 10 μm and aluminium induced texturing (AIT), wet etching of sputtered AZO (E-AZO), ZnO:Al induced texturing (ZIT) for nano / V-shaped textures. The performance of the solar cells deposited on single texturing (IIT) and MST substrates (MST-x) are shown in Table 4. The cells deposited on MST substrates has a superior performance compared to the ones deposited on single texturing.

Substrate	Thickness (μm)	V_{oc}(V)	*FF*(-)	J_{sc}(mA/cm^2)	Eff. (%)	$V_{oc} \times FF$(V)
IIT	2.0	0.525	0.740	23.5	9.14	0.389
MST-AIT	2.0	0.530	0.723	25.9 ↑*+10.1%**	9.92 ↑*+8.5%*†	0.383
MST-EAZO	2.0	0.517	0.732	25.7 ↑*+9.1%**	9.71 ↑*+6.2%*†	0.378
MST-ZIT	2.0	0.546	0.745	25.6 ↑*+8.9%**	10.4 ↑*+13.9%*†	0.407
IIT	3.0	0.529	0.724	25.4	9.73	0.383 ↓*–1.5%*‡
MST-AIT	3.0	0.532	0.726	26.3 ↑*+3.4%**	10.2 ↑ *+4.5%*†	0.386 ↑*+0.7%*‡
MST-EAZO	3.0	0.496	0.691	27.4 ↑ *+7.8%**	9.40 ↓ *–3.4%*†	0.343 ↓*–9.3%*‡
MST-ZIT	3.0	0.532	0.748	26.4 ↑ *+3.7%**	10.5 ↑ *+7.8%*†	0.398 ↓*–2.2%*‡

Table 4: Performance of solar cells deposited on single textured and MST substrates [18]

1.4 Aim and outline of this thesis

The thesis forms part of the FlamingoPV project between HyET Solar and TU Delft. Inspired by the work of Tan *et al*. [8], the project aims to adapt the micro texturing on glass substrates on to a temporary aluminium foil. This aluminium foil acts as a temporary substrate on to which the solar cell layers are deposited.

The first part of the thesis aims at improving the current texturing at HyET Solar. The method used here for texturing is wet chemical etching using acids and bases. The textured foil addressed as 'factory baseline' will be studied for its reflectance and scattering properties. Further, the factory baseline will be analysed for studying its surface morphology (root mean square (RMS) roughness, correlation length (Lc), aspect ratio (AR) and mean slope (θ_M). After the baseline has been studied and established, experiments for targeted development of the above-mentioned parameters will be designed. The aim is to develop features with an aspect ratio of 12-14 % and a correlation length of 3-4 μm for tandem and triple junction cells.

The thesis can be thus sub divided as:

i. Development of different solutions for aluminium texturing: This involves wet etching of aluminium foil with various acids and bases. Parameters of the etching solution-temperature, etching time, concentration, speed of rotation of etchant will be varied and tested
ii. Characterization and evaluation of these different solutions: The aluminium foils subjected to various solutions as stated in (i) will be analysed using ARTA setup, IS setup, SEM and AFM analysis
iii. Application of the obtained morphologies in an optical simulator to understand the performance of a device: The obtained morphology (AFM height data) will be used as the input for optical simulation to understand the effectiveness of texturing
iv. Implementation of optimized micro texturing recipe in the lab to the roll-to-roll production line at HyET: By taking the machine and other limitations into account, the optimized lab recipe should be adapted for testing in the R2R production.
v. Characterization and evaluation of the R2R tested aluminium foil: The processed foil will be subjected to tests as stated in (ii) and will be compared with the baseline and other lab results
vi. Verification of MST: Samples with TCO/other layers deposited on the Al foil is subjected to measurements as stated in (ii) and the cross sections will be analysed to check if the texture of the foil is adapted by the subsequent deposited layers
vii. Understanding the etching kinetics to understand how the texturing can be controlled so that it can be adapted as requirements are changed

2 Fundamentals

2.1 Working principle

The working principle of solar cell can be explained by the 'Photovoltaic effect' in which the incident light energy from the sun is converted to electrical energy. For this purpose, solar cells which are made up of semiconductor materials are used. In response to an electromagnetic radiation, a potential difference is created at the junction of two different semiconductor materials [3]. This is used to perform useful work when connected in an external circuit.

The solar energy which reaches the Earth's atmosphere is a form of electromagnetic (EM) radiation which is distributed from 300 to 4000nm [19]. The radiation outside the earth's atmosphere is similar to that of the radiation emitted by a 'blackbody' in thermal equilibrium for a particular surface temperature T, as described by Planck's law. Since the radiation does not traverse through the earth's atmosphere, it is called the AM0 spectrum. The radiation gets attenuated due to scattering and absorption caused by dust particles, air molecules esp. H_2O, O_2 and CO_2. This absorption is wavelength selective and causes gaps in the spectral distribution. To use as a reference for comparison, standard test conditions (STC) are defined: 1000W/m^2 Irradiance, AM1.5 spectrum, 25°C cell temperature. The irradiance incident on a sun-facing plane tilted 37° w.r.t. to the ground is defined by the AM1.5 spectrum [3]. Comparison of spectral radiance of a blackbody at 6000K, AM0 and AM1.5 is given in Figure 8.

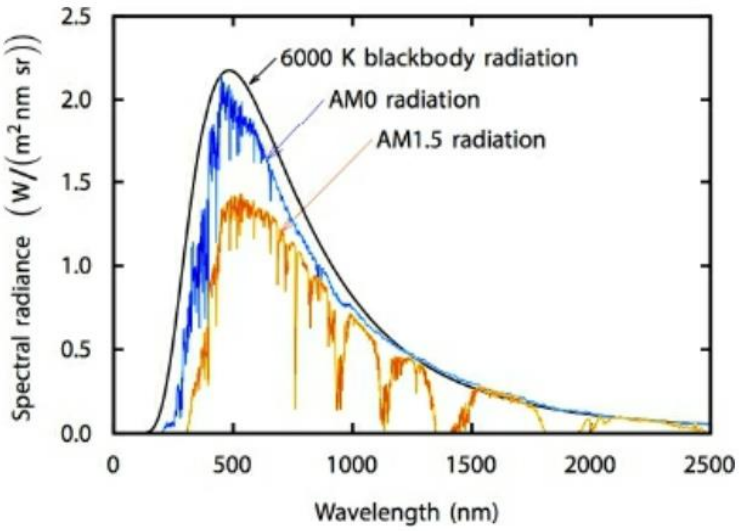

Figure 8: Blackbody spectrum at 6000K, AM0 and AM1.5 spectrum

The light consists of quanta of energy called as photons which can be defined as:

$$E_{ph} = h\upsilon \tag{2.1}$$

Where E_{ph} is the energy of photon, h is the Planck's constant and υ is the EM frequency. The equation for wavelength of light can be written as:

$$\lambda = \frac{c}{\upsilon} \tag{2.2}$$

Where λ is the wavelength and c is the speed of light. Combining equations (2.1) and (2.2), the energy of photon can be written as [3]:

$$E_{ph} = \frac{hc}{\lambda} \tag{2.3}$$

With the help of these, the photovoltaic effect can be divided into 3 processes: Generation, Separation and Collection of charge carriers.

(i) *Photogeneration of charge carriers*: The absorbed energy is used to excite an electron from its initial to final stage (E_i to E_f). In a semiconductor material, electrons are present in the valence band and conduction band. E_V and E_C denotes the edges of valence band and conduction band. The energy band gap E_G is defined as the energy difference between E_C and E_V and is called the forbidden bandgap since no energy states are allowed. A photon only gets absorbed if it has energy equal to or higher than the bandgap energy ($E_{ph} > E_G$). An electron is thus excited from the initial energy level E_i to the final energy level E_f. A void is created at E_i which behaves like positive charged called hole. Thus electron-hole pairs are created. This is illustrated in Figure 9. [3].

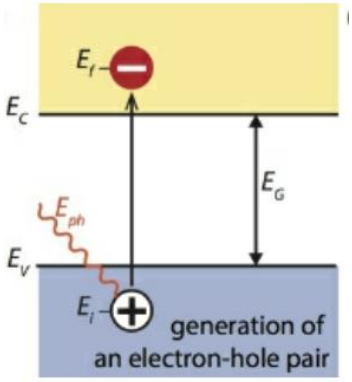

Figure 9: Generation of electron hole pair when $E_{ph} = E_G$ [3]

(ii) *Separation of photogenerated charge carriers*: These generated electron hole pairs must be collected before they recombine. Therefore, semipermeable membranes are present on both sides of the absorber material to collect these charge carriers. These are selective membranes (p and n type semiconductor materials explained in section 2.2.1) such that it only allows only electrons or holes to pass through each membrane [3].

(iii) *Collection of photogenerated charge carriers*: These separated charge carriers are collection using metal contacts. The electrons pass through the external electrical circuit, thus converting chemical energy of electron hole pairs into electrical energy, after which it recombines with the holes at the metal semiconductor junction [3]. The concept of separation and collection is shown in Figure 10.

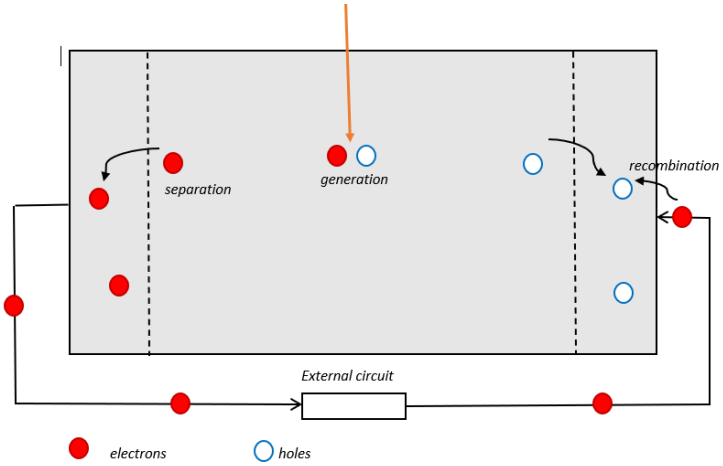

Figure 10: Pictorial representation of working principle of a solar cell. Inspired by [3]

2.2 Semiconductor physics

Semiconductors can be defined as materials that has conductivity between those of insulators and conductors (10^5 to 10^{-6} Sm^{-1}) [20]. The semiconductor materials can be classified in two groups. First, the elements found in the group IV of the periodic table (e.g. Silicon) called the elemental semiconductors. Second, semiconductors formed by the combination of elements in group III and V (e.g. GaAs,) or that of group II and VI. These are called the binary or compound semiconductor materials [21]. Silicon is the most used semiconductor material in integrated circuits as well as in photovoltaic materials [3] [21].

2.2.1 Properties of semiconductor

Doping: The crystal material without any impurity present is called an intrinsic material. The semiconductor properties can be varied by changed by changing the number of electrons or holes present in it by adding controlled amount of impurity atoms called as dopants (these atoms will replace the silicon atoms). These materials are called extrinsic semiconductors. Group III and V elements (namely boron and phosphorus) are usually used. When a group V element is added, four out of the five valence electrons will form bonds with silicon whereas the fifth electron is loosely bound which can absorb thermal energy and moves freely through the lattice. Thus, there is a free mobile electron which increases the electron concentration and these impurity atoms are called *donors.* Similarly, when a group III atom is introduced, the three valence electrons cannot readily form bonds will all the four silicon atoms. Hence at room temperature, electron from nearby Si-Si bond moves and attaches to the impurity atom. This way a hole is created (absence of electron) which moves freely within the lattice. These impurity atoms are called *acceptors.* The electrical conductivity of the semiconductor can be modified this way by doping. When the electrical conductivity is dominated by holes, it is a *p-type* semiconductor and when it is dominated by electrons, it is an *n-type* semiconductor. The fermi level is also influenced by doping. By increasing the donor concentration, the fermi energy increases and moves closer to the conduction band. Whereas increasing the acceptor concentration moves the fermi level closer to the valence band [3]. This is shown in Figure 11. The electrons in the n-type semiconductor are called *majority charge* carriers and the holes are called the

minority charge carriers. Whereas, in p-type, the holes are the *majority charge* carriers and electrons are the *minority charge carriers* [21].

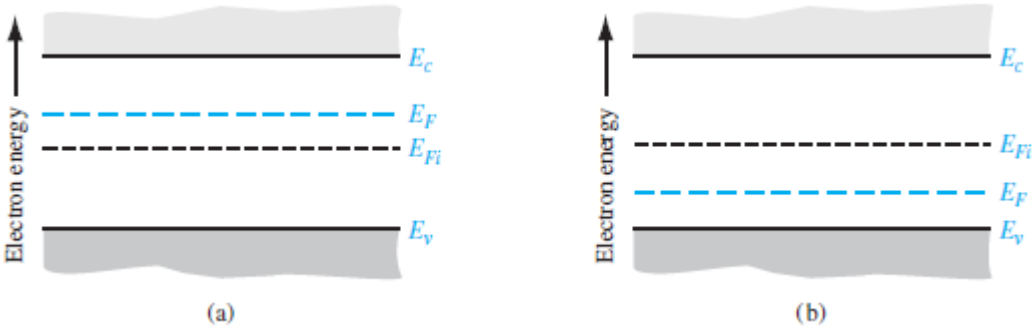

Figure 11: Fermi levels for (a) n-type and (b) p-type semiconductor [21]

Carrier Transport: The process by which the electrons and holes move in a semiconductor is called *transport.* The movement of the charge carriers in response to an electric field is called *drift* which gives rise to a *drift current.* The total drift current density can be given as:

$$J_{drift} = e(\mu_p p + \mu_n n)E \tag{2.4}$$

Where $\mu_{n,p}$ are electron and hole mobilities, which is dependent on temperature and doping concentrations and is a measure of how easily the particle moves within the semiconductor in response to the electric field.

Diffusion currents are created due to the movement of charge carriers from a region of high concentration to that of a low concentration due to random thermal motion. This current is proportional to the *gradient of particle concentration.* The total diffusion current can be given by:

$$J_{diffusion} = e(D_n \frac{dn}{dx} - D_p \frac{dp}{dx})$$

Where $D_{n,p}$ are electron and hole diffusion coefficients. The diffusion coefficients and mobilities can be linked by *Einstein relationship*:

$$\frac{D_n}{\mu_n} = \frac{D_p}{\mu_p} = \frac{k_b T}{e} \tag{2.5}$$

Direct and indirect bandgap semiconductors: The highest point of the valence band and the lowest point of the conduction band are vertically aligned in a direct bandgap semiconductor such that excitation of electrons require only the energy from the photon (*radiative generation for* $E_{ph} > E_G$). No additional momentum transfer is required. GaAs and a-Si are examples of direct bandgap semiconductors. Whereas, in an indirect bandgap semiconductor, both energy by the photon and momentum from lattice vibrations (called as *phonons*) are required to excite electrons from valence to conduction band. Hence, the absorption coefficient of indirect bandgap semiconductors is much lower than direct bandgap semiconductors. c-Si is an example of indirect bandgap semiconductors. The electronic dispersion diagrams of direct and indirect semiconductor are shown in Figure 12.

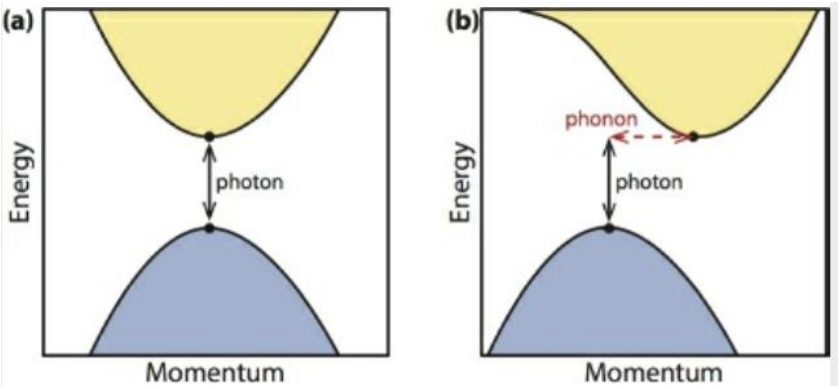

Figure 12: Electronic dispersion diagram of (a) direct and (b) indirect bandgap semiconductor [3]

Recombination in semiconductors: In thermal equilibrium the electron and hole concentration (n_0, p_0) is independent of time. Hence, the rate of generation (G) and recombination (R) are equal ($G_{n_0 p_0} = R_{n_0,p_0}$). In non-equilibrium, *excess carriers* (δn, δp) are generated. A lifetime τ is associated with the minority carriers, called the *minority carrier lifetime* (τ_{n0}, τ_{p0}) which describes the decay of excess minority carriers, i.e. it denotes the mean time before they recombine. The lifetime of a p-type material can be expressed as:

$$R_n{}' = R_p{}' = \frac{\delta n(t)}{\tau_{n0}} \tag{2.6}$$

where R_n' and R_p' are excess electron and hole recombination rates. When the generated excess carriers are not uniform throughout the semiconductor, there is a diffusion of these excess carriers before they recombine with the majority carriers. The distance over which they diffuse is called the *diffusion length* ($L_{n,p}$) given by:

$$L_{p,n} = \sqrt{D_{n,p}\tau_{n,p}} \tag{2.7}$$

where $D_{n,p}$ are the *diffusion coefficients.*

There are different recombination mechanisms in a semiconductor. In direct bandgap semiconductors, *direct/radiative recombination* is the major recombination mechanism. An excited electron falls back to the valence band, recombines with a hole, emitting a photon with energy equal to the bandgap. *Auger recombination* occurs in indirect bandgap semiconductors and is a three-particle process and is highly dependent on the charge carrier densities. The energy and momentum of the recombining electron-hole pair is transferred to another electron/hole which are further excited deeper into the conduction/valence band. When this electron/hole relaxes, the energy is transferred into the lattice as phonons. *Shockley-Read-Hall recombination (SRH)* occurs in indirect materials as well, which is facilitated by *lattice defects* which introduces *trap states* (E_T) within the forbidden bandgap. Electrons get trapped in these states attracts holes which then recombines emitting energy into the lattice as heat [3] [21].

p-n junctions: Solar cells are based on junctions between differently doped materials. The p and the n-type materials mentioned can be joined to create p-n junctions. When these two are brought together, the electrons from the n side diffuses to p-side and holes from the p side diffuses to n side. Due to this, the area near the *metallurgical junction* (interface between n and p type) becomes depleted of mobile charge carriers and a *depletion region* (also called as *space-charge region*) is

formed. This results in the formation of an internal electric field. This field causes the charge carriers to move opposite the concentration gradient. P-n junctions are the building blocks of solar cells. The charge carriers should be collected before they can recombine. Thin-film solar cells like a-Si:H are based on *p-i-n* configuration because of high defect densities. Due to this, the diffusion length can only be around 100-300nm and thus cannot rely on diffusion. The undoped *i-layer* can be hundreds on nm thick whereas the p and n layers are only a few nm thick. The electric field is thus stretched in the i-layer and the light excited carriers will move through the i-layer. Hence these are *drift devices* [3].

2.3 Optics

The field of optics deals with the properties and behaviour of light. The speed of light varies when the light travels in a medium other than vacuum. A medium can be characterized using *Refractive Index 'n'* which is the ratio of speed of light in vacuum to the speed of light in the medium. This is given by $n = c/v$, where c is the speed of light in vacuum, both of which are wavelength dependent. The value of *n* is usually higher than 1. The following sections deals with the interaction of light at flat and rough boundaries.

2.3.1 Optics of flat interfaces:

Two non-absorptive media are considered with real parts of refractive indices n_1 and n_2. When the light encounters a boundary, part of the light is reflected denoted by θ_r and the rest is refracted (or transmitted) denoted by θ_t. Based on laws of reflection the angle of incidence (denoted by θ_i) is equal to angle of reflection θ_r [22]. The relation between the refracted and incident part of the light can be described by *Snell's law* given as:

$$n_1 \sin \theta_i = n_2 \sin \theta_t \tag{2.8}$$

The incidence, reflection and transmittance of light at a flat boundary is shown in Figure 13.

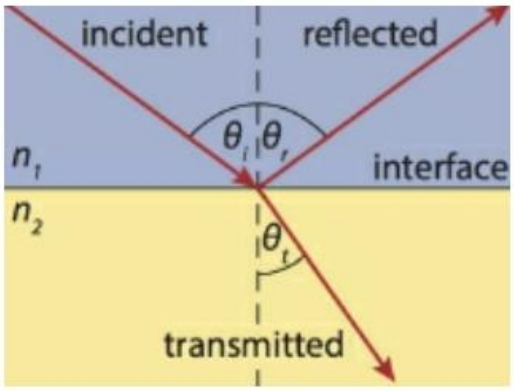

Figure 13: Incidence, reflection and transmittance at a flat interface [3]

The magnitudes of the incident, reflected, and refracted light are governed by Fresnel equations. The optical properties of the medium are governed by the polarization of light. The light can be distinguished as parallel and perpendicular polarized light. In parallel polarized light, denoted by 'P', the electric field is parallel to the incidence plane whereas in perpendicular polarized light, denoted by 'S', the electric field is perpendicular to the incidence plane. The Fresnel equations for parallel and perpendicular polarized light can be given as:

$$r_P = \frac{n_1 \cos\theta_t - n_2 \cos\theta_i}{n_1 \cos\theta_t + n_2 \cos\theta_i} \quad (2.9)$$

$$t_P = \frac{2n_1 \cos\theta_i}{n_1 \cos\theta_t + n_2 \cos\theta_i} \quad (2.10)$$

$$r_S = \frac{n_1 \cos\theta_i - n_2 \cos\theta_t}{n_1 \cos\theta_i + n_2 \cos\theta_t} \quad (2.11)$$

$$t_S = \frac{2n_1 \cos\theta_i}{n_1 \cos\theta_i + n_2 \cos\theta_t} \quad (2.12)$$

Where *r* and *t* denote reflected and transmitted light. However, sunlight is unpolarized [23]. The reflectivity *R* of the unpolarized light will be the mean values of parallel and perpendicular polarizations given by:

$$R = \frac{1}{2}\left({R_P}^2 + {R_S}^2\right) \quad (2.13)$$

For normal incidence equations can be obtained by substituting θ_i=0 in equations (2.9)-(2.11) [3].

'Total internal reflection' (complete reflection into the medium itself) occurs in the medium with higher refractive index than the surrounding medium when light is incident at an angle higher than the 'critical angle' [24]. From Figure 13, if $n_2 > n_1$, using eqn. (2.8), substituting $\theta_t = \theta_{critical}$ and θ_i=90°, the critical angle can be derived as:

$$\theta_{critical} = \sin^{-1}\left(\frac{n_1}{n_2}\right) \quad (2.14)$$

For angles, greater than the critical angle, TIR occurs into the medium. This is an Important design principle of solar cells to efficiently trap light using textured interfaces [3].

2.3.2 Optics of rough interfaces:

When a rough sample is irradiated with light under a given incident angle, it can get *transmitted (T), specularly reflected (R), diffusively scattered (S)* at the surface of the sample or in its volume or *absorbed,* shown in Figure 14.

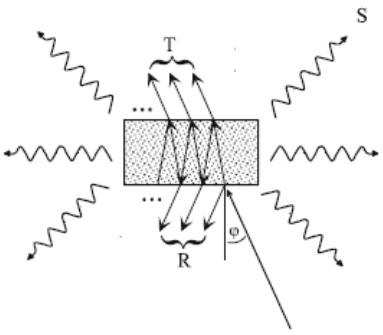

Figure 14: Light incident on a rough sample [25]

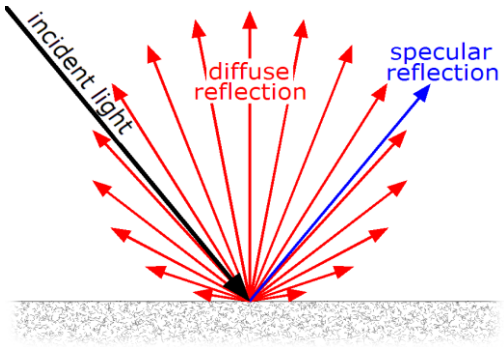

Figure 15: Specular and diffuse reflection [26]

As mentioned in section 2.3.1, reflection from a flat smooth surface obey the laws of reflection (θ_i=θ_r). This component of reflection is called *specular reflection*. In a rough surface, the incident ray gets reflected at different angles. Each ray obeys the law of reflection. The reflected angles are different because the surface met by each ray has a different orientation and hence a different surface normal. Thus, the surface scatters the light in different directions. This is depicted in Figure 15. In transparent

flat medium, the light passes through the material following the Snell's law, called *rectilinear transmission*. In rough transparent or translucent material, the light gets redirected to different directions, thus *diffusively transmitting*. The photons can get scattered or diffused internally in the sample as well as at the interfaces where there is a change in the refractive index [25] [27]. We consider the diffuse reflection and diffuse transmission as diffuse scattering along the surfaces and within the volume of the sample.

The specular transmittance of the sample can be defined as:

$$T_{Spec} \equiv \frac{I_{TSpec}}{I_I} \tag{2.15}$$

Where I_{TSpec} and I_I and the intensities of the transmitted and incident light. Similarly, we can write the specular reflectance R_{Spec}, scattering S and absorptance A as:

$$R_{Spec} \equiv \frac{I_{RSpec}}{I_I} \tag{2.16}$$

$$S \equiv \frac{I_S}{I_I} \tag{2.17}$$

$$I_S = I_{TDiff} + I_{RDiff} \tag{2.18}$$

$$A \equiv \frac{I_A}{I_I} \tag{2.19}$$

Where I_{RSpec} is the intensity of the specularly reflected light, I_S is the intensity of the scattered light (sum of diffusively transmitted and diffusively reflected) and I_A is the absorbed intensity. Based on the law of conservation of energy [25]:

$$T_{Spec} + R_{Spec} + S + A = 1 \tag{2.20}$$

The terms scattering and diffuse has been used interchangeably here. Diffuse reflection does not generally happen due to rough surfaces; it is contributed by the scattering centres that lie beneath the rough surface. In other words, scattering is the mechanism by which a rough surface gives diffuse reflection. Scattering is explained in detail in section 2.5.2.

2.4 Losses

A solar cell cannot convert all of the incident light to useful power, i.e. it is not 100% efficient. There are several factors that defines governs the efficiency of a solar cell. For a single junction solar cell, the theoretical efficiency limit is referred to as the *Schockley-Queisser Limit (SQL).* SQL limit considers the losses caused by *spectral mismatch* and the losses incurred due to the temperature of solar cell being higher than 0 K.

2.4.1 Spectral mismatch

A semiconductor material with a bandgap of E_G forms the absorber material in a solar cell. For successful absorption of a photon and generation of electron-hole pairs, the incident photon should

have an energy higher than E_G. Photons with energy lower than E_G *($E < E_G$)* are not involved in the energy conversion and are considered as below *bandgap losses (non-absorption).* Photons with energy higher than E_G *($E > E_G$)* will create electron-hole pairs. However, the extra energy received by the electron-hole pairs from the high energy photons will be release into the semiconductor lattice as thermal energy. This is called *losses due to thermalization.* Based on this, *ultimate efficiency* η_{ult} can be defined as:

$$\eta_{ult} = P_{abs} \times P_{use} \tag{2.21}$$

Where P_{abs} is the power absorbed by the solar cell to the incident power given by:

$$P_{abs} = \frac{\int_0^{\lambda_G} \frac{hc}{\lambda} \phi_{ph,\lambda} d\lambda}{\int_0^{\infty} \frac{hc}{\lambda} \phi_{ph,\lambda} d\lambda} \tag{2.22}$$

Where λ_G wavelength of photons corresponding to E_G. From the P_{abs}, a fraction of energy is lost due to thermalization. Therefore, the useful energy P_{use} can be given as:

$$P_{use} = \frac{E_G \int_0^{\lambda_G} \frac{hc}{\lambda} \phi_{ph,\lambda} d\lambda}{\int_0^{\lambda_G} \frac{hc}{\lambda} \phi_{ph,\lambda} d\lambda} \tag{2.23}$$

The losses due to spectral mismatch in a c-Si solar cells accounts to ~50%.

The ultimate efficiency is appliable for solar cells at 0K. For higher temperatures, the cell will absorb radiation and will also *emit* the same quantity of radiation causing recombination of electron-hole pairs leading to a non-zero recombination current density, open-circuit voltage loss and a reduction in fill factor. This can be categorized as *other losses.* Figure 16 depicts the loss mechanisms in SQL. The SQ limit is 33.1% at 1.34 eV for the AM1.5 spectrum [3].

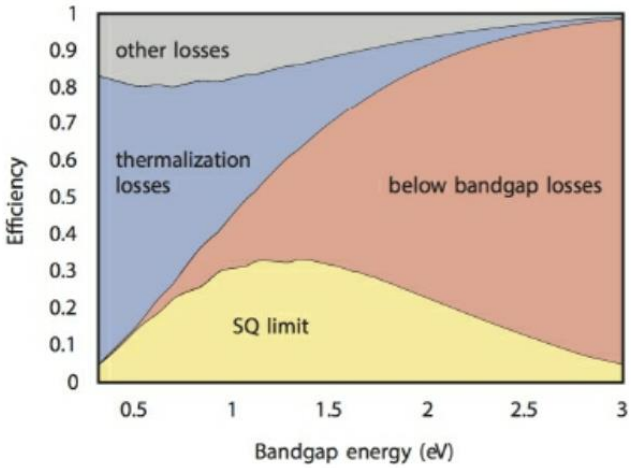

Figure 16: Loss mechanisms in SQL using AM1.5 as incident spectrum [3]

However, the SQ limit is not applicable to c-Si solar cells as they consider only radiative recombination in direct bandgap materials, whereas in c-Si, due to its indirect bandgap nature, Auger recombination is the major recombination mechanism. The SQ limit neglects *optical losses* as well.

2.4.2 Optical losses

The efficiency of the solar cell is also dependent on the optical properties governed by the refractive index ($\tilde{n} = n - ik$) which is wavelength dependent. Due to the variation in refractive index at a boundary between two materials part of the light reflected and other part is transmitted. The reflectivity and transmittance are wavelength dependent *R(λ)* and *T(λ)*. A solar cell consists of multiple layers and hence there will be multiple reflections at these interfaces. This results in a total reflectance between the solar cell and the surrounding medium. As a result, part of the incident energy which can be converted to electricity is lost. Anti-reflection coatings and texturing can be used to reduce *reflection loss* which is explained in section 2.5.

Solar cells have metal contacts in the front and back to collect the charge carriers. The metals have zero transmittance and thus no light enters through the area beneath the contacts. Thus, the active area of the solar cell is reduced. This is called the *shading loss.* The coverage factor can be written as $C_f = A_f / A_{tot}$ where A_f is the area not covered by metal and A_{tot} is the total cell area. However, designing thinner contacts will increase the series resistance. Therefore, contacts should be designed in an optimal way with high coverage factor and low series resistance.

Light is absorbed in all the layers of the solar cell as it transmits. The loss resulting from absorption in layers other than the absorber layer is called *parasitic absorption. Incomplete absorption* can also occur due to the limited thickness of the absorber [3].

2.4.3 Additional losses

Efficiency can reduce due to increased *series resistance* R_S of a solar cell. Contact resistance between the metal semiconductor junctions, resistances of metal electrodes, bulk resistance in the junction contributes to the series resistance which results in a voltage drop. Leakage currents due to the *shunt resistance* R_P of the solar cell also causes a drop in voltage. Along with radiative recombination, non-radiative recombination mechanisms such as the *Shockley-Read-Hall* and *Auger* recombination as well as *surface recombination* results in a decrease in fill factor will in turn causes a drop in the efficiency [3] [28].

2.5 Light management

To effectively reduce the losses mentioned in section 2.4, three design rules are defined:

(i) Bandgap utilization
(ii) Spectral utilization
(iii) Light management

For this thesis, the concept of light management is of the utmost importance and hence will be discussed in this section.

In an absorptive media, lambert-beer law describes how light intensity exponentially decreases as it travels through it. The intensity of light absorbed is given by:

$$I^{abs}(x) = I_0(1 - e^{-\alpha x}) \tag{2.24}$$

Where x is the distance travelled, α is the absorption coefficient and I_0 is the initial intensity. It follows that more light is absorbed at the back side with respect to the front side where the light enters from. Therefore, to absorb all the light, the absorber layer should be *optically thick*. The absorption coefficient of the blue part of the spectrum is much higher than that of the red part of the spectrum for all the semiconductor materials, as a result the blue part gets readily absorbed in the first few nanometres in a c-Si absorber. However, to absorb the red light effectively, a thickness of 60μm is needed, whereas a thickness on 100μm, only 10% of the IR spectrum is absorbed. c-Si is generally is a poor absorber due to its indirect bandgap nature and having a high direct bandgap at 3.4eV. In thin-film technology a-Si:H is an attractive absorber compared to c-Si. By varying the deposition conditions, the bandgap of the a-Si:H is tuneable, has a better absorption coefficient in the visible spectrum due to its direct bandgap nature due to which thinner absorber layers can be realized and it is relatively easy to dope [29]. The absorption coefficient of a-Si:H and c-Si H over the wavelength range is shown in Figure 17.

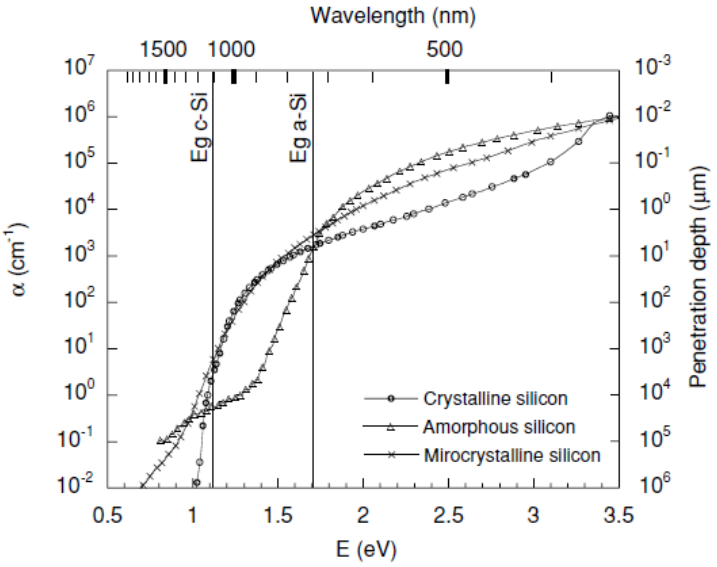

Figure 17: Absorption coefficient versus wavelength [29]

Due to the high intragap state density in a-Si:H (< 10^{16} cm^{-3}) and high dangling bond densities, carrier lifetimes are lower (higher recombination). A low doped intrinsic layer is sandwiched between the thin p+ and n- layers as a 'drift zone' for better carrier collection. However, the material still suffers from creation of metastable defects due to *Light Induced degradation (SWE)* mentioned in section 1.2, which reduced the electric field in the intrinsic layer. Hence, the thickness should be reduced to collect the charge carriers before they can recombine. This however will result in low absorption of light (based on eqn. 2.24). Hence, to make the absorber physically thin and optically thick (so that the light can traverse a higher optical path length), optical confinement techniques required to improve light absorption in all wavelengths.

Similarly, nanocrystalline silicon is another phase of hydrogenated silicon alloy which consists of small grains with a crystal lattice embedded in a tissue of a-Si:H. μc-Si:H is found to be less prone to SWE and thus more stable than a-Si:H. However, it has a lower absorption coefficient due to its crystalline nature (indirect bandgap), in the visible range. Thus, a thicker layer of μc-Si >1mm compared to the

300nm required in a-Si. Hence, light management techniques become even more important in micro/nano crystalline silicon solar cells [29] [3].

It is crucial to reduce other optical losses as well. Reflection can be reduced by using *anti-reflective coatings (ARC).* Introduction of an intermediate layer with a refractive index n_i which has a value between the refractive indices of the two layers it is sandwiched between n_1 and n_2 results in minimal reflection. n_i can be written as:

$$n_i = \sqrt{n_1 n_2} \tag{2.25}$$

Introduction of additional intermediate layers called as *refractive index grating* can further reduce the loss by reflection [3].

The concept of *constructive and destructive interference* can also be used to design ARCs. When two waves are superimposed (from the same source or from 2 different coherent sources), if the phase shift between them is *in phase* (i.e. a multiple of 2π), the waves are said to be in constructive interference and will have maximum amplification. If they are *in antiphase* (or from incoherent sources), they will interfere deconstructively and will have maximum attenuation. The ARC at the front side of the solar cell should be designed in such a way that the light wave reflected from the air-material and air-electrode should be in destructive interference such that the irradiance that is coupled out of the cell is minimal. Similarly, at the back side of the solar cell, the back reflector should be designed in such that the waves reflecting from the reflector should be in constructive interference so that maximum irradiance is coupled back into the cell, thus increasing the optical path length of the light.

Another approach is to have *textured interfaces* which enhances in coupling of light into the solar cell. Light incident on one part of the texture, can reflect light diffusively such that the diffused light can incident on another part of the texture such that another fraction of light gets transmitted into the cell. This way the total reflection is reduced. The basic concept of texturing is illustrated in Figure 18.

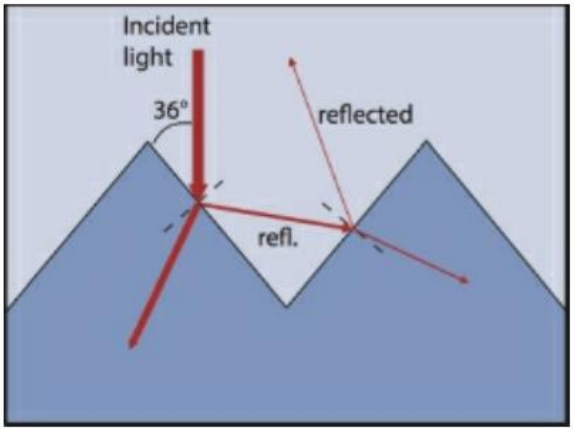

Figure 18: Concept of texturing [3]

2.5.1 Thin-Film roll-to-roll production

In a large-scale production, cost effectiveness is an important parameter. The product of maintenance costs of a machine and the time required per square meter for depositing a stack of multilayers should

be small. Thus, it is not possible to have very low deposition rates. Multiple process configurations are available [30]:

(i) *Single chamber system*: The advantage is that, under vacuum, there is no transport of substrates. Also, larger substrates are possible, and the cost of investment is lower. However, the time required for production is higher since multiple purge and pump down steps are needed. Also, the limited possibilities for applying buffer and graded layers and the deposition temperature cannot be varied

(ii) *Multi-chamber system*: Graded layers and temperature control are possible in this configuration. However, the panel sizes are limited, and the cost of investment is higher

(iii) *Roll-to-roll process*: All the layers are deposited onto a long flexible substrate which moves from one deposition zone to another which are connected to each other. A high throughput can be achieved with this technology and multiple layers can be deposited in a single pass.

In the Flamingo-PV project, as mentioned in section 1.2, R2R technology is used. These cells can be deposited in *superstrate* or *substrate* configuration. In *superstrate* configuration the cells are deposited in p-i-n stack where light enters from the p side first. A glass coated with a TCO film which acts as a transparent carrier is used in this configuration. It should be optically transparent (no parasitic absorption), have good lateral conductivity, low sheet resistance, withstand high deposition temperatures and chemical stability. The glass can be textured to ensure less reflectivity and good light trapping. The textured TCO also enhances the light absorption due to scattering at the rough interfaces. Fluorine doped tin oxide (SnO_2:F/FTO) are naturally textured TCOs used widely in TF solar cells. The glass substrates can withstand the high APCVD deposition temperatures (500-600°C) of the FTO. However, this cannot result in a flexible cell. Currently no flexible transparent foils of low cost are available as a superstrate carrier. In the *substrate* configuration, the layer in which light enters first is deposited last. The carrier can be opaque carriers such as metals or polymers which enables the R2R production technology. Flexible solar cells can be made using this configuration. Stainless steel is widely used as a substrate, but monolithic integration is not possible on this. Polymers such as polyimide are widely used as well, which are temperature resistant but expensive [29].

As mentioned in section 1.2, HyET's technology uses Aluminium as a temporary carrier. FTO is deposited onto the 110μm foil. The foil can withstand the high deposition temperature of APCVD FTO and provides good mechanical stability for the deposition of subsequent layers. Due to the abundant nature of aluminium, the cost is lower as well. The foil is textured to realize micro sized craters before the deposition of other layers. After deposition of the layers, the temporary foil is etched away using wet etching method which exposes the FTO. The FTO is resistant to most etchants so that it functions as an etch barrier to the other layers [6] [31].

2.5.2 Scattering

As mentioned before, thin film solar cells have textured interfaces for efficient light trapping to enable absorption in thin absorber layers. The texturing can be random or periodic. These textures enable scattering of light. Scattering is the mechanism by which causes a change in the direction of light as it interacts with small particles. When the particles are relatively small in the range of 0.3 μm or less, scattering occurs by diffraction. Whereas, when the particles are relatively larger (higher than 2 μm),

scattering occurs by refraction and reflection. It was also proposed by Lord Rayleigh that for scattering, it's not necessary for these particles to exist, variations in refractive indices can also result in scattering [27].

There are different types scattering regimes. This can be classified using the small size parameter approximation given by [32]:

$$x = \frac{2\pi r}{\lambda} \tag{2.26}$$

Where r is the radius of the particle and x is a dimensionless parameter. Particles with x << 1, the mechanism is Rayleigh scattering. When x ≃ 1, the mechanism is Mie scattering and when x >> 1, macroscopic scattering.

(i) *Rayleigh scattering*: Particles with sizes much smaller than the wavelength of photons are responsible for Rayleigh scattering ($nd \ll \lambda$). The light is scattered in all angles and is elastic in nature, i.e. there is no change in wavelength during scattering. The intensity of Rayleigh scattering can be written as:

$$I(\theta) = I_0 \left(\frac{2\pi}{\lambda}\right)^4 \left(\frac{{n_p}^2 - {n_0}^2}{{n_p}^2 + 2{n_0}^2}\right) \left(\frac{d}{2}\right)^6 \frac{1+cos^2\theta}{2R^2} \tag{2.27}$$

From the equation, it can be seen that the scattering is strongly dependent on the wavelength. The sky appears blue because of this: since the atmosphere is full of oxygen and nitrogen particles with diameter much smaller than the wavelengths, blue light is scattered much effectively

(ii) *Mie scattering*: When the particle sizes are comparable to the wavelength ($nd \approx \lambda$), the mechanism is Mie scattering. This is elastic in nature as well. This is mainly defined for spherical particles and occurs mainly in the forward direction and is less dependent on the wavelength and hence scatters blue and red light. The angular intensity distributions of Rayleigh and Mie scattering is shown in Figure 19. The diffuse transmittance T_D can be described by [9]:

$$T_D = \frac{\pi a^2}{{L_C}^2} Q_{scatt} \tag{2.28}$$

Where L_C is the correlation length, Q_{scatt} is the scattering efficiency and πa^2 is half of the peak to peak height of the cross section of the texture.

(iii) *Macroscopic scattering:* When the particle sizes are higher than the wavelength, macroscopic scattering occurs which involves reflection and refraction.

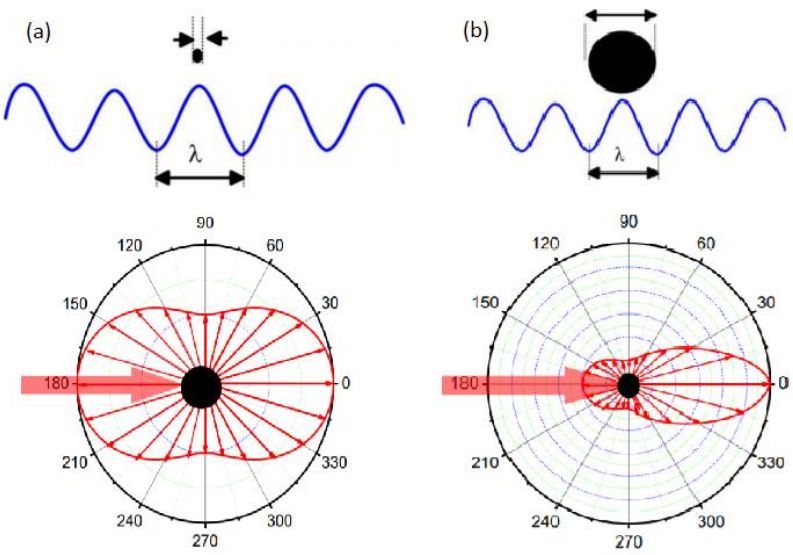

Figure 19: Angular intensity distribution of (a) Rayleigh scattering and (b) Mie scattering [33]

These scattering mechanisms are used in the design of solar cells to develop *targeted scattering.* In an a-Si:H/µc-Si:H micromorph cell, the top amorphous layer is responsible for absorbing the blue light and can be realized using small nano textures (~400nm) which effectively scatters blue light. The red light gets transmitted and can be scattered by macro sized textures (up to 2µm) thus increasing the optical path length of red light. This is depicted in Figure 20. In modulated surface texturing by combining different texturing features, scattering mechanisms can also be superimposed as mentioned in section 1.3.

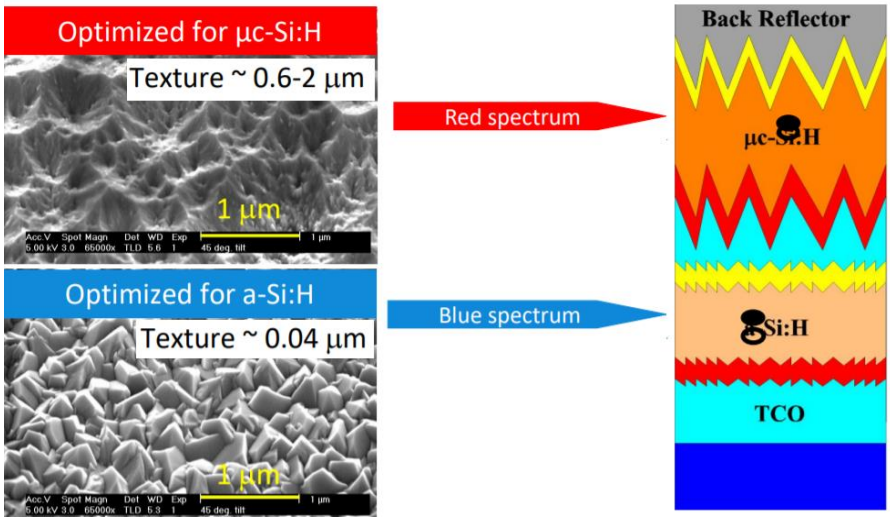

Figure 20: Targeted scattering for a-Si:H/µc-Si:H micromorph cell [33]

Scattering nano textures can be modelled using *scalar scattering theory* as shown in [34]. The diffuse transmittance T_D can be written as:

$$T_D = T_0 \left\{1 - exp\left[-\left(\frac{2\pi\sigma_{rms}|n_0 - n_1|}{\lambda}\right)^{\gamma}\right]\right\} \tag{2.29}$$

Where σ_{rms} is the rms roughness, γ ranges from 1.5 to 3 depending on the height distribution function, n_0 and n_1 is the refractive indices of the interface materials and T_0 is the total transmittance [9]. *Ray tracing* model can be used to model scattering by particles with sizes much higher than the wavelength. This is applicable for spherical and non-spherical particles. Here, the light is considered as *rays* which gets reflected and refracted [35].

Lambert-cosine law states that the intensity (I) of light observed at an area dS is directly proportional to the angle between the surface normal and the direction of the incident light denoted by θ. Such a scattering surface which obeys the Lambert-cosine law is called a *Lambertian scatterer.* The power (I x dS) reflected by a Lambertian scatterer, when viewed from any angle, will be equal. *Eli Yablonovich* theorized the maximal absorption enhancement limit in 1982 which is based on maximizing the area from which light can incident at a point in the bulk of an absorber material. Assuming the reflectivity of the front surface to be zero and introducing front surface texturing such that the front surface is a Lambertian scatterer, yields an absorption enhancement of $2n^2$. For silicon, this value is 25 which implies, the light makes 25 passes in the absorber before escaping. If an ideal back reflector is also introduced along with the front Lambertian scatterer, the enhancement is $4n^2$ [33] [36].

3 Experimental details

3.1 Texturing by wet chemical etching

Texturing increases the optical path length which improves light trapping in solar cells. These textured surfaces can be achieved by *etching*. Etching can be *wet chemical etching, dry etching, patterning* etc. In wet etching process, the chemical solution- the *etchant* is sprayed on the surface of the substrate or the substrate is dipped in the etchant [37]. Dry etching also known as plasma etching involves bombardment of ions on the substrate. *Reactive ion etching (RIE)* is a common type of dry etching. Materials like silicon, silicon dioxide, aluminium, etc. can be both wet etched or dry etched and both technologies have its advantages and disadvantages. Wet etching is a simple process compared to dry etching and thus requires much less capital and in batch mode, has a higher throughput. Wet etching also shows excellent *selectivity* [38].

There are various metrics that can be used to characterize etching [39] [40]:

(i) The rate at which the material is removed given the etching conditions such as temperature, concentration of the etchant, etching time etc. is called the *etch rate* usually expressed as μm/min or nm/min. Higher the etch rate, the less controllable the process

(ii) The ratio of etch rates between two materials can be defined at the *selectivity.* A higher selectivity ensures that the selected layer gets removed without affecting the underlying layer. For example, KOH etchant has a selectivity of 1000 to 1 for polysilicon over oxide. This means that the KOH etches the polysilicon 1000 times faster compared to the oxide

(iii) *Etch uniformity* refers to the variation in etch rates across a substrate or from one substrate to the other. It can be expressed as:

$$etch\ rate\ uniformity\ (\%) = 100 \times \frac{etch\ rate_{max} - etch\ rate_{min}}{etch\ rate_{max} + etch\ rate_{min}} \tag{3.1}$$

(iv) *Degree of anisotropy (A)* can be expressed in terms of the etch rate in lateral (R_L) and vertical (R_V) directions, given as:

$$A = 1 - \frac{R_L}{R_V} \tag{3.2}$$

Etching can be *isotropic* or *anisotropic.* If the etching rate is same in all the directions, then the etching is isotropic, i.e. it does not have a directional dependence. When the etch rate is different in the lateral and vertical directions, i.e. it is direction/orientation dependent, then the etching is anisotropic. The wet etching process is usually isotropic in nature except for crystalline materials. Isotropic etching of silicon can be achieved using HF, HNO_3, H_3PO_4 etc, or its mixtures. Using KOH, it is possible to achieve anisotropic etching of silicon. KOH can etch the (100) plane faster than the (111) orientation. The atoms in (111) has stronger binding forces hence the lower etch rate. A spherical form can result from an isotropic etch if the solution is stirred properly [37] [41]. Figure 21 shows isotropic and anisotropic etching.

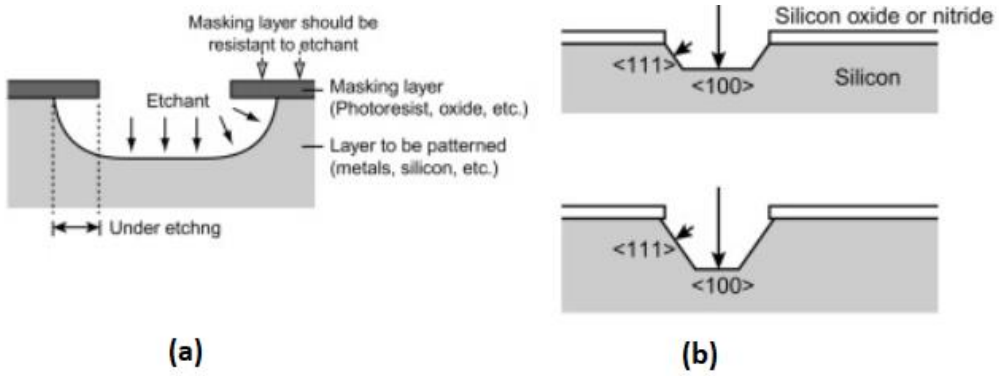

Figure 21: (a) isotropic (b) anisotropic etching [41]

The wet etching process consists of multiple processes. First, mass transport, i.e. diffusion of the etchant occurs towards the substrate to be etched. The etchants are adsorbed at the active areas of the substrate which leads to a chemical reaction between the etchant and the active areas resulting in by-products of the reaction. These by products will diffuse away from the surface back to the solution. This mechanism is depicted in Figure 22. The etch rate is determined by the etchant concentration, temperature, time and the rate at which the by products are removed from the surface. If the by products are not soluble, it can adhere to the surface which will prevent etchants from entering the surface.

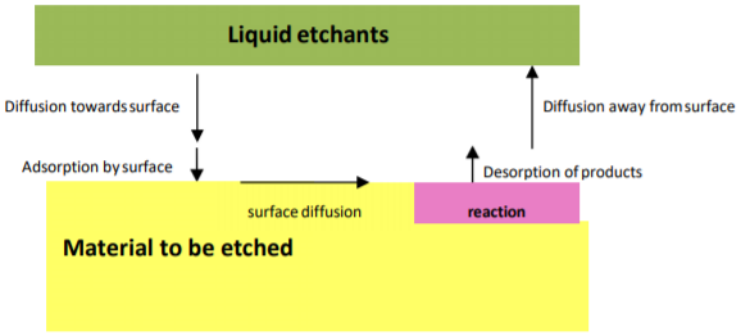

Figure 22: Mechanism of wet etching [40]

As explained in section 1.3, glass can be etched isotropically using various etchants (HF, HNO_3, HCl etc.) to achieve textures as well.

3.1.1 Bare Al texturing

An aluminium foil is used as a temporary substrate on to which all the other layers are deposited. The aluminium is textured using wet chemical etching to achieve features for light trapping. The initial thickness of the foil before etching is measured to be 107-110µm. In this thesis, two approaches have been used to texture the foil. The first one is to directly etch the aluminium in different etchants. Acids and bases are used as etchants for the direct texturing of the foil. [42] [43] [44] has reported the use of phosphoric acid, nitric acid, sodium hydroxide etc as aluminium etchants.

A combination of phosphoric and nitric acid mix at 90°C is used and etched for 60s and 150s. This however is not used further as it resulted in sharp pyramidal V-shaped textures (shown in section 4.2).

Sodium hydroxide (NaOH) and potassium hydroxide (KOH) etchants resulted in crater or U-shaped textures. Mixtures of KOH:H_2O and NaOH:H_2O with concentrations varying from 20 g/L to 100 g/L with temperatures ranging from 35°C to 70°C are experimented. The etching times are varied from 30 s to 4 minutes. After etching the aluminium foil in the designated etchant, it is immediately rinsed in warm/flowing water after which it is immersed in 1% of H_3PO_4 for cleaning. The acid is kept at 70°C and the foil is cleaned for 45s to 1 minute. The etching reaction creates by-products termed as '*smut*' which sticks to the foil and hence the cleaning using phosphoric acid. For example, when aluminium reacts with NaOH, it is an exothermic reaction, i.e. it generates heat. It also generates free hydrogen (which is froth or bubbles) and oxides and hydroxides of aluminium. Since the aluminium is not 100% pure, it can contain other alloy elements like iron, manganese, silicon etc. which also produces intermetallic components which are insoluble in the solution. This grey layer, loosely sticks to the foil as well as to the tank walls, termed as smut. Hence, after etching and rinsing a *de-smutting* step with an acid [45] [46] [47]. As mentioned, the hydrogen bubbles and smut adhere to the surface of the foil and inhibits etching which results in non-uniformity. Therefore, in further experiments, '*chelating agents*' and '*surfactants*' such as metal (Na or K) gluconic acid salts and polyethylene gluconate are added along with the etchants to investigate the uniformity of etching.

3.1.2 Sacrificial layer texturing

In sacrificial layer etching, layer of AZO or ITO is deposited on to the aluminium foil before the wet etching step. These are deposited using sputtering at a temperature of 200 and 500°C. This type of etching is inspired by [8] [18]. Acid (HF) and alkaline (NaOH and KOH) etching is done at room temperature, 35°C, 50°C and 60°C for 2 minutes.

3.2 Optical characterization

To estimate the effectiveness of texturing, optical characterization of the sample is important. Since the aluminium has zero transmittance, the reflection properties are used to characterize the samples, which are *total reflectance (R_{Tot}), diffuse reflectance (R_{Diff}) and reflective angular intensity distribution (AID_{Refl}).* These three parameters were measured for each sample from 300 nm to 1200 nm. A *PerkinElmer® Lambda™* 950 *spectrophotometer* and *PerkinElmer® Lambda 1050 spectrophotometer* available at the PVMD group TU Delft, are used to perform these measurements.

3.2.1 Integrating Sphere (Reflectance setup)

The lambda 950 and 1050 spectrophotometer host the *Integrating Sphere (IS)* for the reflectance set up which is capable of measuring wavelength dependent total and diffuse reflectance and transmittance. As mentioned above, for this thesis, only the reflectance part is considered. The setup is shown in Figure 23. For the reflectance measurement, the sample is mounted in sample holder as shown in the figure, in the rear part of the chamber. Monochromatic light is incident on the sample which is placed at an angle of 5° so that the reflected ray does not interfere with the incident ray. As mentioned in section 2.3.2, from rough surfaces, the reflected rays consist of a specular (R_{Spec}) and diffuse part (R_{Diff}). By opening a port (next to the light entrance at 5°), the specular part of the reflection can be removed since it obeys $\theta i = \theta r$. This way, diffuse reflectance can be measured. The

effectiveness of scattering is determined by *haze factor. Reflectance haze* is considered here, which is the ratio of diffuse reflectance to total reflectance given by:

$$H_{Refl} = \frac{R_{Diff}}{R_{Tot}} \tag{3.3}$$

Similarly, *transmittance haze* can be written as:

$$H_{Tra} = \frac{T_{Diff}}{T_{Tot}} \tag{3.4}$$

It is important to measure the diffuse and total reflectance at the same spot in the sample since the sample is non-uniform.

Figure 23: The Integrating Sphere setup [48]

3.2.2 ARTA (Angular Intensity Distribution setup)

The spectrophotometer hosts an accessory for measuring the angular intensity distribution of the sample, called the *ARTA-Automatic Reflectance/Transmittance Analyser.* Due to scattering, light is reflected/transmitted in all angles. In the fixed sample position, the setup detects the intensity of the light at all angles by the rotating detector which hosts an integrating sphere. Since the transmittance of the aluminium foil is zero, only the reflectance is considered. For the measurements, fixed sample mode is selected, and the sample is fixed at 10°. The detector is connected to the sample stage by a stepper motor and is programmed to move around the sample from 10° to 100° and from 280° to 350° which covers the full reflected angles. The sample is fixed at 10° to ensure that the specular angle is 20° from the starting point of the detector so as the incident and reflected ray does not interfere. The angles between 350° and 10° are not reachable by the detector. The setup is shown in Figure 24.

Figure 24: The ARTA setup [48]

The angular intensity distribution function is angle as well as wavelength dependent. The intensity of the light can be calculated as $I = I_0 10^{-A}$ where A is the absorptance given by the ARTA. The obtained values are normalized for comparison.

3.3 Surface morphology characterization

3.3.1 Atomic Force Microscopy

This is a tool to measure the surface morphology. A cantilever having a tip at the end interacts with the sample. This assembly is referred as the probe. As the probe scans over the surface, the cantilever gets deflected due to the forces between the surface and the probe and the amount of light reflected into the photodiode off the probe varies and the surface morphology is measured. For this thesis, an *NT-MDT® NTEGRA* AFM at the EKL and *Bruker ScanAsyst®* at the Kavli Nano lab are used for the measurements. Due to the high roughness and adhesive nature of the sample *Tapping mode* in the NTEGRA AFM and *ScanAsyst mode* in the Bruker AFM is used. In the tapping mode, the cantilever oscillates close to its resonant frequency normal to the surface of the sample. As the oscillating cantilever approaches the surface, the amplitude of oscillation varies as a response to the interacting forces between the sample and the tip. In the scanasyst, a *PeakForce Tapping* mechanism is used which intermittently contacts the surface but resonates at a frequency lower than the resonant frequency. It also automatically optimizes the feedback gain, set point (minimum force required to track surface of samples) and the scan rate [49] [50].

The AFM image obtained corresponds to the height values *z* at points *x* and *y* of a specified scan size. The parameters used for the AFM image characterization are the *root mean square (RMS) roughness* (σ_{RMS}), *Auto-correlation length (Lc)*, *aspect ratio* ($AR=\sigma_{RMS}/Lc$), and *mean slope* (θ_M). These parameters can be found using the user interface softwares- NT-MDT® Nova and Bruker NanoScope Analysis. The RMS roughness is an indicator for the vertical height of a surface feature. The autocorrelation length indicates how wide a feature can be and uses auto-correlation function (ACF) to correlate the height values between various horizontal points on the surface. The AR and the slope are indicators of how steep the features are. A higher AR and a higher slope indicate a steeper feature. For each sample, at least 3 sets of measurements are taken to calculate these parameters and analyse the error bars.

3.4 GenPro4 Simulations

GenPro4 is an optical simulation tool which considers the multiple layers in a solar cell and calculates the amount of light absorbed. This tool takes into account flat and textured interfaces which can be given as an input AFM file for light trapping calculations done by wave and ray optic models. The layers of the solar cell can be modelled as '*coating*' which are thin compared to the coherence length of sunlight, i.e. 1µm and thus interference is considered. The layers can also be modelled as '*layer*' when these layers are thicker than the coherence length and thus interference is not considered.

For a flat interface, each layer can be modelled by a thickness d_i and a R.I. $N_i=n_i+ik_i$ where i indicates the layer or the interface. For normal incidence, the transmittance of layers and the reflectance of interfaces can be calculated using Lambert-Beer law and Fresnel equations as:

$$\tau_i = e^{-(4\pi k_i/\lambda)t_i} \tag{3.5}$$

$$r_i = \left|\frac{N_i - N_{i+1}}{N_i + N_{i+1}}\right|^2 \tag{3.6}$$

These equations are further modified for other angle of incidences. The multiple reflections occurring at interfaces are calculated using '*net radiation*' method which is shown in Figure 25. Four fluxes denoted by q_i^x (in W/m^2) where a, b, c and d show if the light is entering or leaving the interface. These fluxes can be related as:

$$\begin{cases} q_i^a = \tau_i . q_{i-1}^d \\ q_i^b = r_i . q_i^a + t_i . q_i^c \\ q_i^c = \tau_{i+1} . q_{i+1}^d \\ q_i^d = t_i . q_i^a + r_i . q_i^c \end{cases} \tag{3.7}$$

Where t_i=1-r_i. For the first interface q_1^a is set to 1 since all light is incident from the top and q_1^c is set to 0 since no light is incident from below. These approximations are substituted in eqn. (3.7) to derive other fluxes and the R, T and A can be obtained as:

$$R = q_1^b \tag{3.8}$$

$$T = q_1^d \tag{3.9}$$

$$A_i = q_{i-1}^d - q_{i-1}^c + q_i^b - q_i^a \tag{3.10}$$

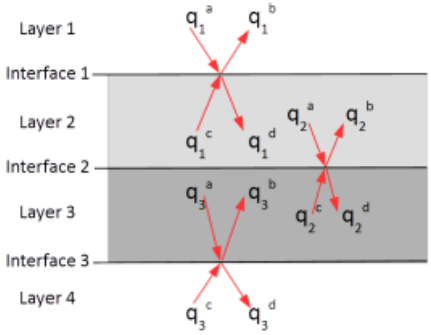

Figure 25: Net radiation flux [51]

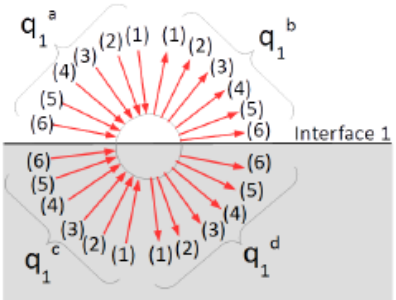

Figure 26: Net radiation sub-fluxes depicted using 6 intervals [51]

For this thesis, we have used the GenPro4 model to simulate the textured interfaces. Thus, the reflected and transmitted light do not have a well-defined direction of propagation and are distributed over a range of angles from 0° to 90° i.e. perpendicular and parallel to the interface, respectively. This range is divided into 30 intervals such that one interval corresponds to 3° (shown in Figure 26). These intervals are denoted by '*v*' and the sub-flux can be represented as $q_i^x(v)$ which is grouped into a vector $\boldsymbol{q}_i^x = [q_i^x(1),\ q_i^x(2), \ldots\ldots\ldots q_i^x(v)]$. Thus eqn. (3.7) can be written as:

$$\begin{cases} \boldsymbol{q}_i^a = \boldsymbol{\tau}_i . \boldsymbol{q}_{i-1}^d \\ \boldsymbol{q}_i^b = \boldsymbol{r}_i{}^+ . \boldsymbol{q}_i^a + \boldsymbol{t}_i{}^+ . \boldsymbol{q}_i^c \\ \boldsymbol{q}_i^c = \boldsymbol{\tau}_{i+1} . \boldsymbol{q}_{i+1}^d \\ \boldsymbol{q}_i^d = \boldsymbol{t}_i{}^+ . \boldsymbol{q}_i^a + \boldsymbol{r}_i{}^- . \boldsymbol{q}_i^c \end{cases} \tag{3.11}$$

The letters indicated in bold shows that they matrices having a size of *v x v*. the '+' and '-' symbols denotes if the light is incident from top or bottom. The $\boldsymbol{r}_i$ and $\boldsymbol{t}_i$ are the '*scatter matrices*' which are calculated from the morphology of the surface. If the surface morphology has features which are larger than the wavelengths, then the tool uses '*ray optics*' model to calculate the scatter matrix which uses ray tracing. If the features are smaller than the wavelength, '*wave optics*' model is used which uses scalar scattering model as shown in section 2.5.2 [51].

4 Results and discussions

4.1 The factory baseline

The R2R production at HyET uses wet chemical etching for texturing the aluminium foil. The etchant used is sodium hydroxide with additives. The recipe of the etchant used is: 4 g/L (0.1 mol/L) of NaOH, Sodium nitrate, sodium gluconate and polyethylene glycol 400 (PEG-400) are added as well. The components other than NaOH are referred to here as 'additives' and act as chelating agents and surfactants (mentioned in section 4.5). The etching bath has a capacity of 1000 litres and the above-mentioned components are added accordingly. After the etching, the roll is rinsed in warm water in modules attached to the etch bath modules. The warm water aids in cleaning of the smut layer with acids and removes other water-soluble impurities. The roll then passes to the adjacent module where it is subjected cleaning in phosphoric acid. The module has a capacity of 240 litres. This ensures that the smut layer is completely removed from the aluminium. After this the roll is rinsed again in warm water after which the roll is brushed and dried. The rolls are 350 mm wide with varying length.

Figure 27 shows the SEM image of the factory baseline from which it is seen that the features are quite small compared to the targeted values. To characterize the features, AFM imaging was done as depicted in Figure 28. The following are the parameters derived from the AFM data:

- *RMS roughness (σ_{RMS}) = 28.4nm*
- *Autocorrelation length (L_C) = 497nm*
- *Aspect ratio (σ_{RMS}/L_C) = 5.7%*
- *Slope (θ_m) = 12.11°*

As stated in section 1.3, the aim is to have an aspect ratio of 12-14% with an L_C of 3-4 μm. If the features are too steep (very high aspect ratio), it will not provide a suitable morphology for high quality nc-Si:H growth, and if the features are less shallow (very low aspect ratio), it will not provide efficient light trapping. In addition, as explained in section 2.5.2, the feature size should be such that it aids in trapping of red light to the bottom cell. Naturally nanotextured FTO is deposited on to the textured Al which adds to the roughness values. Thus, the craters should be wide and smooth enough such that the FTO is deposited in a conformal way adapting the Al texture and superimposing it with the nanotexture as shown in Figure 3.

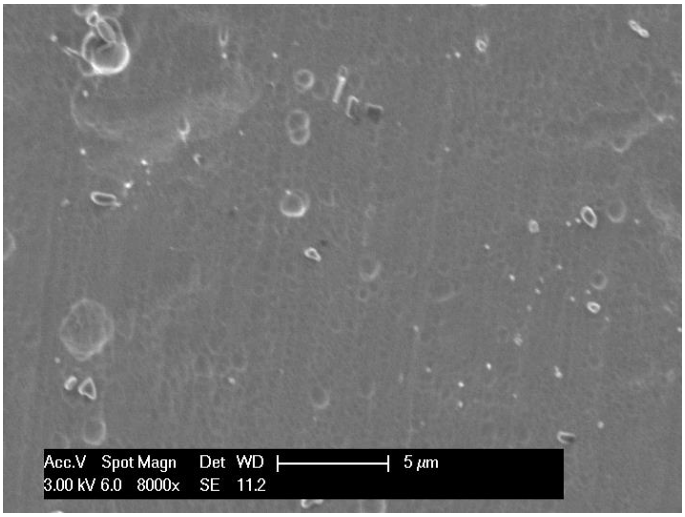

Figure 27: SEM image of factory baseline

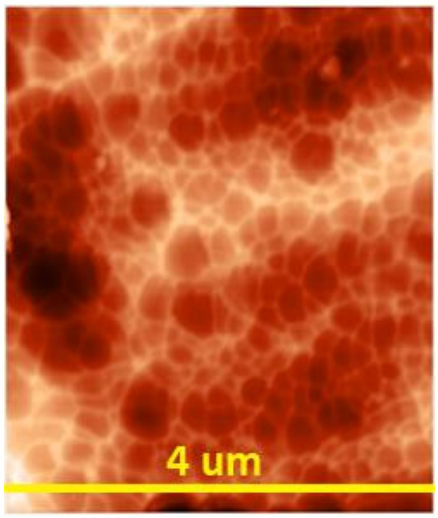

Figure 28: AFM image of factory baseline

Theoretically, as mentioned above, the FTO and the other subsequent layers deposited onto the Al foil should follow the conformality of texturing. Hence, the sample should ideally have a very low reflectance with a high value of haze and should scatter light into larger angles. Thus, reflectance and angular intensity distribution measurements are performed on the Al sample. The reflectance measurement is shown in Figure 29.

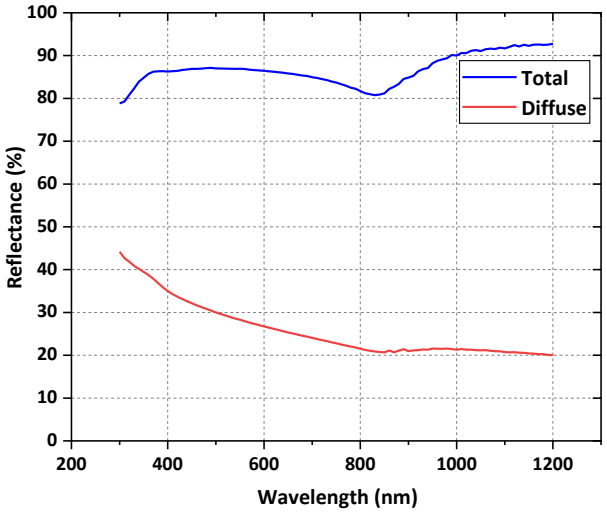

Figure 29: Total and diffuse wavelength of factory baseline sample

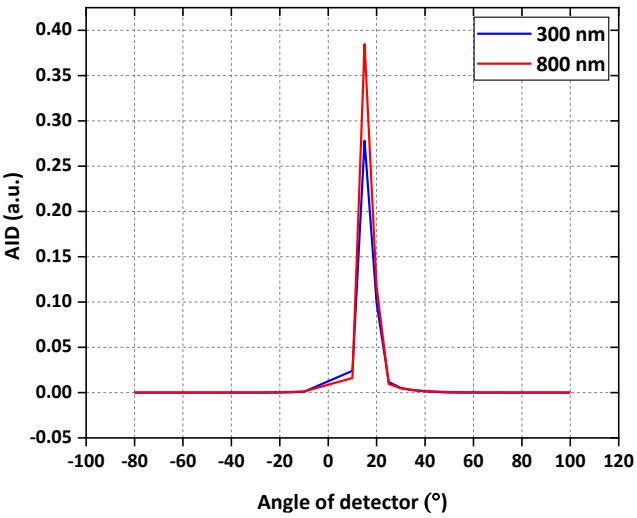

Figure 30: Angular intensity distribution measurement of factory baseline sample

From the image, calculated over the entire wavelength, it can be seen that:

- *Average total reflectance = 86.7 %*
- *Average diffuse reflectance = 25.8 %,*
- *Average specular reflection (total-diffuse) = 60.8 %*
- *Average haze (diffuse/total) = 29.98 %*

From the data, it can be said the sample is highly reflective and a poor scatterer. This can also be observed through visual observation- one's image can be clearly seen reflected from the factory baseline foil. From the graph, it can also be observed that the diffuse reflection is low in high wavelength ranges which implies very small morphologies. This is in line with the AFM data which

showed small features. The comparatively higher diffuse component in the smaller wavelengths can be explained by the smaller features, i.e. scattering is higher when the feature sizes are comparable to the wavelength [52]. This can be seen more clearly in the angular intensity distribution shown in Figure 30. The measurement was done for 300-800 nm in steps of 100 nm. In the image only 300 and 800 nm are shown for comparison. It is seen that the sample is not effective in scattering and the AID is mirror-like.

4.2 Acid Etching

A combination of phosphoric and nitric acid is used as an etchant for texturing aluminium. The temperature is kept at 90°C and etched for 60s and 150s respectively [53]. The 3D AFM images of the samples are shown in Figure 31 and Figure 32. This texturing technique resulted in pyramidal texturing as opposed to crater-like features and hence was not investigated further.

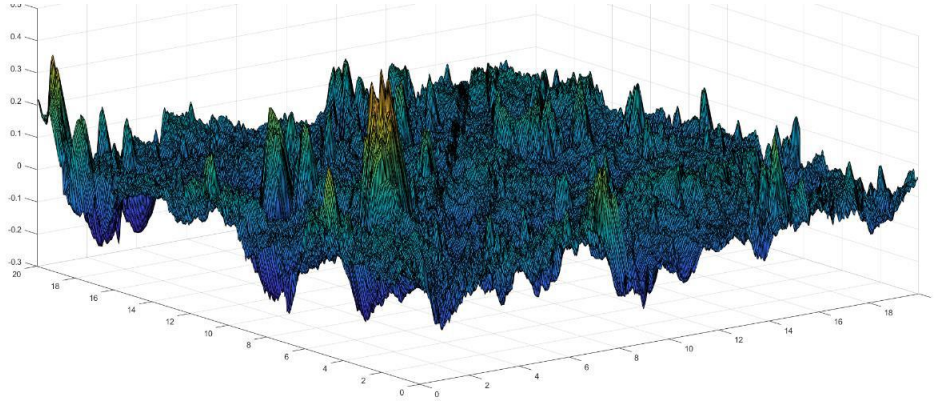

Figure 31: 3D AFM image of Al textured with acid for 60s [53]

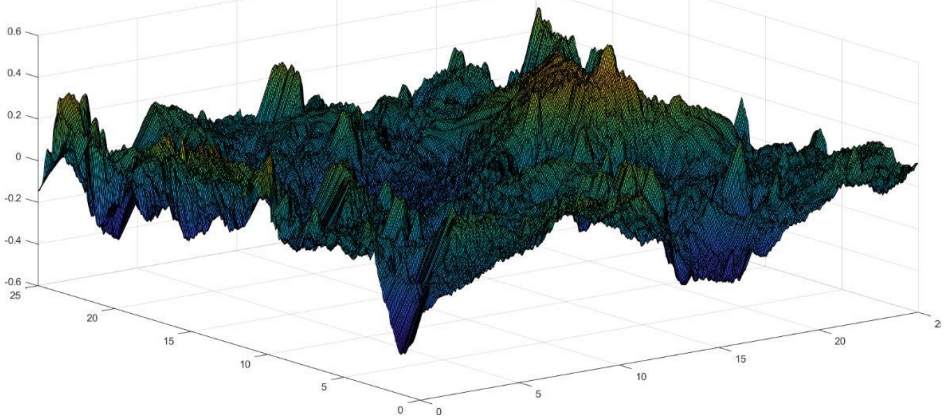

Figure 32: 3D AFM image of Al textured with acid for 150s [53]

4.3 KOH etching

4.3.1 Etching kinetics

KOH and NaOH are the two main etchants used in this project with which craters were obtained. A series of experiments was first done with KOH as it is less reactive with Al compared to NaOH [54] [55]. Hence better controllability of the etching. Time, temperature and concentration series were investigated on the Al foil:

- *Time: 0 min, 1 min, 2 min, 3 min and 4 min*
- *Concentration: 20 g/L, 40 g/L, 60 g/L, 80 g/L and 100 g/L*
- *Temperature: 35°, 50°, 60° and 70°*

To understand the etching mechanics, the above parameters were investigated and the etch rates at different temperatures were measured. Figure 33, Figure 34 and Figure 35 show the thickness of the foil as a function of concentration versus time for a fixed temperature. From these images it can be seen that the etching is highly influenced by the temperature. For the foil etched at 35°C, for the first 2 minutes there is no change in the thickness of the foil, regardless the concentration used. However, after the first 2 minutes, the etching highly depends on the concentration and the etch rate increases with increasing concentration. As the temperature is doubled (i.e. at 70°C), the etching is evident in the first 2 minutes, unlike at 35°C. There is a significant decrease in the thickness of the foil as the concentration increases. A temperature between these two windows can be taken as 50°C and the pattern of the foil thickness is in between that of 35 and 70°C. For lower concentrations, i.e. 20 and 40 g/L, there is no significant change in the thickness of the foil for the first 2 minutes. As the concentration is increases, this window moves towards the left, i.e. at 60 and 80 g/L the foil thickness remains the same for the 1st minute and starts decreasing after that. As the concentration is increased further to 100 g/L, the foil gets etched from the beginning of the process.

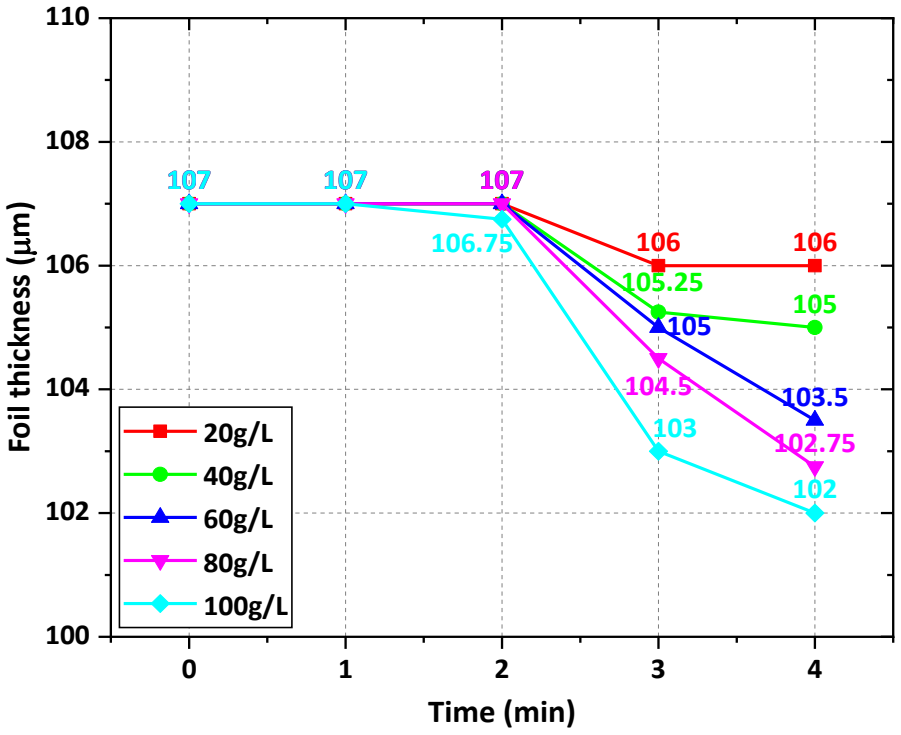

Figure 33: Thickness measurement of Al foil etched with KOH at 35°C

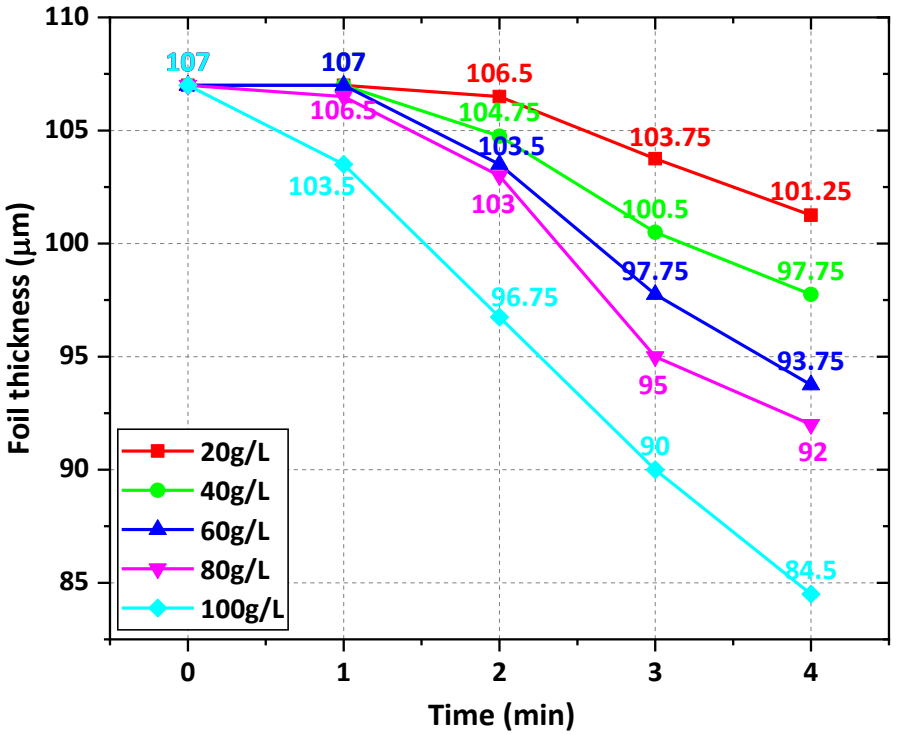

Figure 34: Thickness measurement of Al foil etched with KOH at 50°C

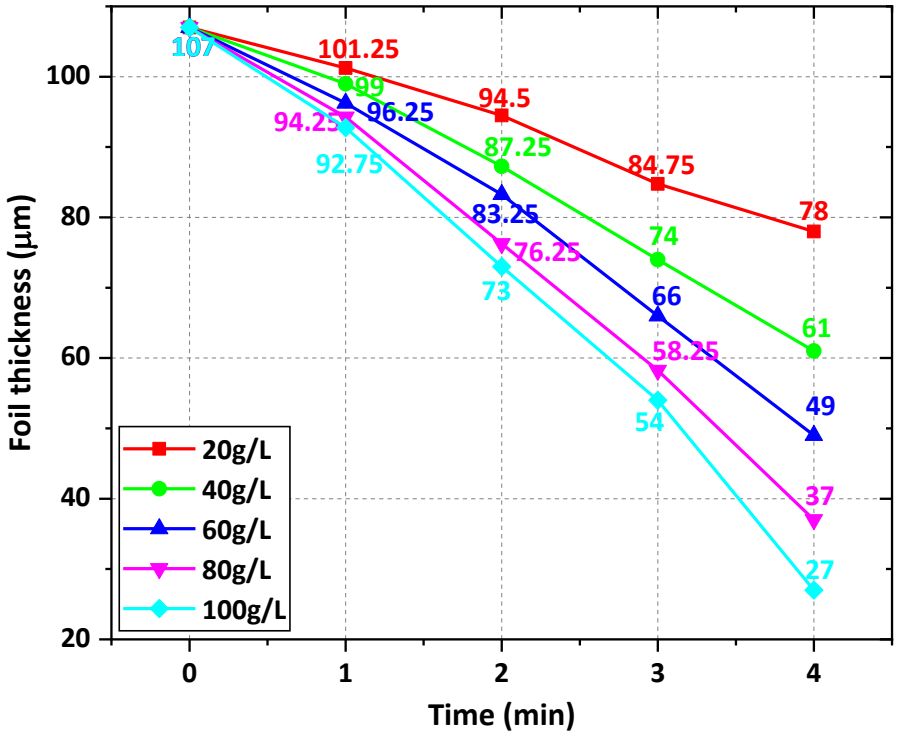

Figure 35: Thickness measurement of Al foil etched with KOH at 70°C

Given the aforementioned results, it can be said that the etching is highly dependent on all three parameters- time, temperature and concentration. For lower temperature, the etching is highly dependent on the time window. For higher temperatures, the etching is dependent on time and concentration. For temperatures in between, the behaviour of etching is in between that of a high and low temperature behaviours. This is shown in Figure 36 where the concentration is fixed at 60 g/L.

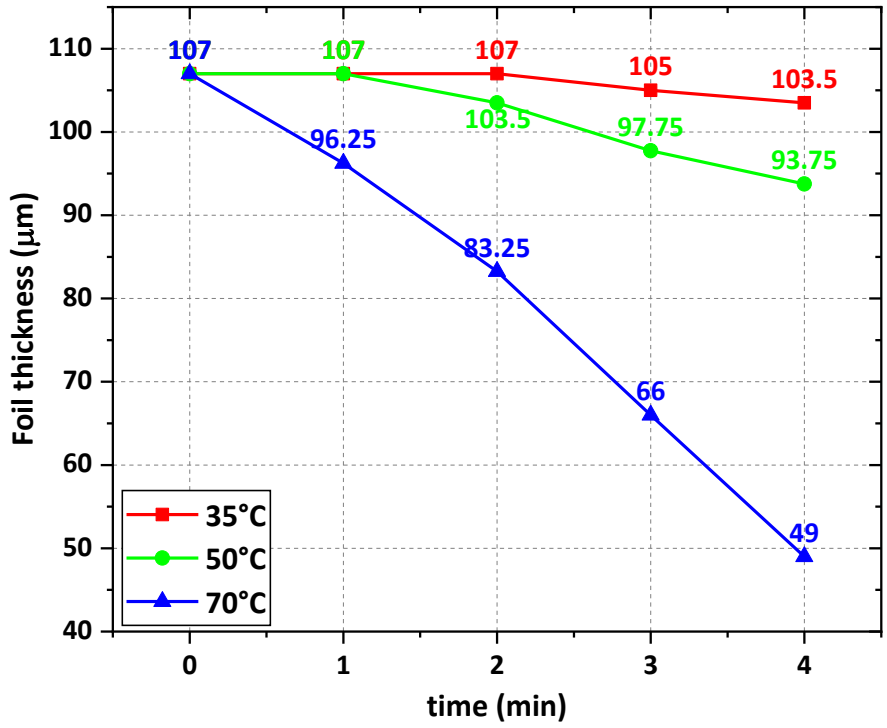

Figure 36: Thickness measurement of Al foil at 60 g/L for different temperatures for etching time till 4 minutes

This trend can be allocated to the presence of aluminium oxide (Al_2O_3) on the foil surface. All metals get oxidised when exposed to air. Thus, a thin layer of oxide is formed on the foil which inhibits the reaction of Al with KOH. This aluminium oxide is inert to neutral and mild acid solutions. However, they dissolve in alkaline solutions. Thus, the time window required to destroy the oxide layer can be defined as the '*induction period*'. This period has been reported to be as high as 90 minutes for 2M (molar) NaOH for an Al disc (99.99% purity) of dimensions 6 mm radius and 2.46 mm thick at a temperature of 25°C. The induction period was reported to reduce with an increase in temperature and concentration as well [56]. The values of the thicknesses for the above mentioned combinations are listed in Appendix 7.1, Appendix 7.2 and Appendix 7.3.

The etch rate of Al with KOH is shown in Figure 37, Figure 38 and Figure 39. Note that the time on x-axis, i.e. 1 indicates the time interval between 0^{th} and 1^{st} minute, 2 indicates the time interval between 1^{st} and 2^{nd} minute. As explained before, the induction period is very evident for lower temperatures and lower concentrations. After the induction period, the following observations can be made regarding the etch rates:

i) For low concentrations (20 g/L, 40 g/L and 60 g/L), despite the temperature, the etch rate increases after the induction period and starts to decrease or saturate after the 3^{rd} minute
ii) For lower temperatures- 35°C and 50°C, this trend mentioned in (i) is observed for all the concentrations
iii) For higher temperature- 70°C, for higher concentrations (80 and 100 g/L) the etching does not saturate
iv) Higher concentrations result in higher etch rates

These can be explained as follows: the reaction between Al and KOH can be written as:

$$Al + OH^- + 2H_2O + \frac{1}{2}O_2 \rightarrow Al(OH)_4{}^- + \frac{1}{2}H_2 \quad (4.1)$$

From the reaction it can be seen that the cation (K+ or Na+) does not directly participate in the reaction but does affect the effectiveness of the hydroxide ion (OH-). When the reaction occurs, the Al surface will contain adsorbed molecules of water, hydrogen bubbles, oxygen and other precipitates of Al metal alloys present in the foil (smut) which can hinder the reaction. The formation of Al precipitate can be written as:

$$Al(OH)^- \leftrightarrow OH^- + Al(OH)_3 \quad (4.2)$$

As the time increases, the (OH-) starts to get consumed more by the Al(OH)- by product and this results in precipitates as shown in eqn. 4.2 which will stick to the foil and hinder the reaction, causing the etch rate to saturate. However, at higher temperatures, there will be an increased movement of the ions and precipitation becomes difficult, hence the etch rate does not get saturated [54] [57]. Hence, the increase in etch rate is directly dependent on the pH of the solution (which depends on the concentration) and on the temperature. Therefore, higher the temperature and concentration, higher the etch rate.

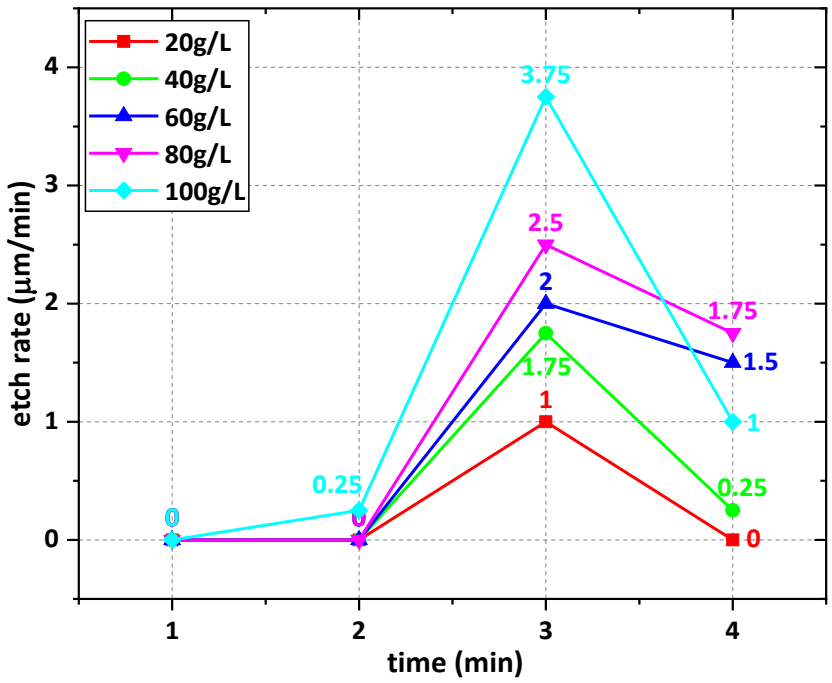

Figure 37: Etch rate of KOH etching of Al at 35°C

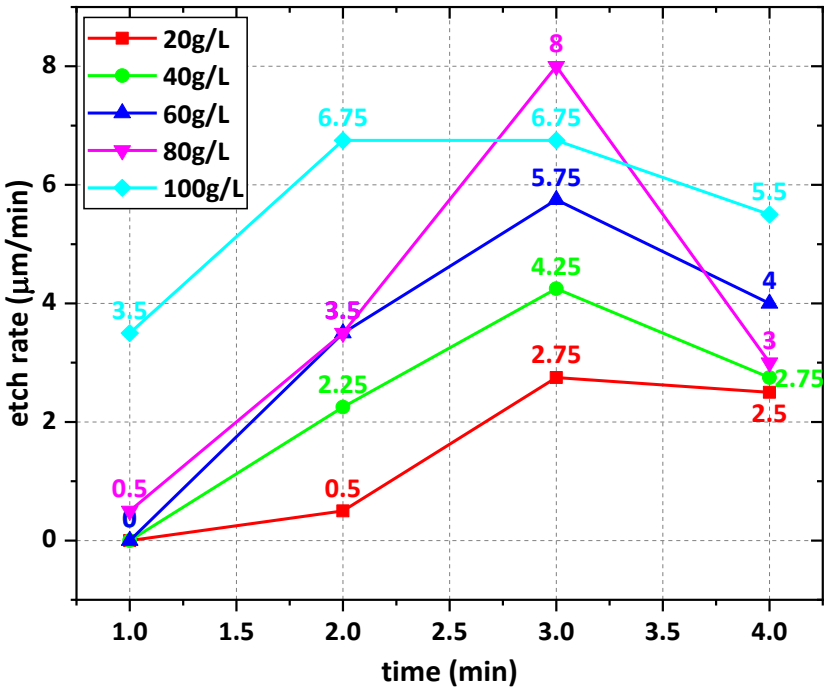

Figure 38: Etch rate of KOH etching of Al at 50°C

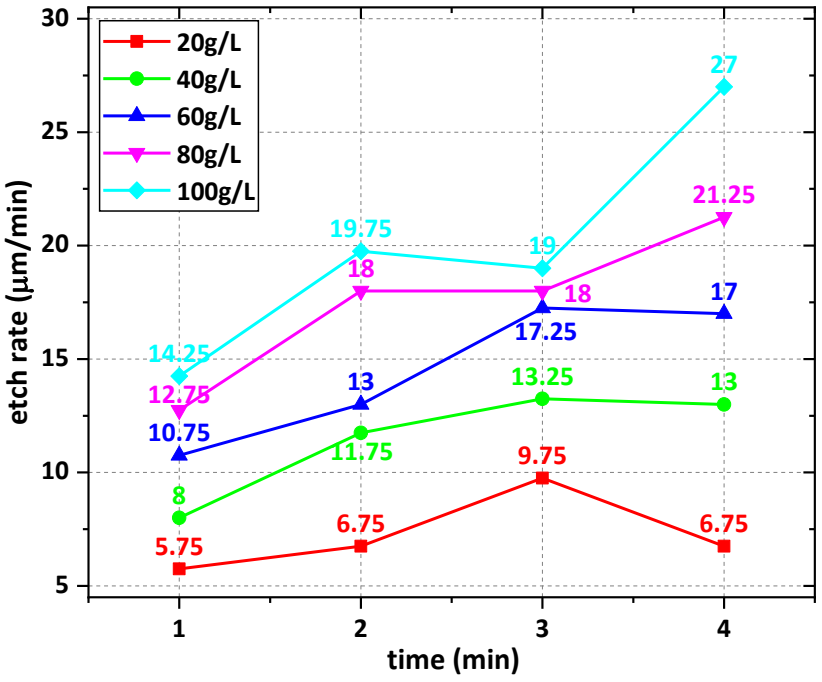

Figure 39: Etch rate of KOH etching of Al at 70°C

Based on this data, a thickness map (as shown in Figure 40) was developed to define the texturing process window. Considering the mechanical stability of the foil during the roll-to-roll (R2R) texturing and subsequent processing, the foil needs to be thicker than 95µm for the R2R tests and 70µm for the lab-scale cells. Also, visual observations were taken into account, such as the reflectance of the sample before defining the window. Based on this map, the following window was defined:

- *Temperature window = [60°C, 70°C]*

- *Time window = [2 min, 3 min]*
- *Concentration of etchant (molarity) = [80 g/L, 100 g/L] i.e. [1.42M, 1.78M]*

To validate the temperature window, AID measurements were done by selecting samples etched at various temperatures with a fixed concentration and time. The samples etched for 2 minutes at 100g/L were compared for 800 nm for 35, 50 and 70°C. Figure 41 shows the AID comparison. From this it is seen that the sample at 35°C has the highest intensity of specular reflection (highest specular peak), which shows poor scattering. This is followed by 50 and 70°C has the lowest specular peak. This is because of the dependence of specular and diffuse reflectance on roughness, as reported by [52], where lower RMS roughness result in higher specular peak and it is explained in section 4.3.3. For a better comparison, these values are normalized to understand the AID curve and is shown in Figure 42. Sample at 70°C scatters light into much higher angles as compared to 50 and 35°C. Hence, out of the three samples, the sample at 70°C showed the best scattering. This is explained by the dependence of diffuse reflection on the RMS roughness and correlation length, where a steeper sample (higher σ_{RMS}/Lc i.e. AR value) will scatter light into higher angles [18].

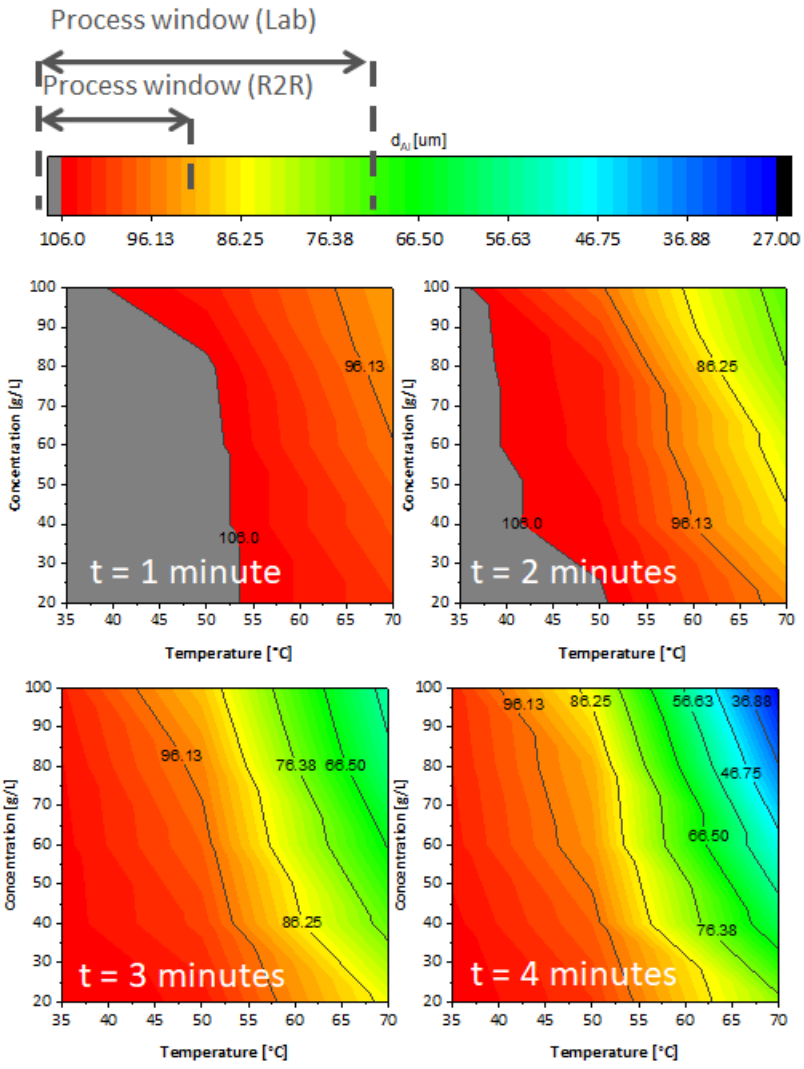

Figure 40: Texturing process map

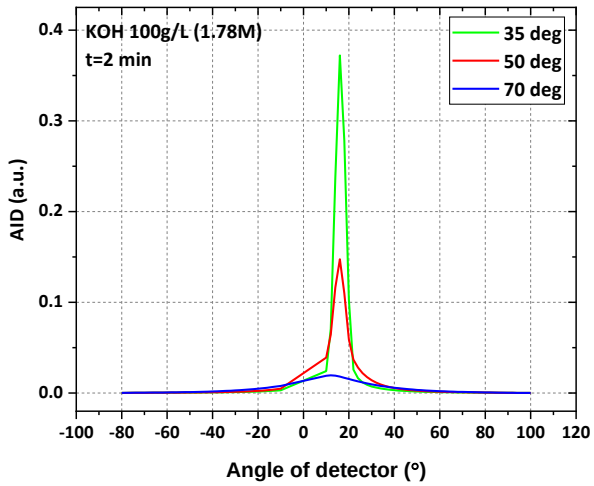

Figure 41: AID comparison between 35, 50 and 70°C at 800nm for t=2m

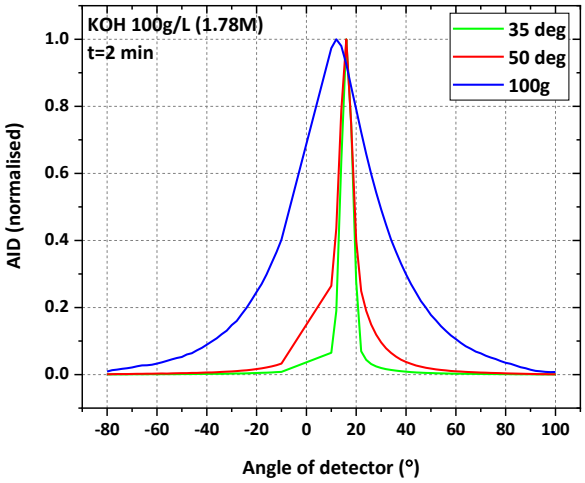

Figure 42: Normalised AID comparison between 35, 50 and 70°C at 800nm for t=2m

4.3.2 Etching at 70°C

A texturing map at 70°C is shown in Figure 43. For lower concentrations, the sample is visually highly reflective (shown by 'A' in the image). For higher concentrations, the sample is hazy (shown by 'B'). This is due to the lower reaction rate due to lower $(OH)^-$ concentrations at lower concentrations, as seen from the etch rate and thickness diagrams.

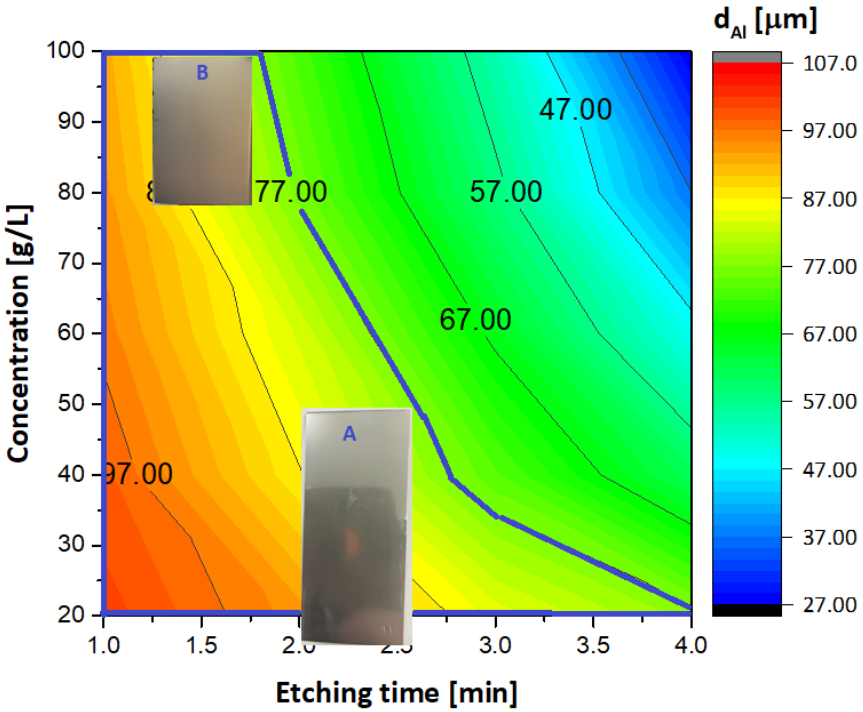

Figure 43: Texturing map- concentration vs time for 70°C

SEM images of samples etched at 70°C, 100 g/L for 1 and 2 minutes are shown in Figure 44. At 1 minute, the etching is non-uniform as the reaction rate is lower and some areas get etched more than the other. This could be because of localized penetration of the Al oxide and uneven etching resulting from other alloy elements (as induction period varies from element to element). Whereas at 2 minutes, craters are present throughout the surface of the foil. Etching time beyond 2 min is not considered for this temperature as it resulted in a very thin foil.

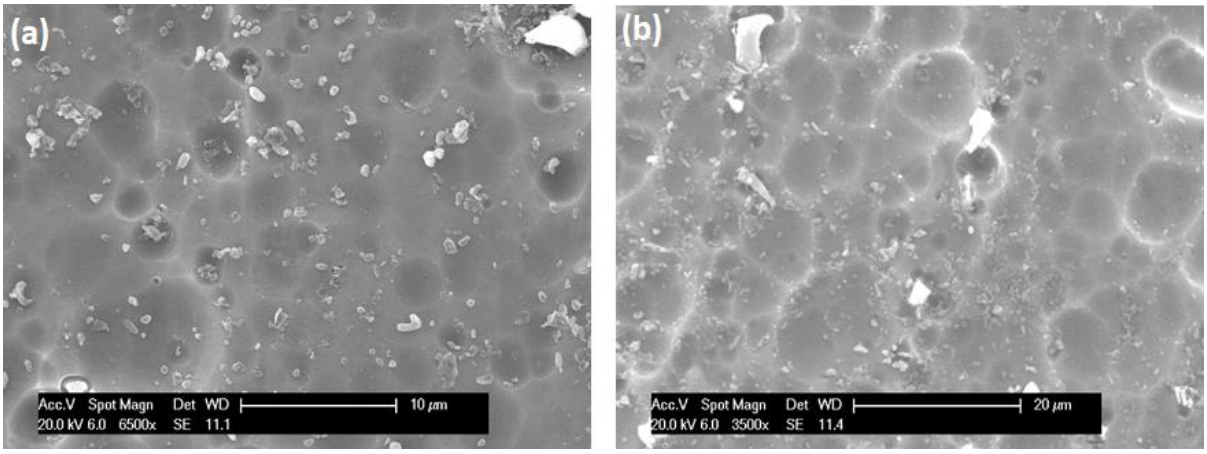

Figure 44: SEM images of KOH etching at 70°C, 100gL for (a) 1min (b) 2min

AFM measurements of selected samples- concentration series (60 g/L, 80 g/L and 100 g/L) of samples etched at 70°C for 2 minutes, are shown in Figure 45. The RMS roughness (σ_{RMS}), correlation length (Lc) and AR increases with increasing concentration. The sample at 100g/L has the highest AR close to 12% and Lc of 4 µm (targeted AR 14%, Lc 3-4 µm). Hence, this can be considered as the best lab sample at this point and will be referred as '***KOH70***'. The AFM images of the samples are shown in Figure 46. The calculations and values are given in Appendix II.

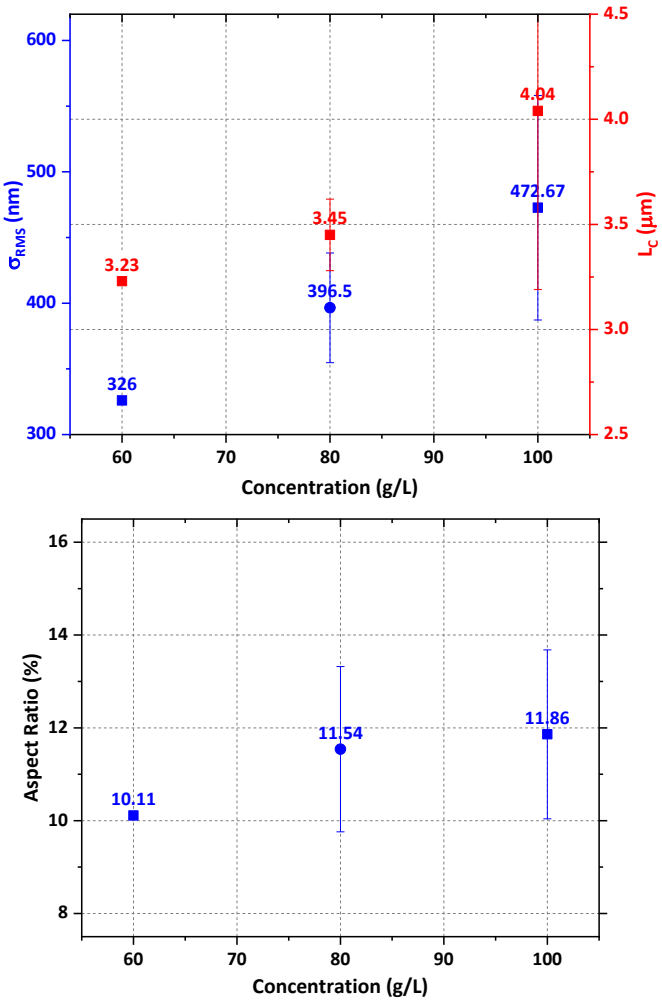

Figure 45: σRMS, Lc and AR of sample etched at 70°C, 2m- concentration series

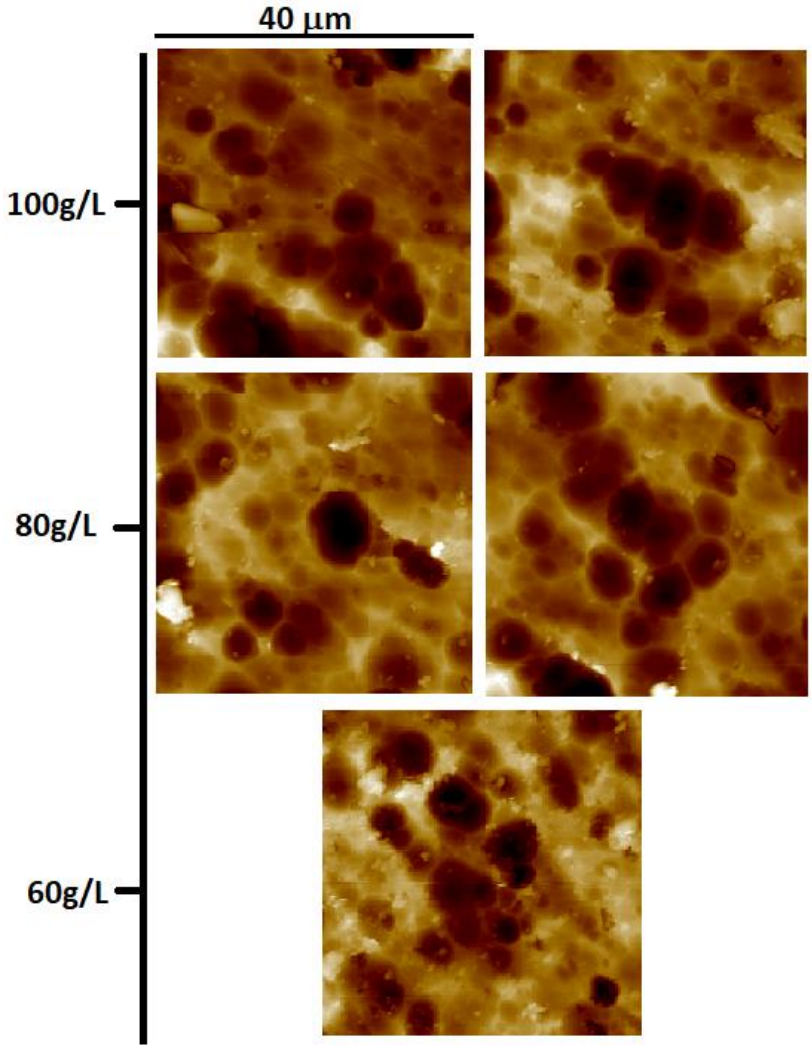

*Figure 46: 40µm*40µm AFM images of samples etched in KOH at 70°C, 2m- concentration series*

4.3.3 Comparison between factory baseline and KOH70:

The surface features of factory baseline and KOH70 are:

Parameters	Factory baseline	KOH70
RMS roughness (σ_{RMS}) (nm)	28.4	472.67
Autocorrelation length (L_C) (µm)	0.497	4.04
Aspect Ratio (σ_{RMS}/L_C) (%)	5.7	11.86
Slope (θ_m)	12.11°	16.72°

Table 5: Surface morphology characterization comparison between factory baseline and KOH70

Compared to the factory baseline, the sample KOH70 displays much larger surface feature values that are closer to the targeted values.

Reflectance comparison between factory baseline and KOH70 is shown in Figure 47. The following observations can be made:

- KOH70 has much higher diffuse reflectance and reflective haze compared to the factory baseline. The diffuse reflectance is a function of the surface parameters as reported by [52] can be written as:

$$\int_0^{\Delta\theta} r_d(\theta)d\theta = R_0 \frac{2^5\pi^4}{m^2}\left(\frac{\sigma_{RMS}}{\lambda}\right)^4 (\Delta\theta)^2 \quad (4.3)$$

where m is the root mean square slope:

$$L_c = \sqrt{2}\sigma_{RMS}/m$$

From eqn. (4.3), the diffuse reflectance for a wavelength is directly proportional to the roughness and correlation length and inversely proportional to the wavelength. Thus, very low values of roughness and correlation lengths result in lower diffuse reflectance values, i.e. poor scattering. For the same set of roughness and correlation lengths, as the wavelength increases, the diffuse reflectance value reduces. For the case of the baseline, this value steadily reduces as wavelength increases since the feature sizes are significantly smaller than the wavelengths.

Whereas, larger diffuse reflectance of KOH70 is observed at higher wavelengths, as opposed to the factory baseline which implies an improvement in the surface features which is in line with the observations made by [52] [18]. The parameters can be summed up as:

Parameters	***Factory baseline***	***KOH70***
Average total reflectance	*86.7 %*	*78.46 %*
Average diffuse reflectance	*25.8 %*	*74.18 %*
Average specular reflectance (total-diffuse)	*60.8 %*	*4.28 %*
Average haze (diffuse/total)	*29.98 %*	*94.54 %*

Table 6: Reflectance values of factory baseline and KOH70

- The factory baseline shows a high specular peak compared to KOH70 (shown in Figure 48). This is related to the roughness of the sample based on [52]:

$$R_s = R_0 \exp\left[(-4\pi\sigma_{RMS})^2/\lambda^2\right] \quad (4.4)$$

where R_0 is the reflectance of a perfectly smooth Al. Higher the roughness, lower will be the specular peak for a fixed wavelength [48].

- For better clarity, the normalised AID curves of factory baseline and KOH70 is shown in Figure 49. KOH70 sample scatters light into higher angles as compared to the factory baseline. The broader AID curve is due to the higher aspect ratio (and thus a higher slope- AR and slope are indicators of how steep the feature is) of KOH70 compared to the factory baseline [18]. The AID plots are shown for 800 nm.

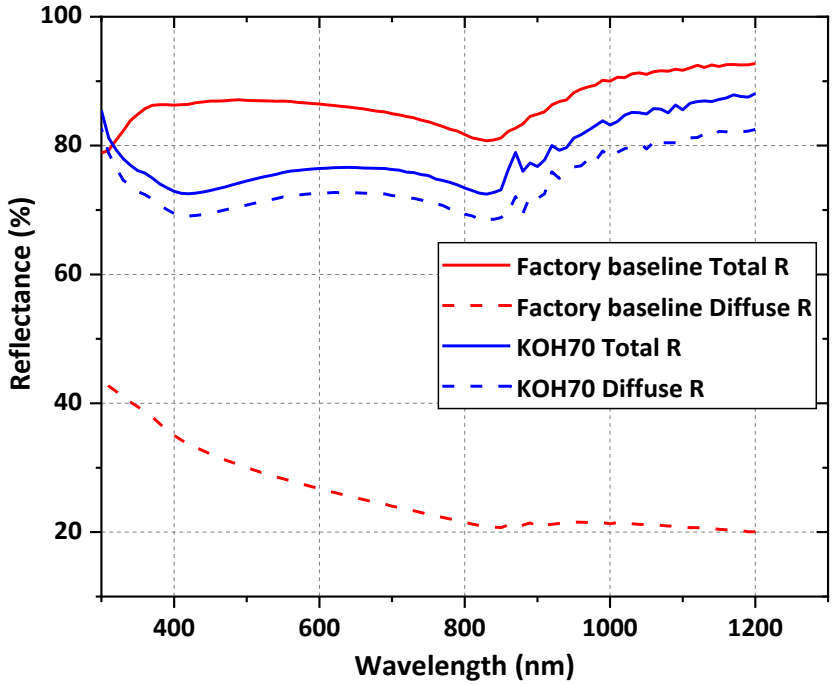

Figure 47: Total and diffuse reflectance comparison between factory baseline and KOH70

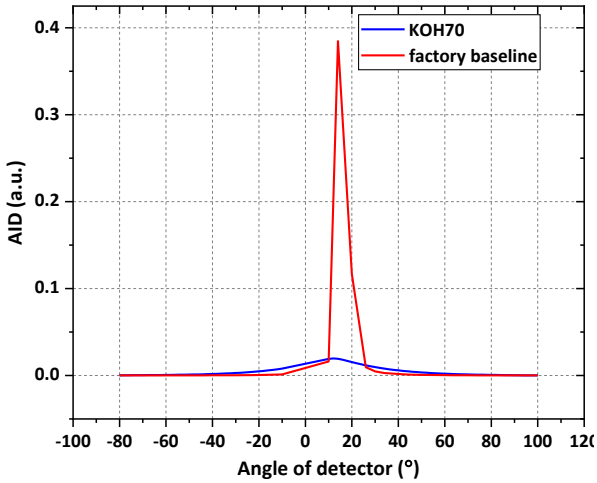

Figure 48: Angular intensity distribution comparison between factory baseline and KOH70 at 800 nm

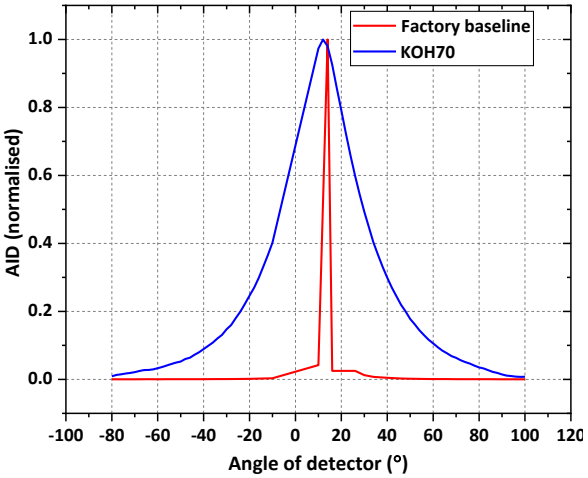

Figure 49: Normalised Angular intensity distribution comparison between factory baseline and KOH70 at 800 nm

To analyse the improvement of KOH70 over the baseline, an AZO/p-i-n nc-Si stack was deposited onto the etched Al foils. The cross-sectional SEM images are displayed in Figure 50. The layers deposited onto the factory baseline (as shown in (a)), did not result in good quality nc-Si:H layers. Moreover, after the FTO is deposited, which is naturally pyramidally textured, the subsequent layers did not adapt the superimposed texturing pattern (pattern of Al + pattern of FTO), since the baseline texturing features are very small. Whereas, the layers deposited onto KOH70 followed the texturing pattern (as shown in (b)) and resulted in dense materials with high quality.

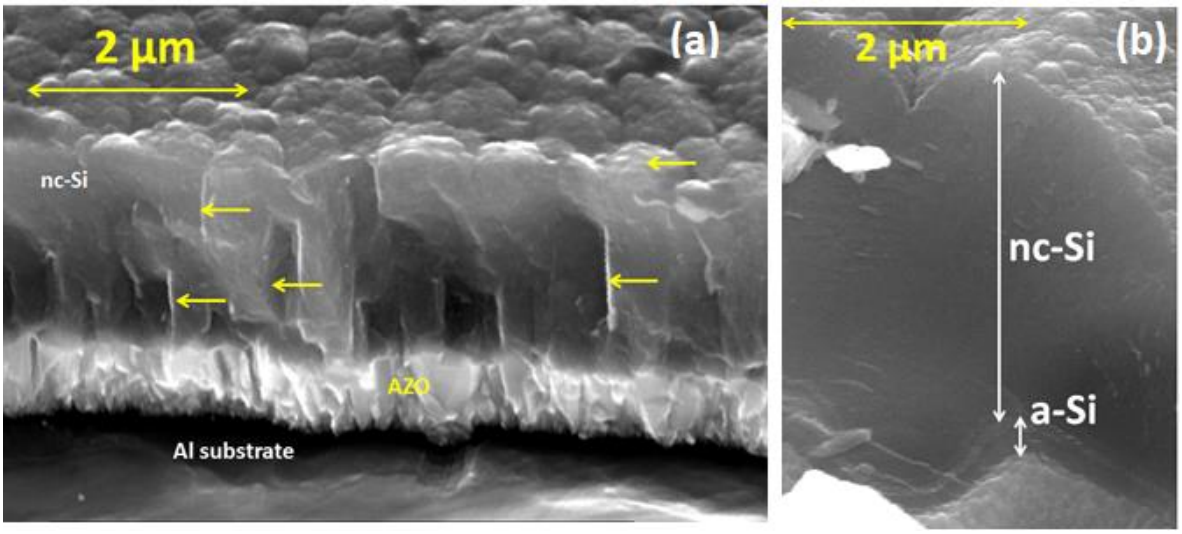

Figure 50: TCO/p-i-n layers deposited onto (a) factory baseline texturing (b) KOH70 texturing

Figure 51 shows an image of a cell deposited on KOH70 as the temporary substrate. The cell is processed and encapsulated using the HyET production process. It can be seen that the morphology of the Al substrate is transferred to all the cells and is preserved after the final encapsulation process. This confirms that the concept of MST can be successfully applied on Al foils.

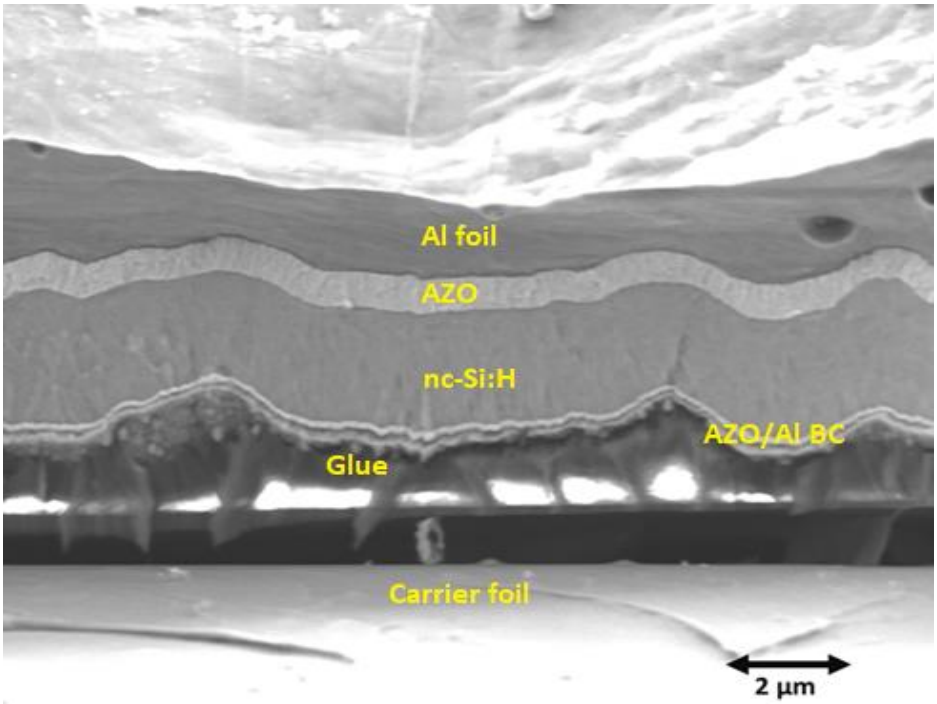

Figure 51: Cell deposited on KOH70

4.3.4 Etching at 60°C

The texturing map shown in Figure 40 showed possibility of good texturing at temperatures between 50 and 70°C. Hence, texturing was also investigated at 60°C. Since higher concentrations, i.e. 80 g/L and 100 g/L showed best results with 70°C, these concentrations were selected to do a thickness series with 60°C. The thickness series for 60°C was done for 2 to 4 minutes, based on the induction period and thickness data at 50 and 70°C. Figure 52 shows a comparison between 60 and 70°C for 80 and 100

g/L. As expected, 60°C shows a considerably lower etch rate compared to 70°C. Higher concentrations resulted in higher etch rates, i.e. 100 g/L at 60°C showed higher etching compared to 80 g/L at the same temperature.

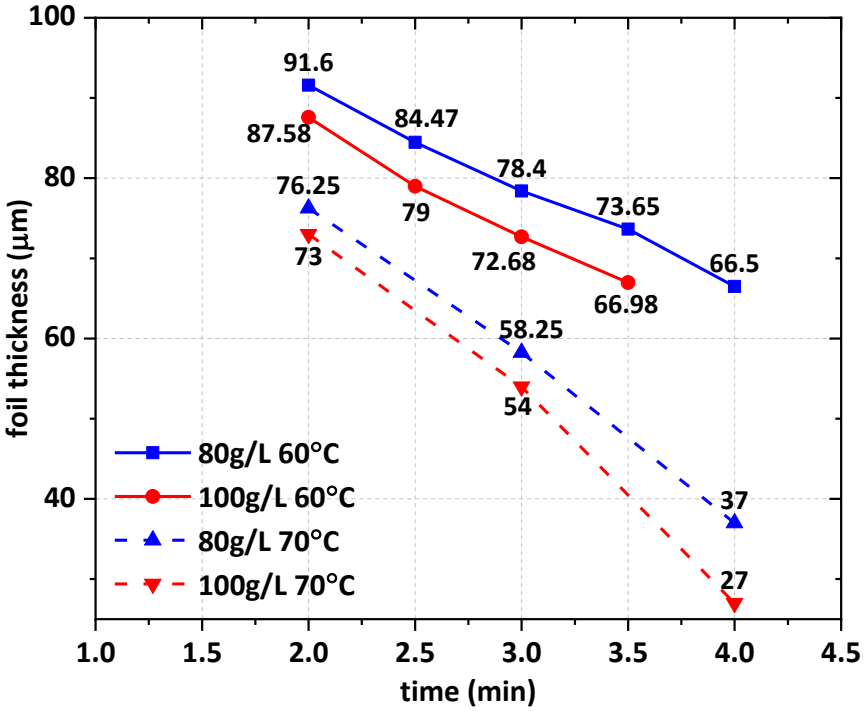

Figure 52: Thickness series comparison between 60 and 70°C for 80 and 100 g/L

Figure 53 shows the SEM and AFM images of samples etched at 60°C, 80 g/L for 2, 2.5 and 3 minutes. The RMS roughness, autocorrelation length and the aspect ratios of these samples are shown in Figure 54. The roughness increases with increasing time, whereas Lc decreases with time. This could be because of formation of new and small craters as time increases which have a lower value of L_C and can influence the final value. If so, the roughness values should decrease as well since new and small craters are formed but that is not the case. Hence, no definitive conclusions can be made from this trend. The AR increases with increasing time and approaches the targeted value of 14% at 3 minutes.

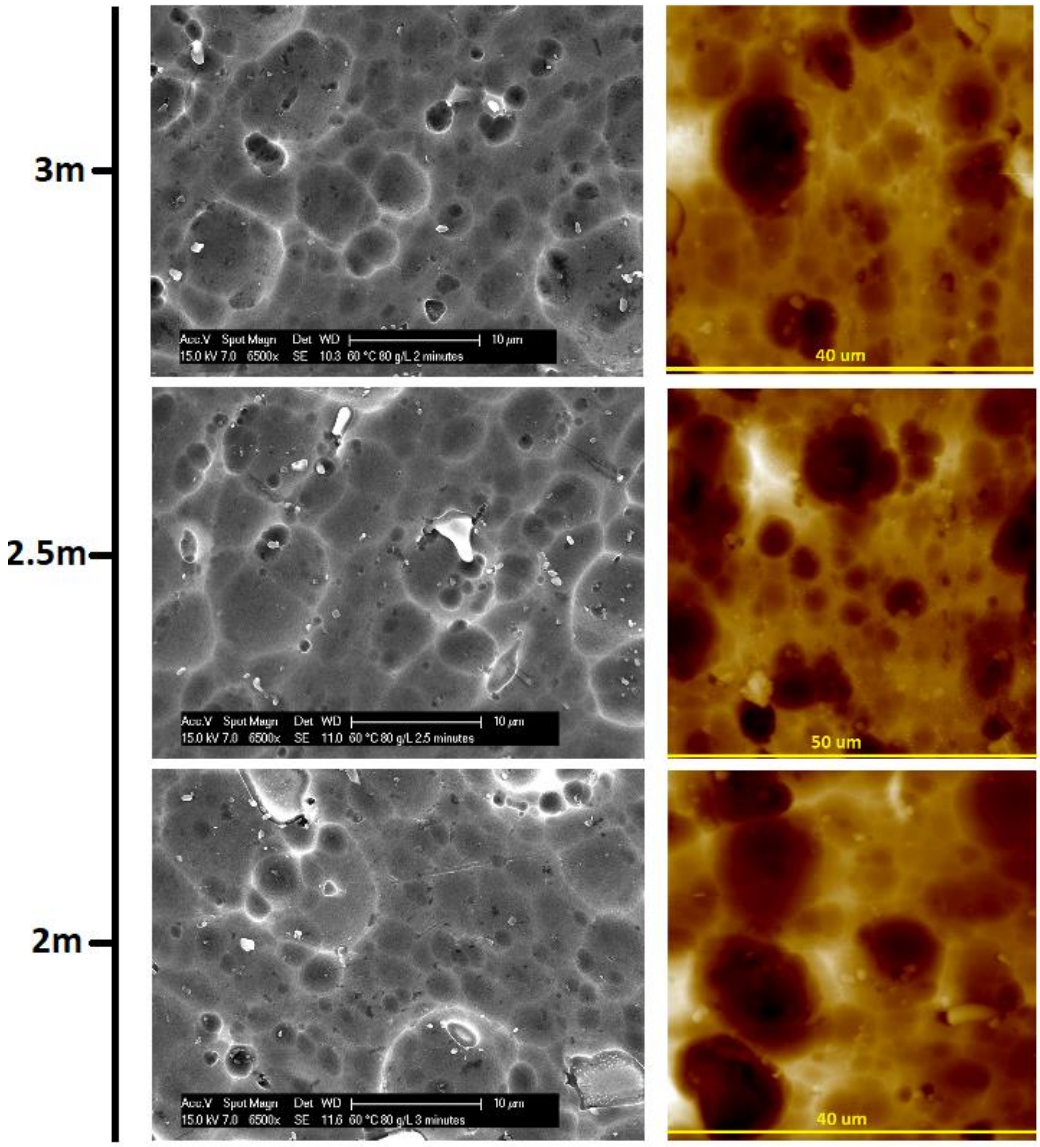

Figure 53: SEM and AFM images of KOH etched samples at 60°C, 80 g/L- time series

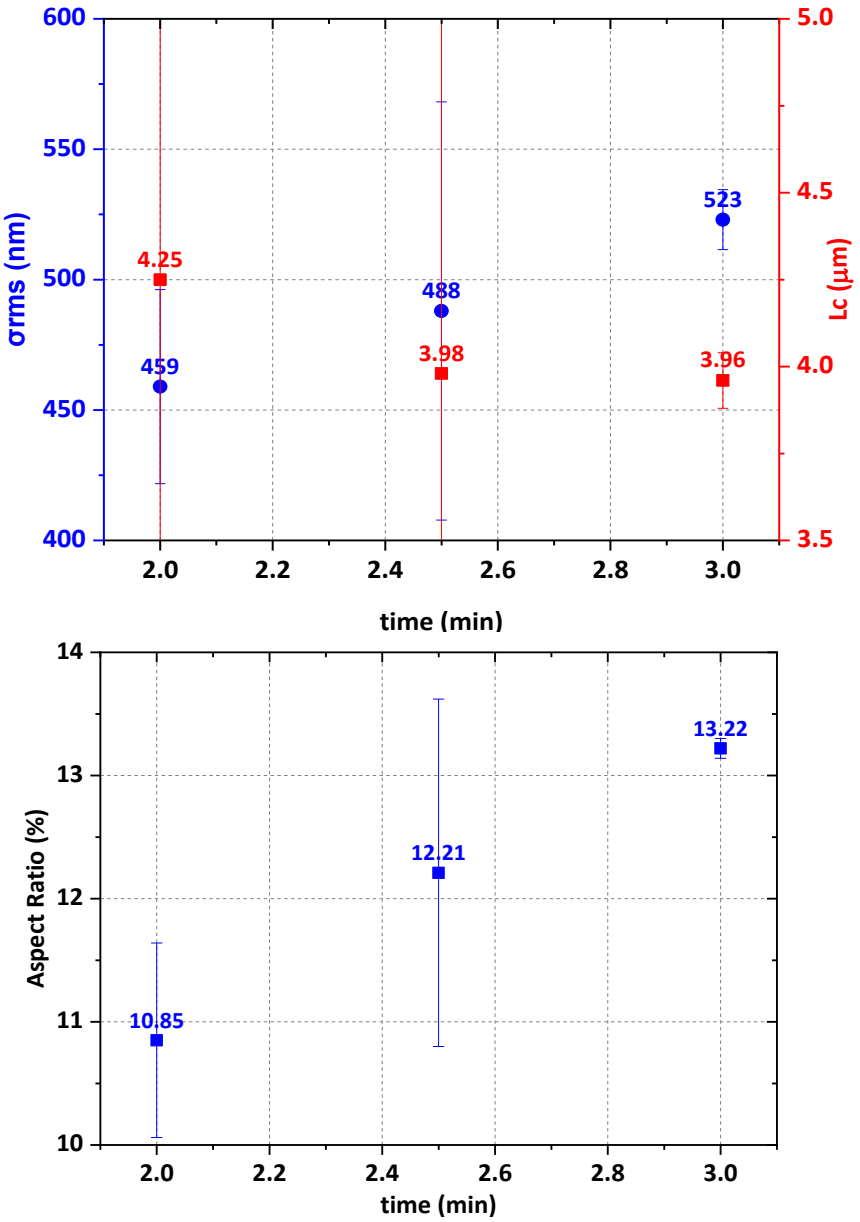

Figure 54: σ_{RMS}, Lc and AR of sample etched at 60°C, 80 g/L- time series

Similarly, the SEM and AFM images of samples etched at 100 g/L for 2, 2.5 and 3 minutes are shown in Figure 55 and its corresponding roughness, autocorrelation length and aspect ratio values in Figure 56. Unlike the data set at 80 g/L, all the 3 parameters increase with increasing etching time. The sample at 3 minutes shows an AR of 14.3% and Lc of 4.6 µm, which is very close to the targeted value.

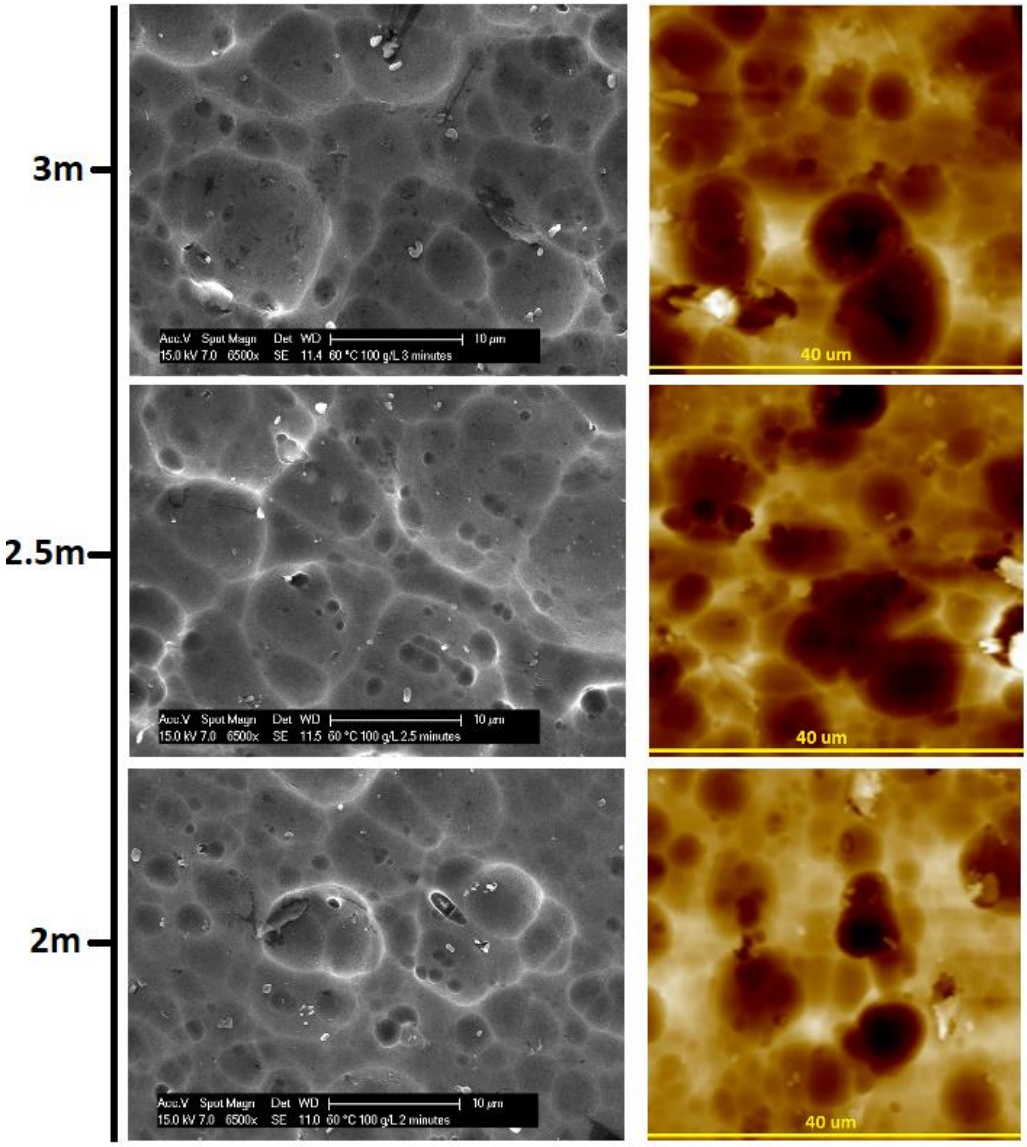

Figure 55: SEM and AFM images of KOH etched samples at 60°C, 100 g/L- time series

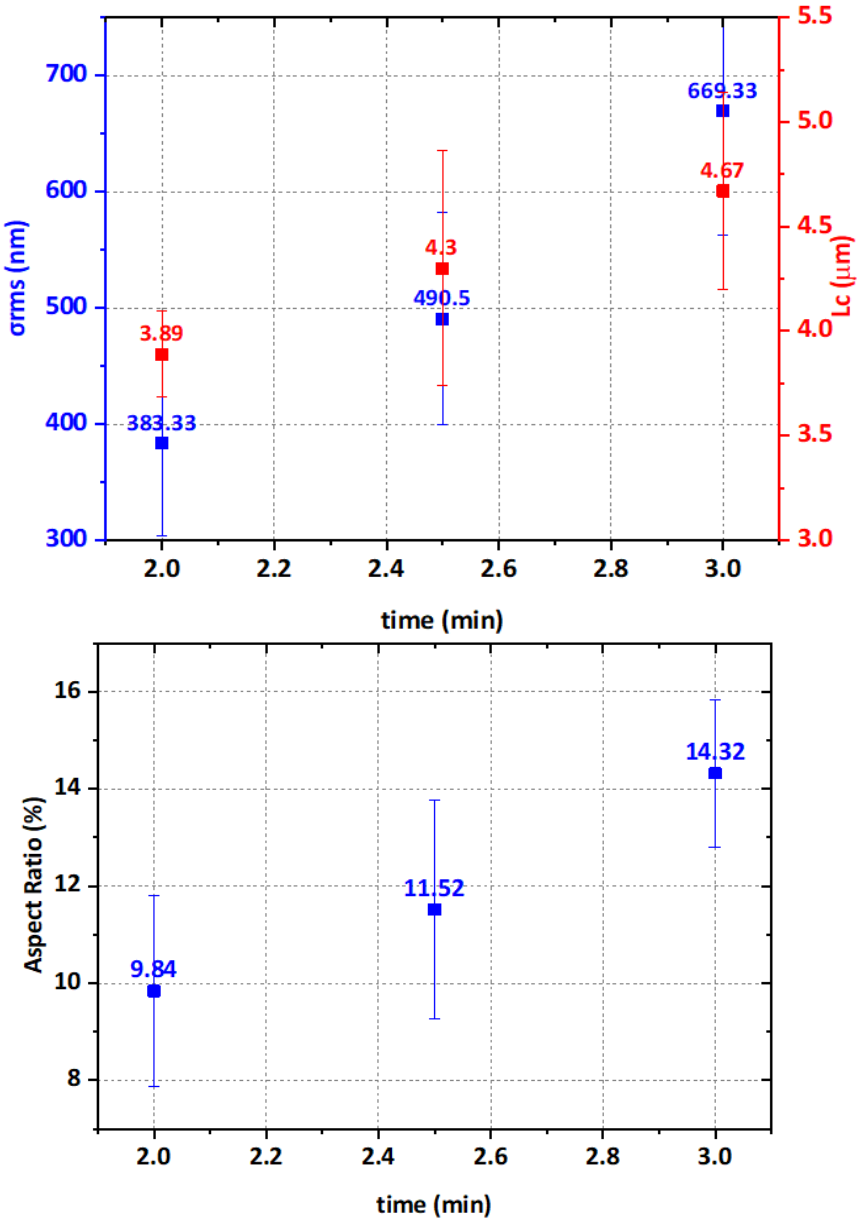

Figure 56: σ_{RMS}, Lc and AR of sample etched at 60°C, 100 g/L- time series

Figure 57 and Figure 58 shows the absolute and normalised AID measurements of samples etched at 60°C, 100 g/L for 2, 2.5 and 3 minutes at 800 nm. The sample etched for the longest time has the lowest specular peak and the sample etched for the shortest time has the highest specular peak. This is related to the RMS roughness values as mentioned in section 4.3.3. Higher the roughness, lower is the specular intensity. The normalised curve is broader for samples at 2.5 minutes and 3 minutes compared to the sample etched at 2 minutes. This is due to its higher AR values, i.e., higher AR results in scattering of light into larger angles. However, from the data it is difficult to make a comparison between 2.5 and 3 minutes. A similar trend can be expected for the samples etched with 80 g/L of KOH as well.

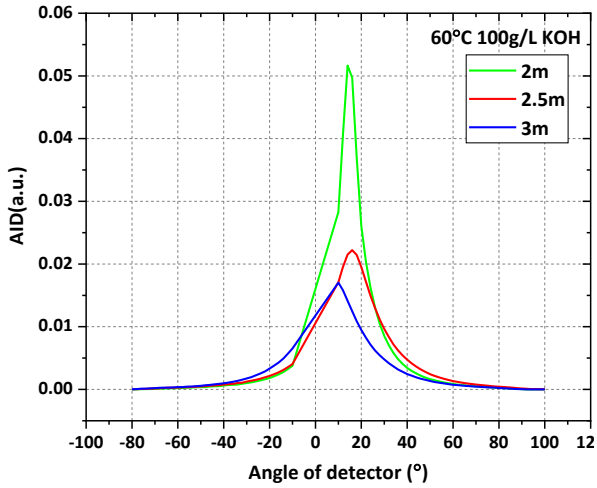

Figure 57: Angular intensity distribution of KOH etched samples at 60°C, 100 g/L at 800 nm- time series

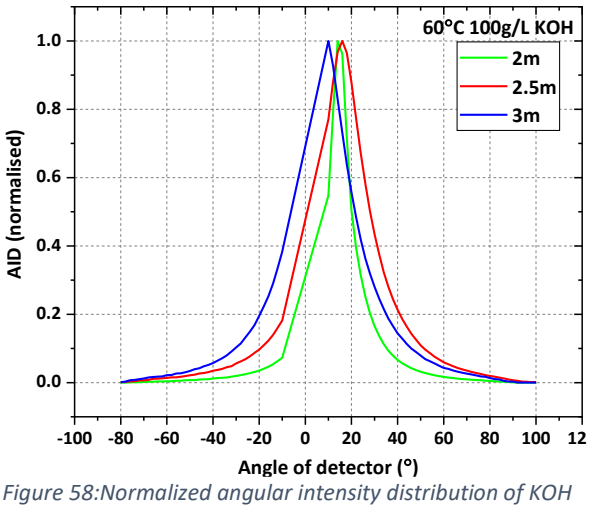

Figure 58:Normalized angular intensity distribution of KOH etched samples at 60°C, 100 g/L at 800 nm- time series

To compare the samples etched with 100 g/L and 80 g/L, samples etched at 3m are compared. Figure 59 and Figure 60 shows the absolute and normalised AID measurements. The sample at 100 g/L has a lower specular component compared to the sample at 80 g/L since the sample at 100 g/L has a higher RMS roughness than the sample at 80 g/L (eqn. 4.4). The normalised curve for sample at 100 g/L is slightly broader as well, due to its higher AR compared to the sample at 80 g/L. Figure 61 and Figure 62 shows the reflectance and haze measurement of these two samples. The 100 g/L sample has a higher diffuse and lower specular reflection, i.e. a higher haze compared to the sample at 80 g/L due to its superior surface parameter values. From the AID and reflectance measurements, it can be said that the sample at 100 g/L scatters more compared to the one at 80 g/L.

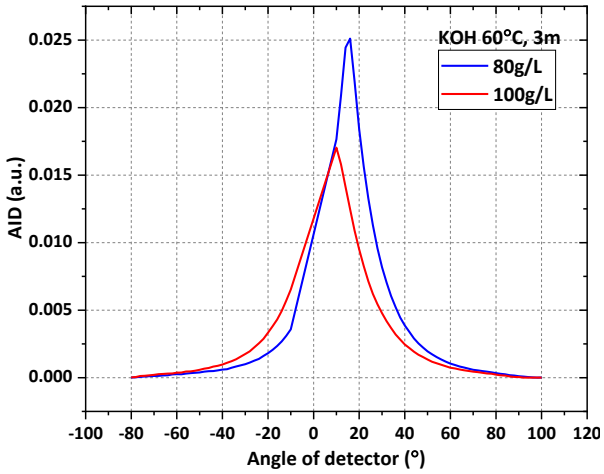

Figure 59: Angular intensity distribution comparison of KOH etched samples at 60°C for 3m, 80 and 100 g/L at 800 nm

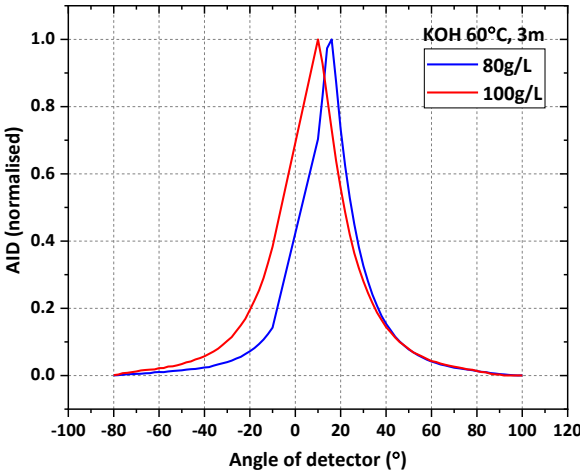

Figure 60: Normalised angular intensity distribution comparison of KOH etched samples at 60°C for 3m, 80 and 100 g/L at 800 nm

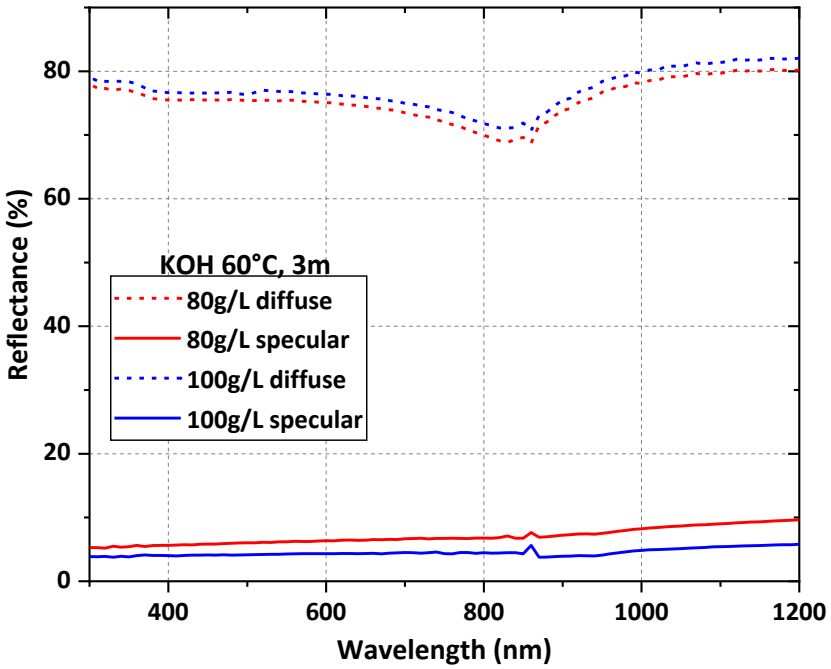

Figure 61: Diffuse and specular reflection comparison between 80 and 100 g/L, KOH at 60°C, 3m

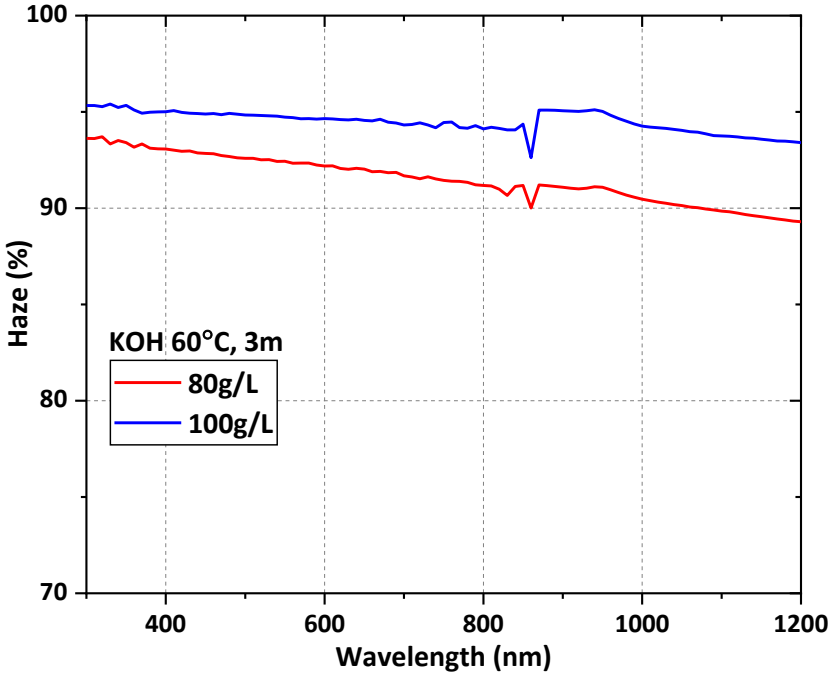

Figure 62: Reflection haze comparison between 80 and 100 g/L, KOH at 60°C, 3m

Since the sample at 60°C, 100 g/L etched for 3 minutes has the best surface features and scattering properties, it will also be considered as one of the best lab samples and will be referred as '***KOH60***'.

4.3.5 Comparison between factory baseline and KOH60:

The surface features of factory baseline and KOH60 are:

Parameters	Factory baseline	KOH60
RMS roughness (σ_{RMS}) (nm)	28.4	669
Autocorrelation length (L_C) (μm)	0.497	4.67
Aspect Ratio (σ_{RMS}/L_C) (%)	5.7	14.32
Slope (θ_m)	12.11°	18.56°

Table 7: Surface morphology characterization comparison between factory baseline, KOH70 and KOH60

KOH60 has larger surface feature values compared to the factory baseline and are close to the targeted values. Figure 63 and Figure 64 show the absolute and normalised AID comparison between KOH60 and factory baseline. KOH60 has a lower specular intensity peak compared to the factory baseline due to its higher RMS roughness. It also scatters light into higher angles due to its higher AR (and higher slope).

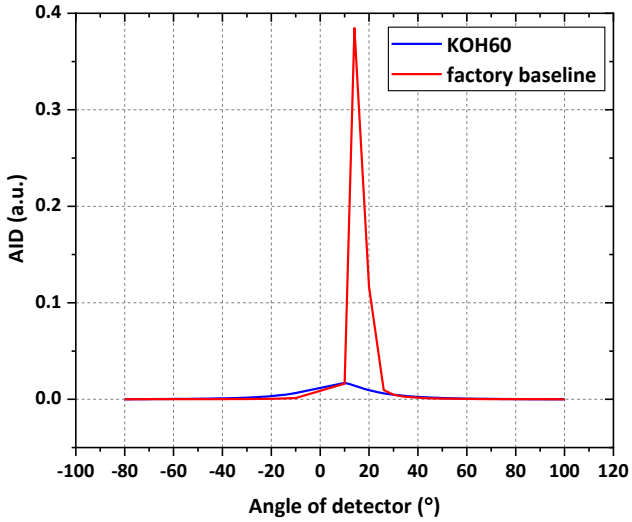

Figure 63: Angular intensity distribution comparison between factory baseline and KOH60 at 800 nm

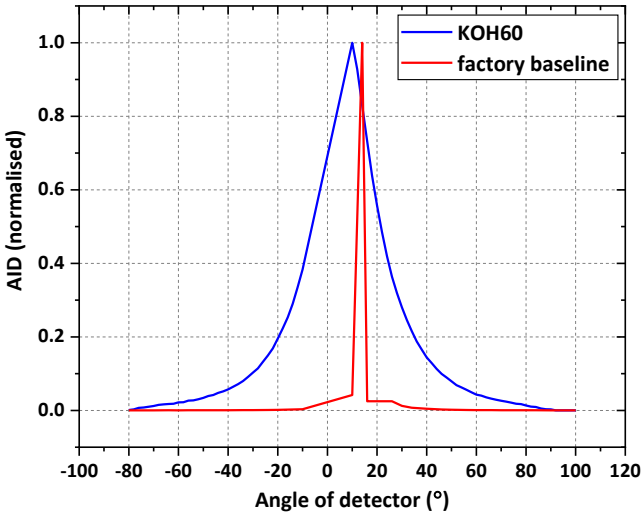

Figure 64: Normalised angular intensity distribution comparison between factory baseline and KOH60 at 800 nm

Figure 65 and Figure 66 shows the diffuse, specular and reflectance haze comparison between factory baseline and KOH60. Since KOH60 has higher RMS roughness compared to the baseline, it has significantly lower specular reflection and a high diffuse reflection. Thus, a higher haze. A higher haze also corresponds to a broader AID curve. Compared to the factory baseline KOH60 displays significant improvement in scattering at 800 nm. These observations are in line with [52] and [18]. The reflection values are listed in Table 8.

Parameters	Factory baseline	KOH60
Average total reflectance	86.7 %	81.56%
Average diffuse reflectance	25.8 %	77.09%
Average specular reflectance (total-diffuse)	60.8 %	4.49%
Average haze (diffuse/total)	29.98 %	94.49%

Table 8: Reflectance values of factory baseline and KOH60

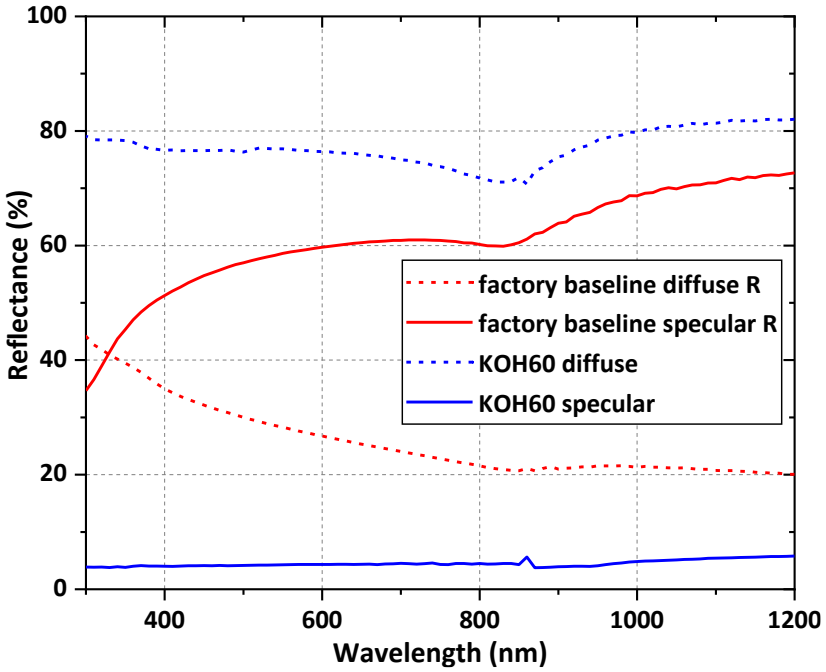

Figure 65: Diffuse and specular reflection comparison between factory baseline and KOH60

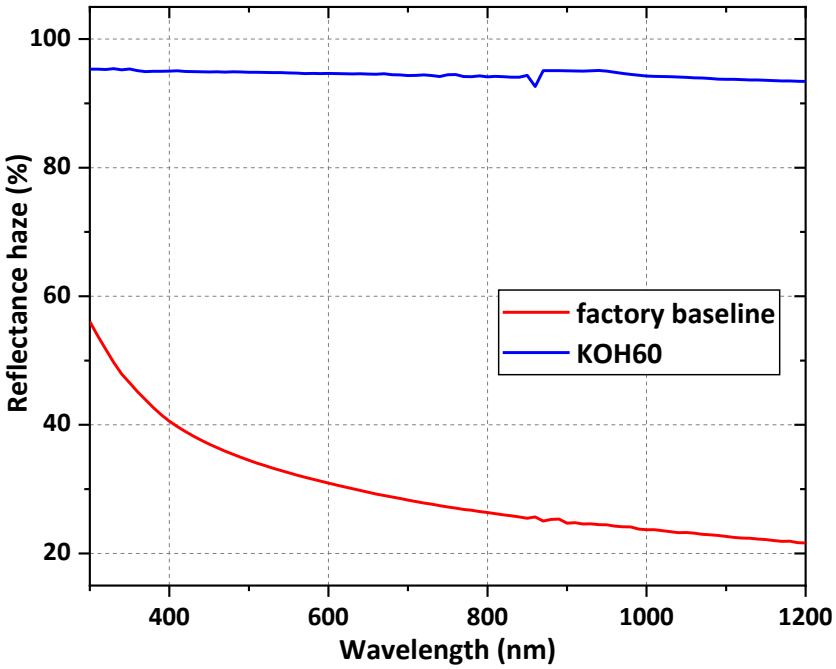

Figure 66: Reflection haze comparison between factory baseline and KOH60

4.4 NaOH etching

Etching Al with NaOH also resulted in crater like structures. Since optimum feature sizes were obtained with KOH, the NaOH recipe was also calculated using the same molarity as KOH:

Molar mass of KOH = 56.1056 g/mol
Molar mass of NaOH = 39.997 g/mol

80 g of KOH in 1L of water:

Number of mols: 80 g/56.1056gmol^{-1} = 1.425 mol/L = 1.425 M
Equivalent grams of NaOH needed = 1.425M x 39.997 gmol^{-1} = 57.03 g/L

100 g of KOH in 1L of water:
Number of mols: 100 g/56.1056gmol^{-1} = 1.78 mol/L = 1.78 M
Equivalent grams of NaOH needed = 1.78M x 39.997 gmol^{-1} = 71.288 g/L

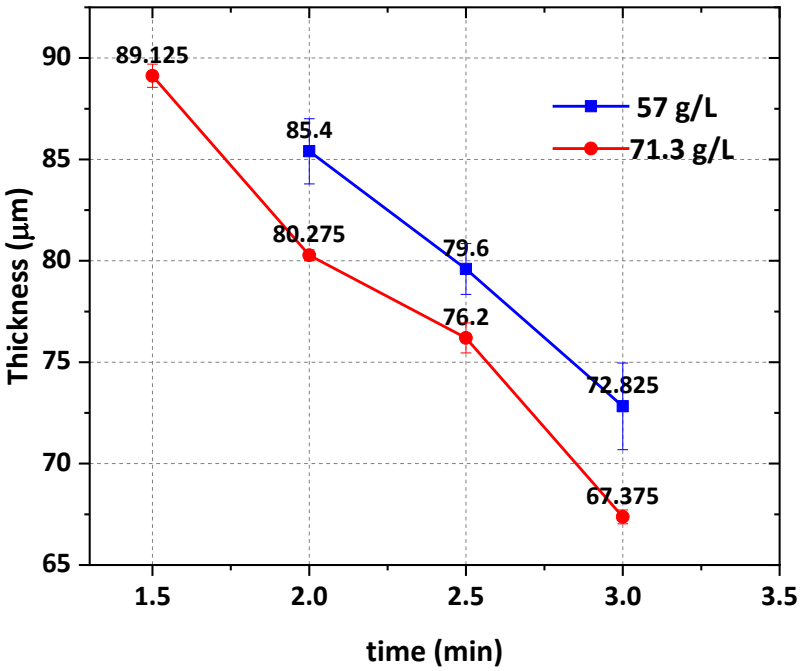

Figure 67: Thickness measurement of Al foil etched with NaOH at 60°C

Since targeted ARs were obtained with KOH at 60°C, the etching temperature is fixed at 60°C for NaOH as well and 57 and 71.3 g/L as the concentration corresponding to 80 and 100 g/L (1.42 and 1.78M) of KOH respectively. Also, using 70°C for NaOH etching resulted in very thin foils.

The thickness measurement of NaOH etching is shown in Figure 67. Comparing this with the thickness series of KOH texturing, NaOH etching resulted in a lower thickness at the same conditions. For example, at 1.42M (80 g/L of KOH and 57 g/L of NaOH), at 60°C etched for 2 minutes, resulted in 91.6 µm and 85.4 µm for KOH and NaOH, respectively. Similar trend was observed for other time intervals as well. Thus, NaOH is more reactive with Al than KOH which was also reported by [55].

4.4.1 Etching with 1.42M (57 g/L) NaOH solution

Figure 68 shows the SEM and AFM images of samples etched with 57 g/L NaOH at 60°C for 2, 2.5 and 3 minutes. The sizes of the craters seem to be increasing with increasing etching time. Figure 69 shows its corresponding RMS roughness, correlation length Lc and aspect ratio AR. All three parameters follow the same trend- from 2 to 2.5 minutes, the values are increasing, whereas from 2.5 to 3 minutes, the values are decreasing. Like KOH etching, this can be explained by the formation of small new craters within existing craters which can lower the values mathematically. From these set of values, the sample etched at 2.5 minutes (σ_{RMS} 594nm, Lc 4.36mm and AR of 13.58%) is close to the targeted values.

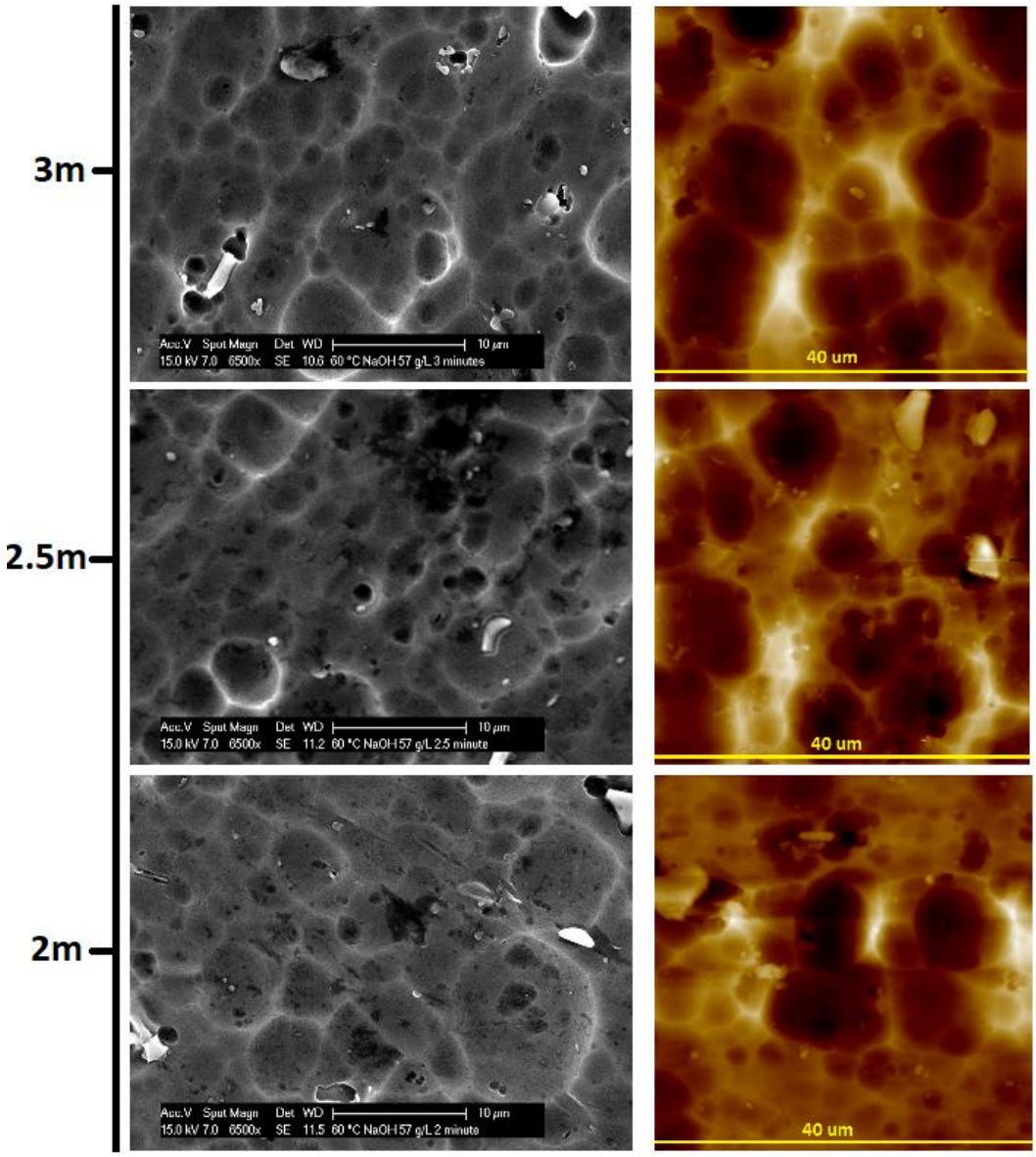

Figure 68: SEM and AFM images of NaOH etched samples at 60°C, 57 g/L- time series

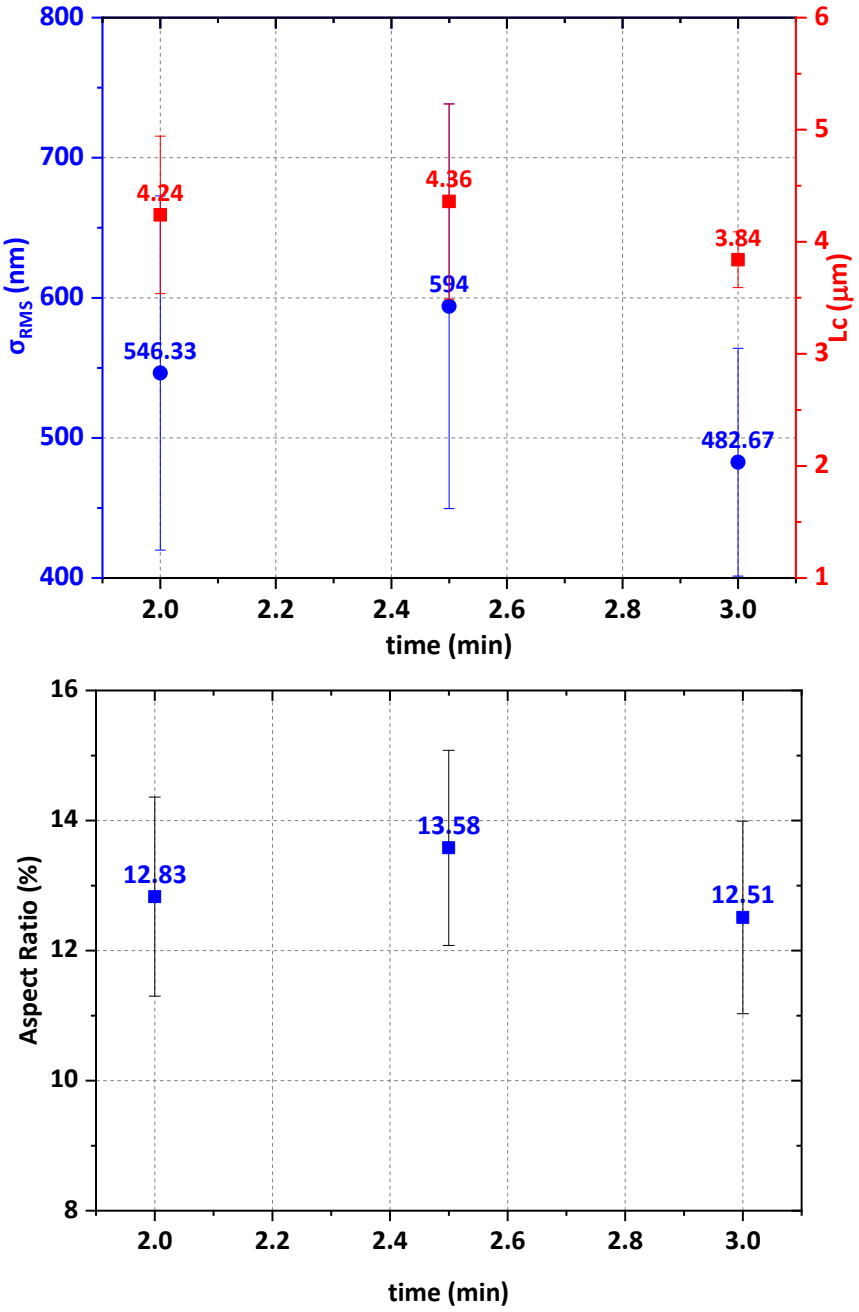

Figure 69: σ_{RMS}, Lc and AR of sample etched with NaOH at 60°C, 57 g/L- time series

Figure 70 and Figure 71 shows the absolute and normalised AID measurements of these samples for 2 and 2.5 minutes (sample at 3 minutes are not shown since the features of samples at 2 and 2.5 minutes are larger). The sample at 2.5 minutes has a lower specular intensity peak as compared to the one at 2 minutes. This is explained by the higher roughness of the sample at 2.5 minutes. Also, this sample exhibits a broader AID curve which can be explained by its higher AR. The sample at 2.5 minutes thus has superior surface morphology as well as scattering properties. Figure 72 and Figure 73 shows the reflectance and haze measurement of these two samples. The sample at 2.5 minutes have a higher diffuse and lower specular reflection, i.e. a higher haze, especially at higher wavelengths compared to the sample at 2 minutes due to its superior surface parameter values. From the AID and reflectance measurements, it can be said that the sample at 2.5 minutes scatters more compared to the one at 2 minutes.

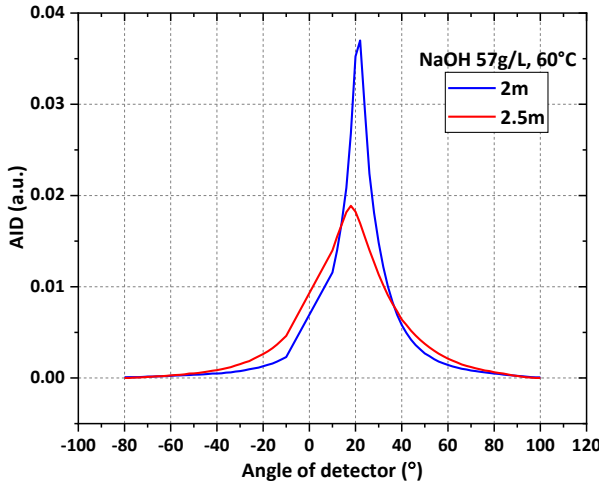

Figure 70: Angular intensity distribution of NaOH etched samples at 60°C, 5 7g/L at 800 nm- time series

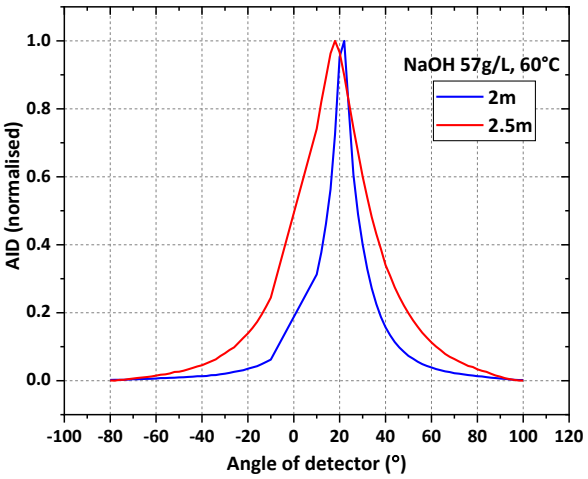

Figure 71: Normalised angular intensity distribution of NaOH etched samples at 60°C, 57 g/L at 800 nm- time series

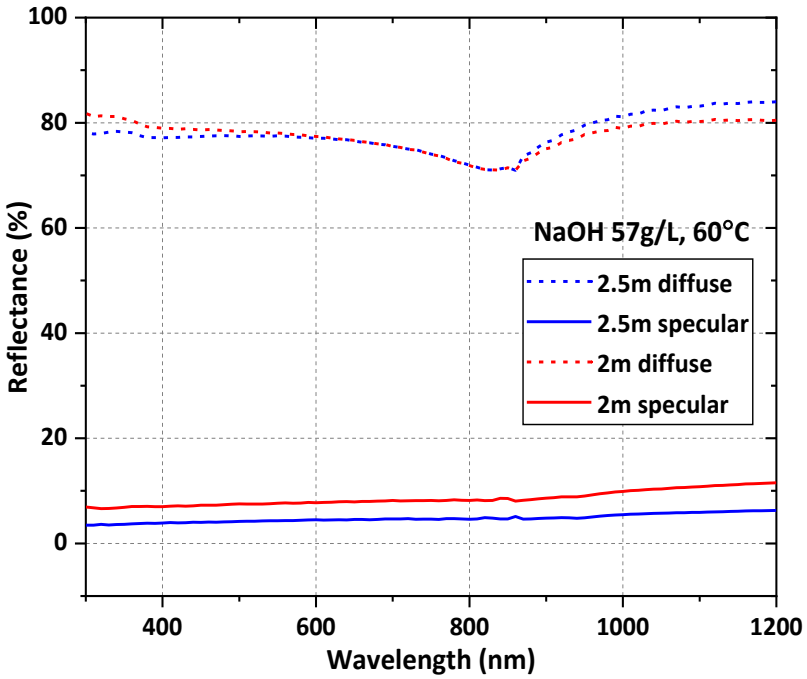

Figure 72: Diffuse and specular reflection comparison between NaOH etched sample with 57 g/L at 60°C for 2 and 2.5m

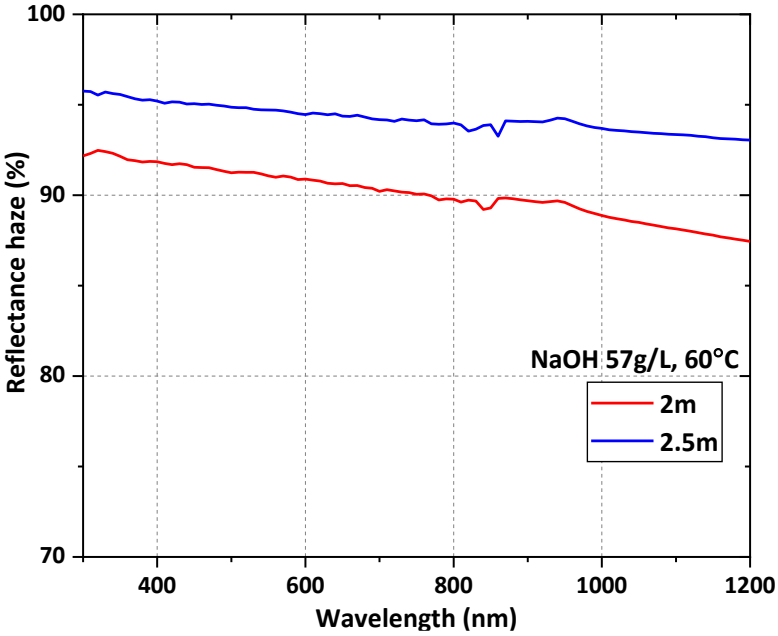

Figure 73: Reflection haze comparison between NaOH etched sample with 57 g/L at 60°C for 2 and 2.5m

4.4.2 Etching with 1.78M (71 g/L) NaOH solution

Figure 74 shows the SEM and AFM images of samples etched with 71 g/L of NaOH at 60°C for 2, 2.5 and 3 minutes. Like the previous results, from visual observation, the craters seem to be increasing in size as the etching time increases. Figure 75 shows the RMS roughness, correlation length and aspect ratio values of these samples. The roughness and the AR follow a similar trend as that of 57 g/L, i.e. increases till 2.5 minutes after which it decreases. Whereas, Lc is slightly decreasing at 2.5 minutes after which it slightly increases. The sample at 2.5 minutes has parameters close to the targeted value.

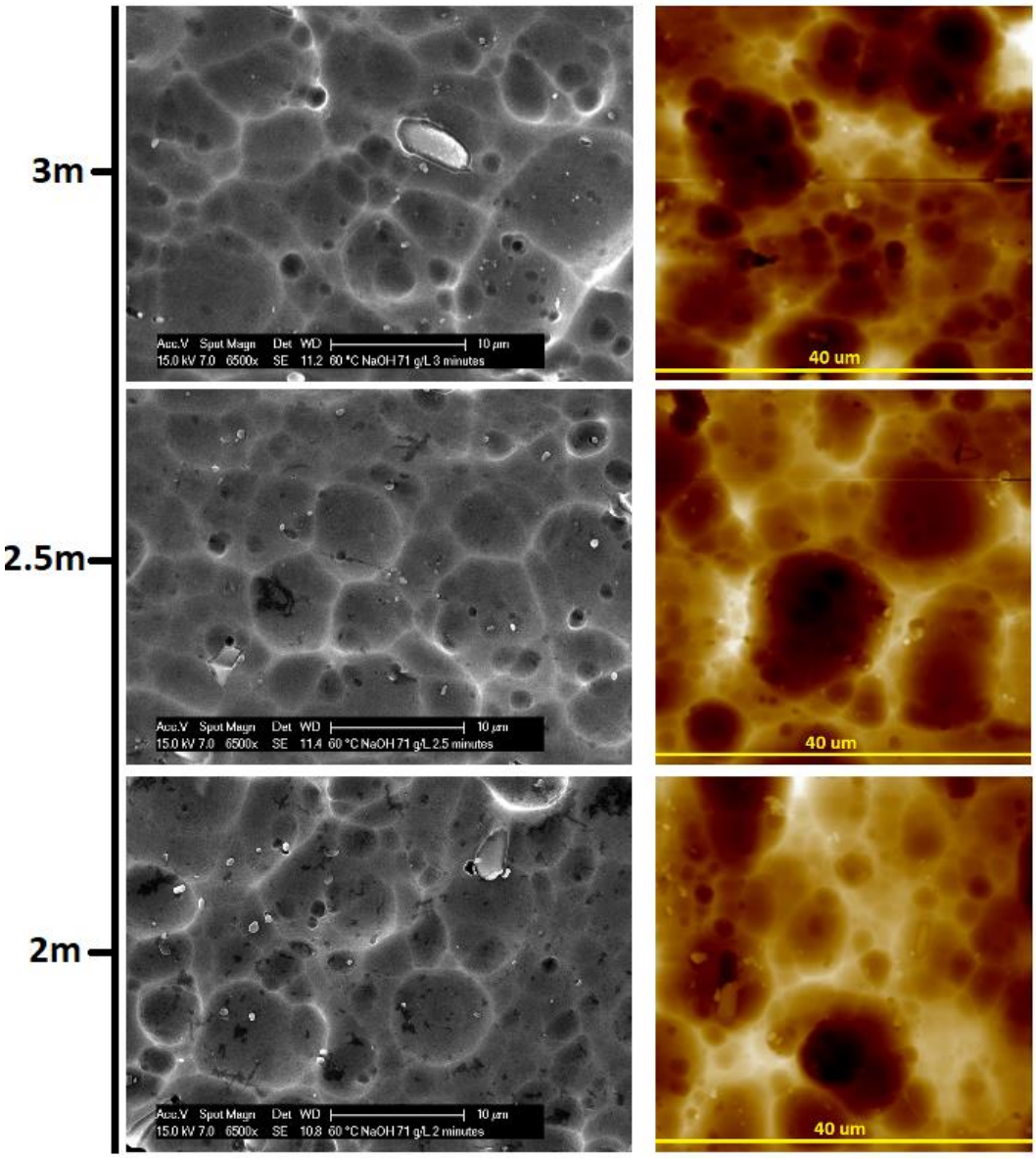

Figure 74: SEM and AFM images of NaOH etched samples at 60°C, 71 g/L- time series

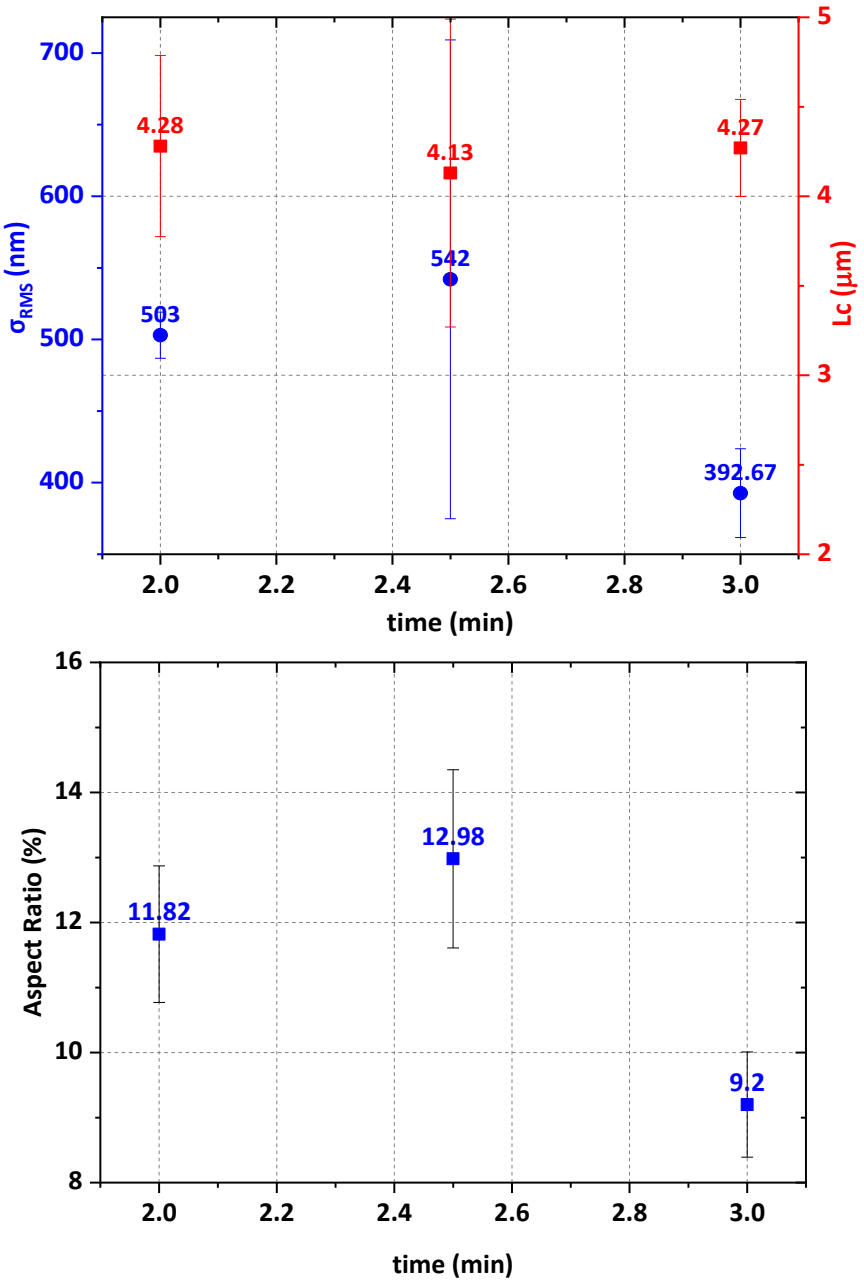

Figure 75: σ_{RMS}, Lc and AR of sample etched with NaOH at 60°C, 71 g/L- time series

The corresponding AID measurements (absolute and normalised) are shown in Figure 76 and Figure 77. These measurements are shown for only 2 and 2.5 minutes since these samples have surface morphological parameters closer to the aimed values. The sample with the higher roughness has lower specular intensity. Both samples have a similar normalised AID curve despite the sample at 2.5 minutes having a higher AR. However, the sample at 2.5 minutes exhibits a higher diffuse and lower specular intensity of reflection compared to the sample at 2 minutes (shown in Figure 78). Thus this sample has a higher reflectance haze as shown in Figure 79, which also indicates a better scattering behaviour. Considering the surface morphological parameters, AID and reflectance measurements, the sample at 2.5 minutes can be considered as the best sample among the set etched with 71 g/L of NaOH at 60°C.

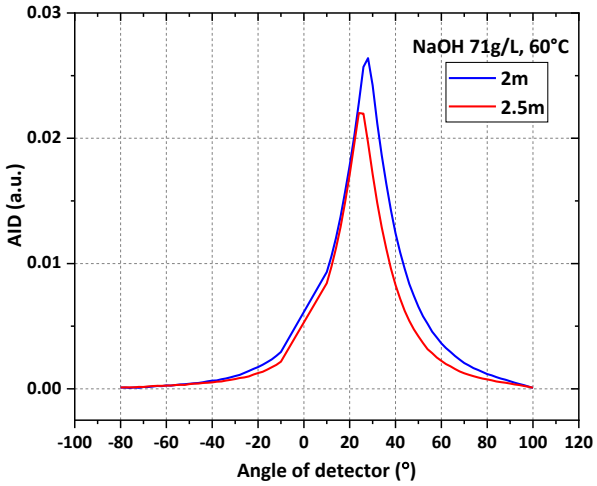

Figure 76: Angular intensity distribution of NaOH etched samples at 60°C, 71 g/L at 800 nm- time series

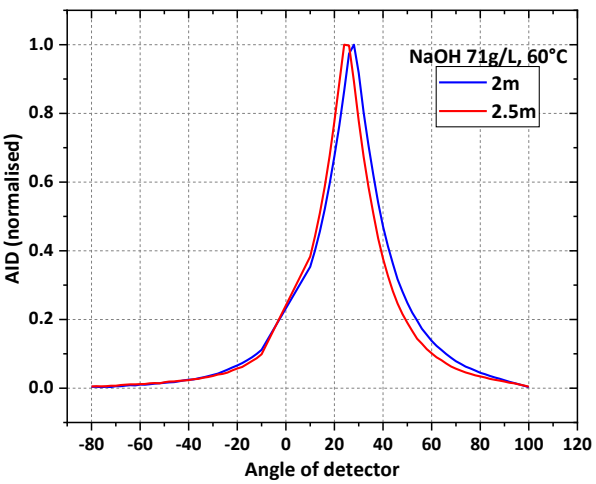

Figure 77: Normalised angular intensity distribution of NaOH etched samples at 60°C, 71 g/L at 800 nm- time series

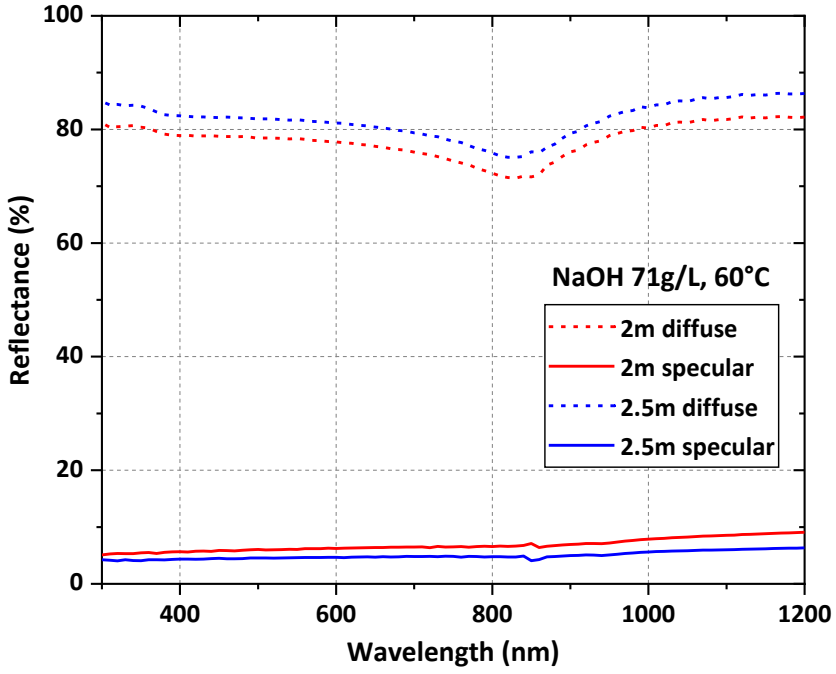

Figure 78: Diffuse and specular reflectance measurement of samples etched with 71 g/L of NaOH at 60°C for 2 and 2.5m

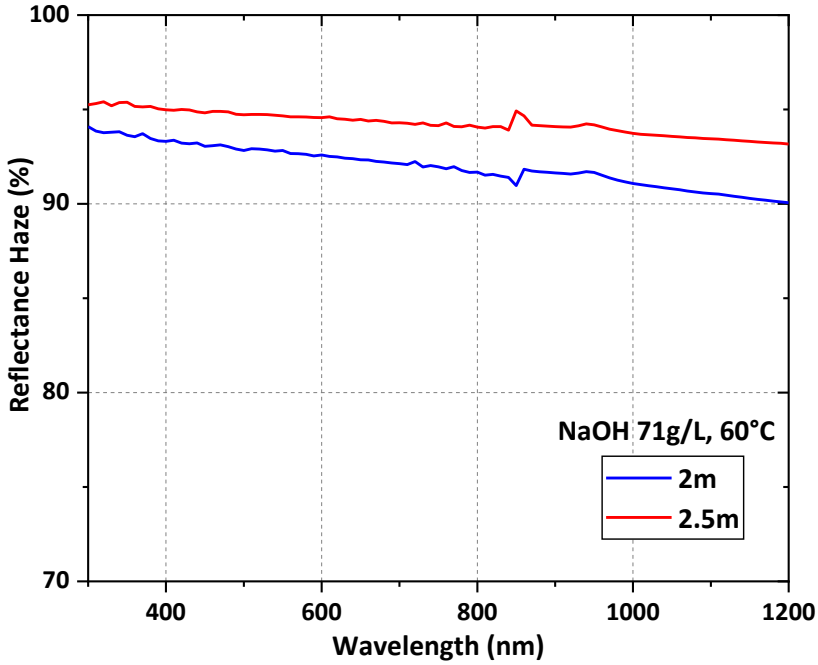

Figure 79: Reflectance haze measurement of samples etched with 71 g/L of NaOH at 60°C for 2 and 2.5m

4.4.3 Comparing 1.42M and 1.78M etching at 2.5 minutes

As mentioned in the previous sections, the samples etched with both 1.42M and 1.78M (57 g/L and 71 g/L respectively) at 2.5 minutes showed larger scattering and had larger surface morphological parameters compared to its respective time series samples. The surface morphology of these two samples can be summed up as:

Parameters	***1.42M (57 g/L)***	***1.78M (71 g/L)***
Foil thickness	*79.6*	*76.2*
RMS roughness (σ_{RMS}) (nm)	*594*	*542*
Autocorrelation length (L_C) (μm)	*4.36*	*4.13*
Aspect Ratio (σ_{RMS}/L_C) (%)	*13.58*	*12.98*

Table 9: Surface morphology characterization comparison between 1.42M and 1.78M NaOH etched samples at 2.5m

From the table, the sample etched with 57 g/L has higher values compared to the sample etched with 71 g/L for the same etching time. This sample also has an aspect ratio close to the targeted value of 14% and has a higher foil thickness which will ensure better mechanical stability as compared to the sample etched with 71 g/L.

Figure 80 and Figure 81 shows the absolute and normalised AID comparison between these two samples. The sample etched with 71 g/L has a higher specular reflection intensity compared to the sample etched with 57 g/L. This can be attributed to its lower RMS roughness (542 nm) compared to the sample etched with 57 g/L (594 nm). Also, the sample etched with 57 g/L has a broader scattering curve comparatively which can be attributed to its higher aspect ratio of 13.58%.

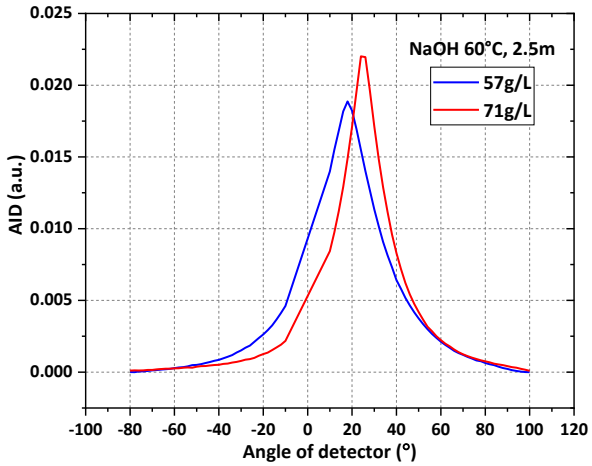

Figure 80: Angular intensity distribution comparison between NaOH etched samples with 57 g/L and 71 g/L at 800 nm at 2.5m, 60°C

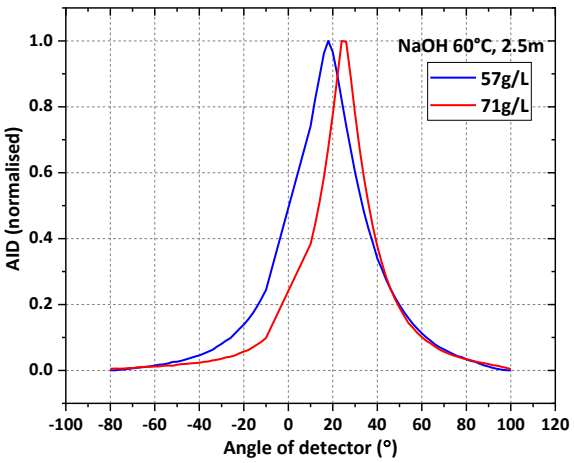

Figure 81: Normalised angular intensity distribution comparison between NaOH etched samples with 57 g/L and 71 g/L at 800 nm at 2.5m, 60°C

From Figure 82 and Figure 83, it can be seen that the sample etched with 57 g/L has a lower diffuse reflection compared to the sample etched with 71 g/L. This is opposite to the trend, since the sample at 57 g/L has the higher roughness, comparatively. A direct comparison between these two cannot be made, as the sample with 57g/L has a lower total reflectance. The sample at 57 g/L has a slightly lower value of specular reflection. The reflectance haze of both samples appears to be the same. This could be due to its higher surface morphological parameters compared to the sample with 71 g/L. To understand clearly, these parameters are listed in Table 10.

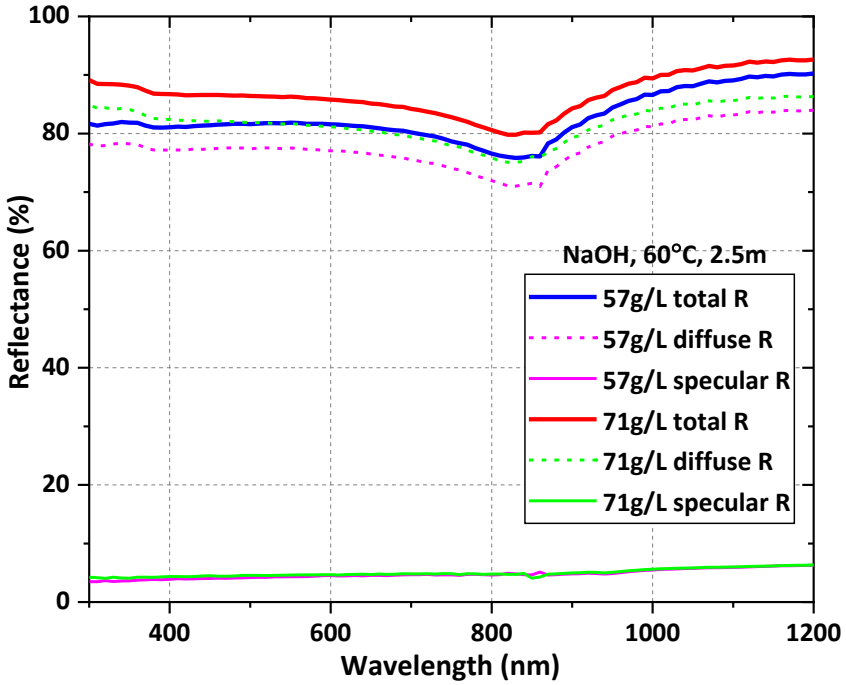

Figure 82: Total, diffuse and specular reflection comparison between NaOH etched samples with 57 g/L and 71 g/L at 2.5m, 60°C

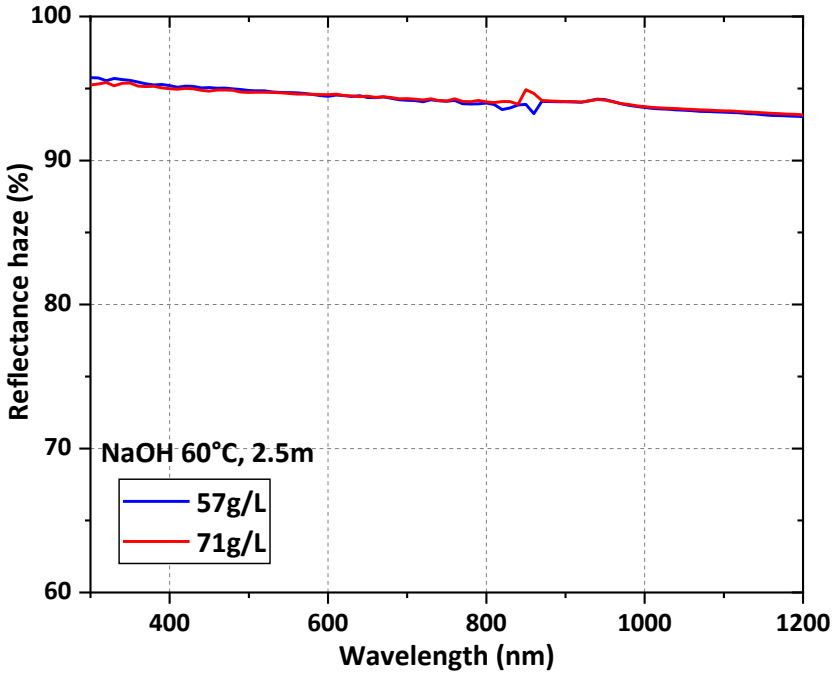

Figure 83: Reflection haze comparison between NaOH etched samples with 57 g/L and 71 g/L at 2.5m, 60°C

Parameters	***1.42M (57 g/L)***	***1.78M (71 g/L)***
Average total reflectance	*82.67%*	*86.68%*
Average diffuse reflectance	*77.91%*	*81.71%*
Average specular reflectance (total-diffuse)	*4.76%*	*4.96%*
Average haze (diffuse/total)	*94.25%*	*94.28%*

Table 10: Reflectance comparison between 1.42M and 1.78M NaOH etched samples at 2.5m

Thus, the sample etched with 57 g/L NaOH at 60°C for 2.5 minutes will be considered as one of the best lab samples and will be referred as '***NaOH60***' in the upcoming sections.

The RMS roughness, correlation length and aspect ratio values of NaOH etching are listed in Appendix IV.

4.4.4 Comparison between factory baseline and NaOH60

Table 11 lists the surface morphology parameters of the factory baseline and NaOH60. The NaOH60 sample has larger and closer to targeted values as compared to the factory baseline.

Parameters	***Factory baseline***	***NaOH60***
RMS roughness (σ_{RMS}) (nm)	*28.4*	*594*
Autocorrelation length (L_C) (μm)	*0.497*	*4.36*
Aspect Ratio (σ_{RMS}/L_C) (%)	*5.7*	*13.58*
Slope (θ_m)	*12.11°*	*17.2°*

Table 11: Surface morphology characterization comparison between factory baseline and NaOH60

Figure 84 and Figure 85 shows the absolute and normalised AID plots of NaOH60 and factory baseline samples. The NaOH60 sample has a very low specular reflection peak and a broader AID curve

compared to the factory baseline which can be attributed to the significant increase in RMS roughness and aspect ratio.

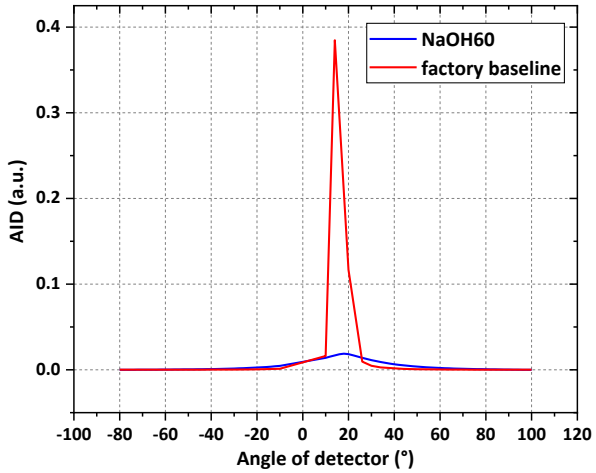

Figure 84: Angular intensity distribution comparison between NaOH60 and factory baseline at 800 nm

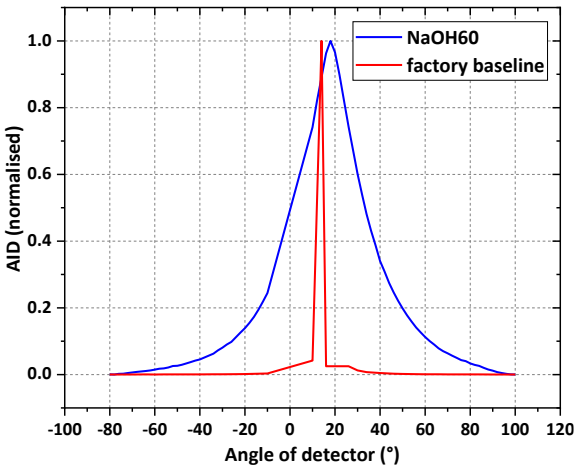

Figure 85: Normalised angular intensity distribution comparison between NaOH60 and factory baseline at 800 nm

The reflectance and haze measurement of NaOH60 and factory baseline are shown in Figure 86 and Figure 87. NaOH60 has significantly higher haze compared to the factory baseline which indicates larger scattering of light compared to the baseline. These values are listed in Table 12. The higher diffuse reflectance of NaOH60 can be explained using eqn. 4.3 (explained in section 4.3.3) where a higher RMS roughness and correlation length results in a higher diffuse reflection. Similarly, the lower specular reflection of NaOH60 can be explained using eqn. 4.4 where a higher RMS roughness results in a lower specular intensity.

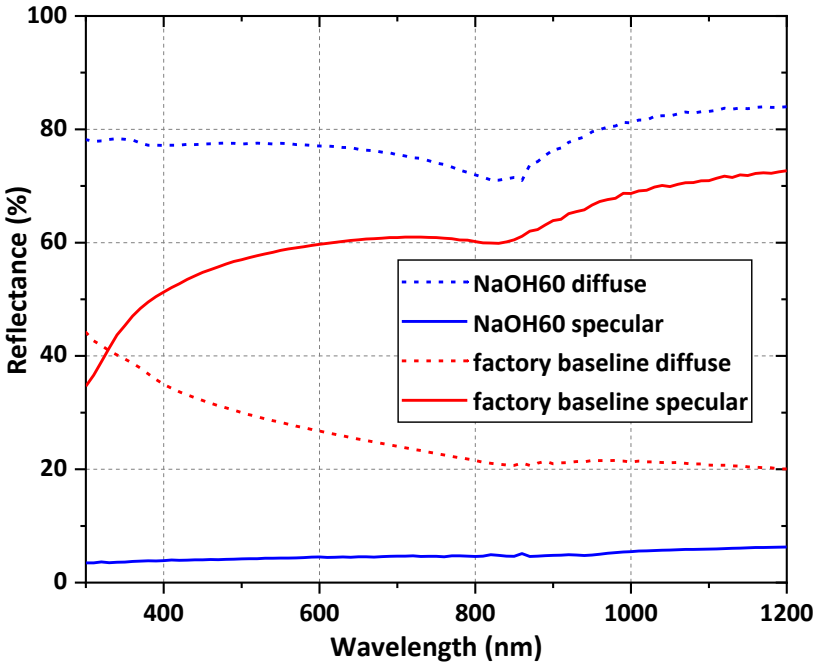

Figure 86: Diffuse and specular reflection comparison between NaOH60 and factory baseline

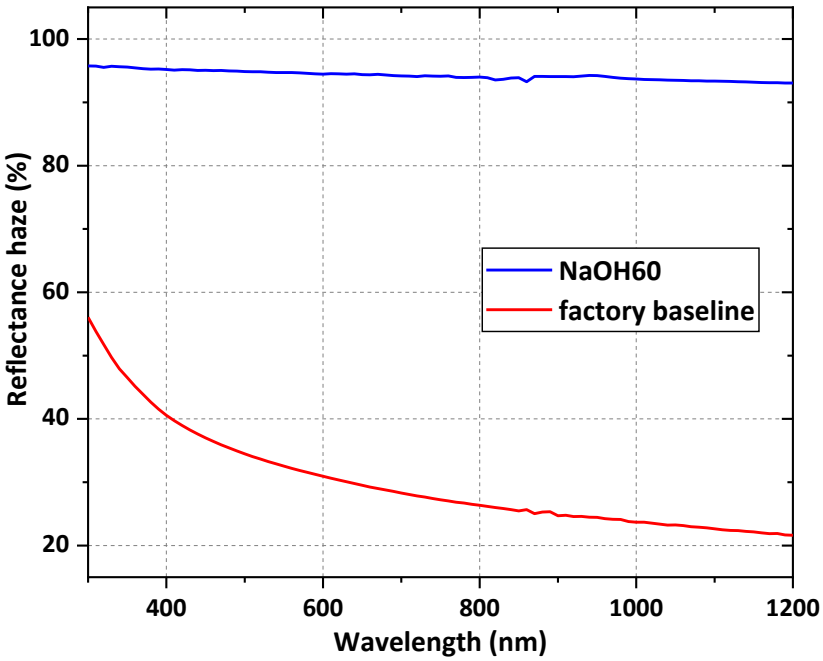

Figure 87: Reflectance haze comparison between NaOH60 and factory baseline

Parameters	*Factory baseline*	*NaOH60*
Average total reflectance	*86.7 %*	*82.67%*
Average diffuse reflectance	*25.8 %*	*77.91%*
Average specular reflectance (total-diffuse)	*60.8 %*	*4.76%*
Average haze (diffuse/total)	*29.98 %*	*94.25%*

Table 12: Reflectance comparison between NaOH60 and factory baseline

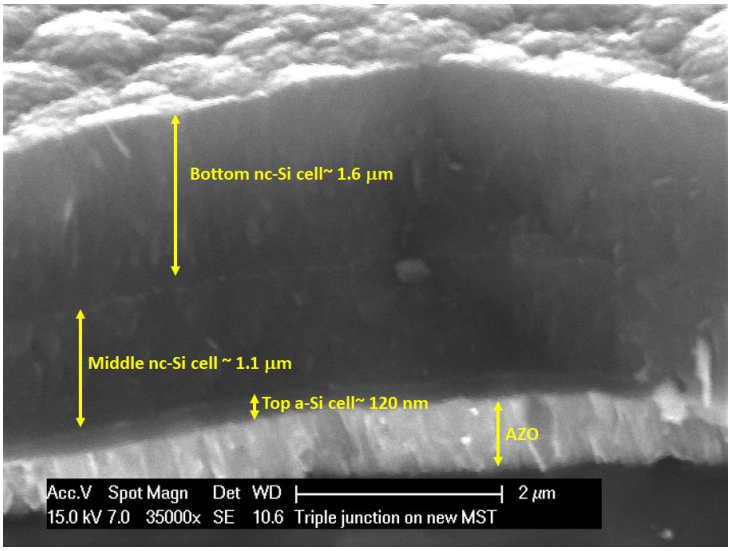

Figure 88: a-Si:H/nc-Si:H/nc-Si:H triple junction deposited on NaOH60

Figure 88 shows an a-Si:H/nc-Si:H/nc-Si:H triple junction deposited on NaOH60. The layers deposited onto NaOH60 followed the texturing pattern, without any visible cracks and resulted in high quality materials, as opposed to the factory baseline texturing as shown in Figure 50 (a).

Thus, the following samples- KOH70, KOH60 and NaOH60 has higher values of surface morphological parameters and scattering compared to the factory baseline, which are closer to the targeted values:

(i) KOH70- Sample etched with 100 g/L (1.78M) KOH at 70°C for 2 minutes
(ii) KOH60- Sample etched with 100 g/L (1.78M) KOH at 60°C for 3 minutes
(iii) NaOH60- Sample etched with 57 g/L (1.42M) NaOH at 60°C for 2.5 minutes

4.5 Additives

Additives such as polyethylene glycol 400 (PEG-400), sodium gluconate and sodium nitrate are added to the factory baseline. To investigate the effects of these 3 compounds in etching, these are added one by one to the etching solution. The thickness measurement of these samples is shown in Figure 89. Addition of one or any combination of these additives results in a higher etch rate- this can be noticed from the lower thickness at any time compared to the thickness of the foil without any additives. In adding these additives individually, the addition of sodium nitrate resulted in the least foil thickness. Sodium nitrate is an 'equalizing agent' which is added to get a uniform etch rate. It is also said to inhibit hydrogen bubble formation which can stick to the Al foil and inhibit the etching reaction, by forming ammonia gas which can be vented out of the etching tank comparatively easily [58]. Addition of sodium gluconate or PEG individually to the etching solution increased the etch rate as well, but not as much as the increase due to addition of nitrate. The gluconate and PEG can be termed as '*chelating agents*' and '*surfactants*'. Chelating agents will form bonds with the Al ions and extracts it forming a water- soluble compound. These are added to inhibit redeposition of removed Al onto the foil [59] [60]. Surfactants increases the wettability of the foil by lowering the surface tension between the etching solution and the foil [61]. PEG is a type of non-ionic surfactant, has good capacity to increase wettability and has a lower etch rate compared to an ionic surfactant. They foam less compared to ionic surfactants as it is less sensitive to hardness of the water used [61] [62]. Addition of all three additives resulted in the highest etch rate and the foil thickness was significantly reduced. In all the cases, the smut layer was easier to remove in the acid-desmutting step.

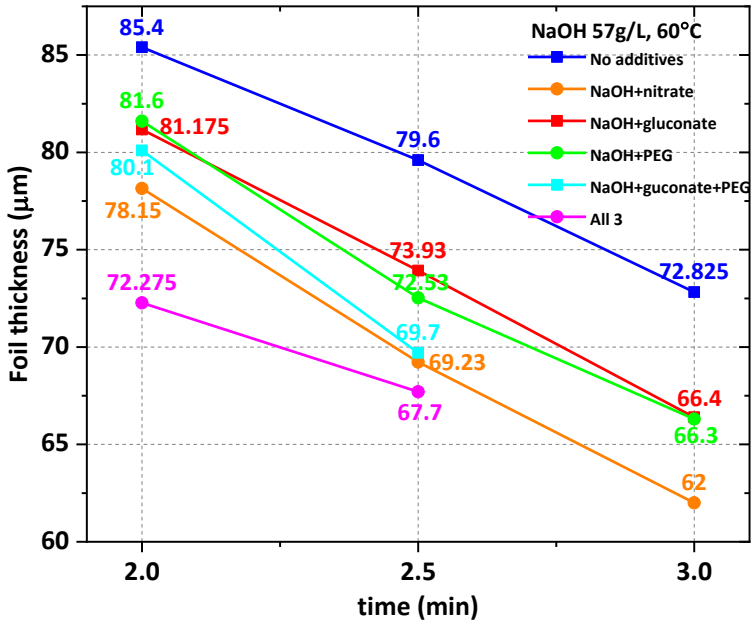

Figure 89: Thickness measurement of Al foil at NaOH 57 g/L, 60°C with and without additives- time series

Figure 90 shows the SEM images of NaOH etched sample with 57 g/L, 60C for 2 minutes, without and with the addition of one or a combination of additives. It can be clearly seen that addition of any additives has improved the uniformity of texturing, i.e. the density of craters is higher. Lower spread (error bar) of the surface morphological parameters also indicates uniformity. Figure 91 and Figure 92 shows the RMS roughness and correlation lengths with spread for samples etched with 57 g/L NAOH at 60°C for 2 and 2.5 minutes without any additives and with PEG and sodium gluconate. The samples with PEG and gluconate have a significantly lower spread compared to the ones without any additives. The roughness and correlation length values are slightly lower for the samples with additives. This can be due to the formation new craters densely covering the entire surface of the foil.

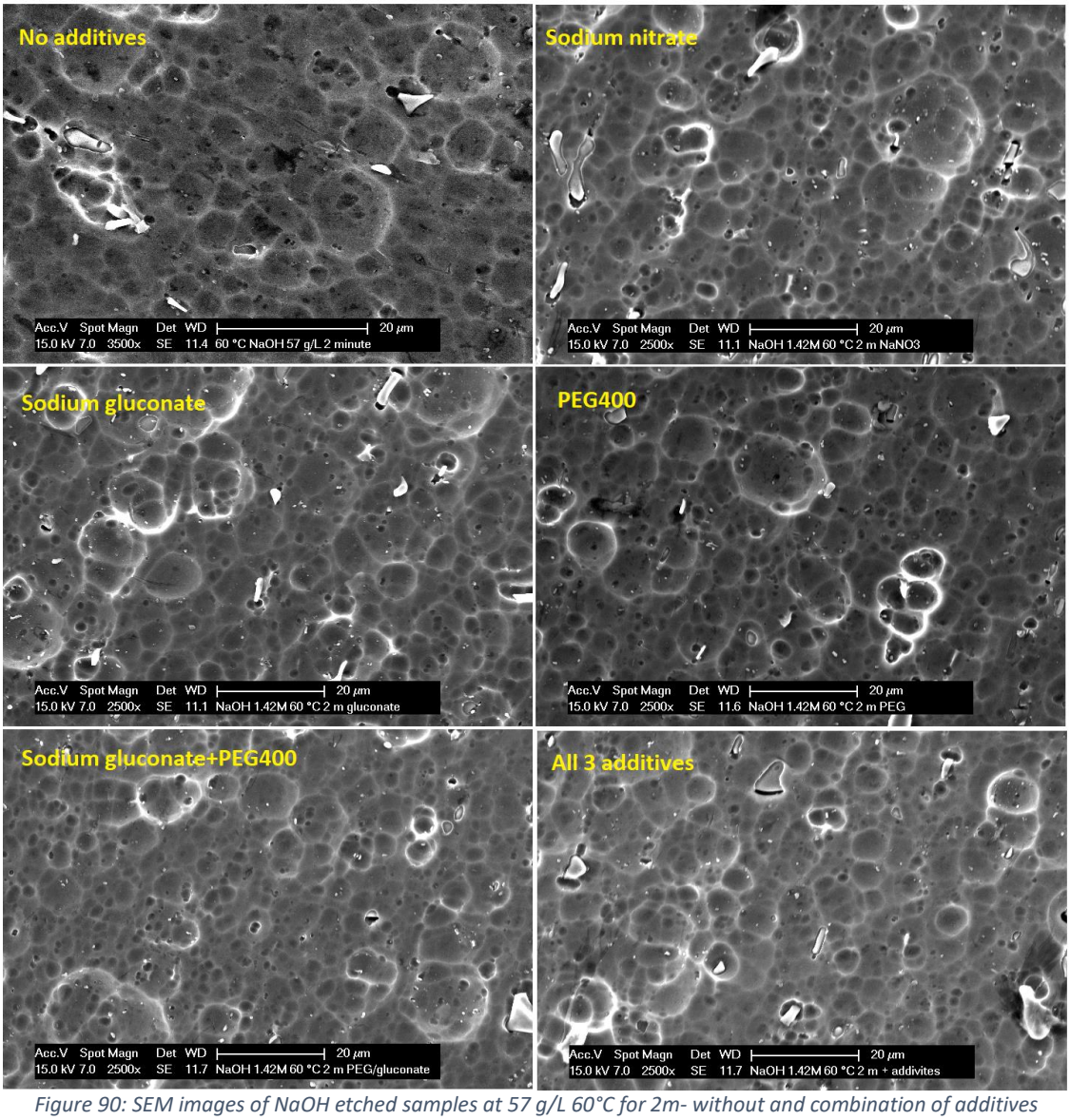

Figure 90: SEM images of NaOH etched samples at 57 g/L 60°C for 2m- without and combination of additives

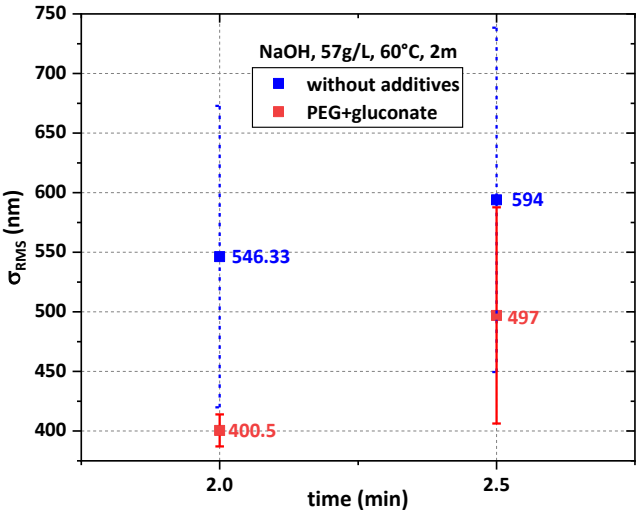

Figure 91: RMS roughness with error bars for 57 g/L NaOH etched samples at 60°C, 2 and 2.5m, with and without additives

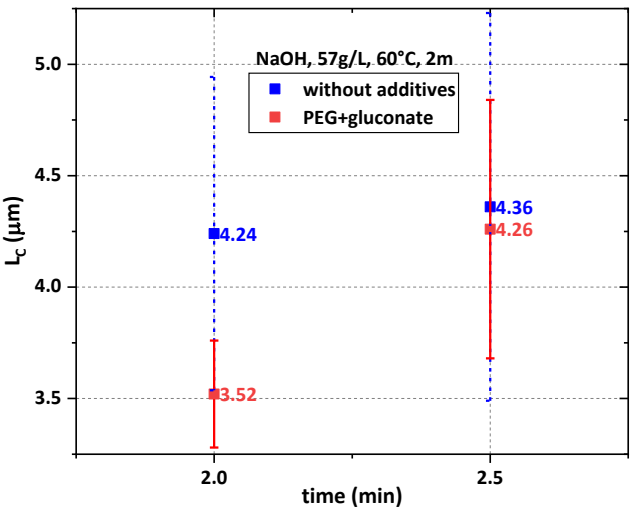

Figure 92: Correlation length with error bars for 57 g/L NaOH etched samples at 60°C, 2 and 2.5, with and without additives

4.6 Speed of rotation of etchant

In all the experiments, a magnetic stirrer at 100 RPM (rotations per minute) was employed to ensure that the etchant is homogenous, and temperature is evenly distributed. Stirring is one of the factors that influences the reaction rate of aluminium in KOH/NaOH. Stirring also ensures that the by-products diffuse away from the surface of the foil back into the solution. This section investigates the influence of speed of stirring on the RMS roughness and correlation length.

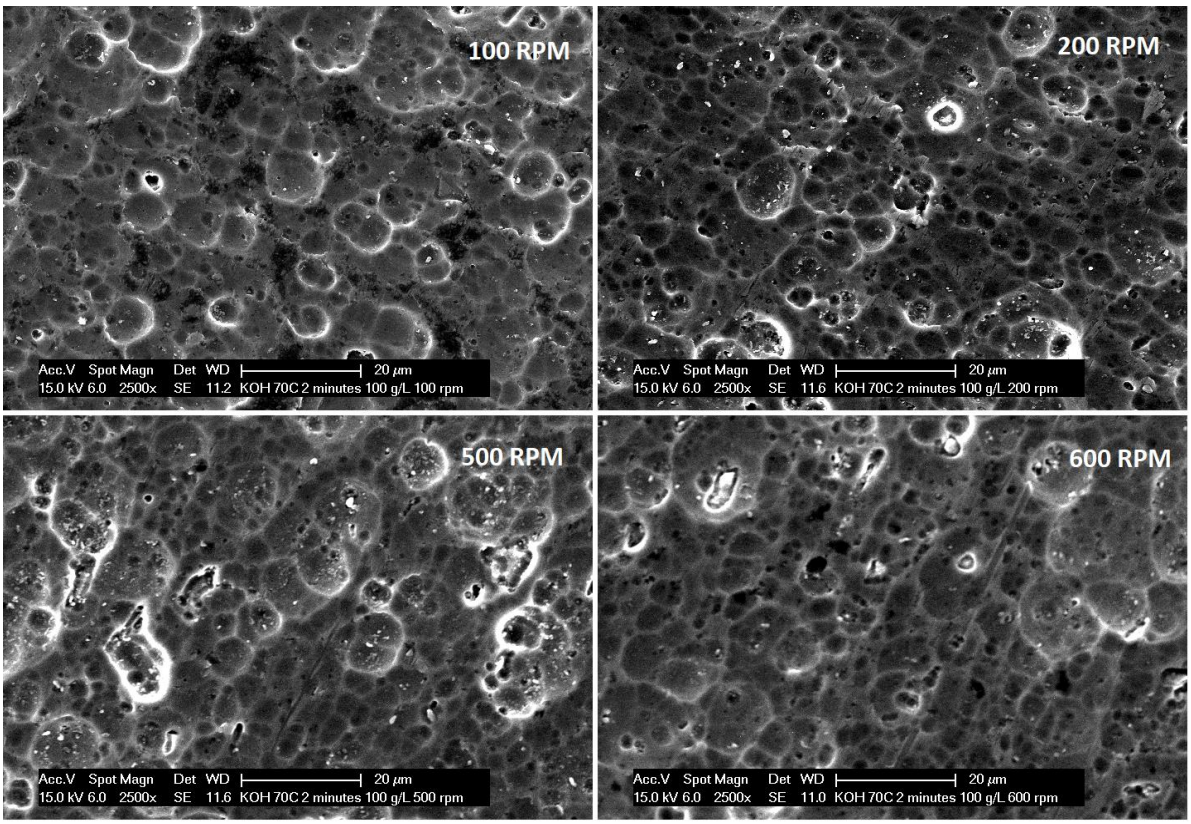

Figure 93: SEM images of KOH etched samples with 100 g/L, 70°C for 2 minutes- RPM series

Figure 93 shows the SEM images of samples etched with 100 g/L KOH at 70C for 2 minutes at 100, 200, 500 and 600 RPM. Theoretically, as mentioned above, as stirring increases, the solution and temperature gets homogenous. Thus, there is a better contact of the solution with the foil and the diffusion of reaction by-products (smut in this case) off the foil is improved resulting in a higher RMS roughness and correlation length values. This is confirmed by the values derived from the AFM images as shown in Figure 94. The sample at 100 RPM has the lowest RMS roughness and correlation length, and the sample at 600 RPM has the highest RMS roughness and correlation length values. Thus, it can be said that, as the speed of stirring increases, the reaction rate (and thus the etch rate) increases, resulting in an increase in roughness and correlation length. The values are listed in Appendix VIII.

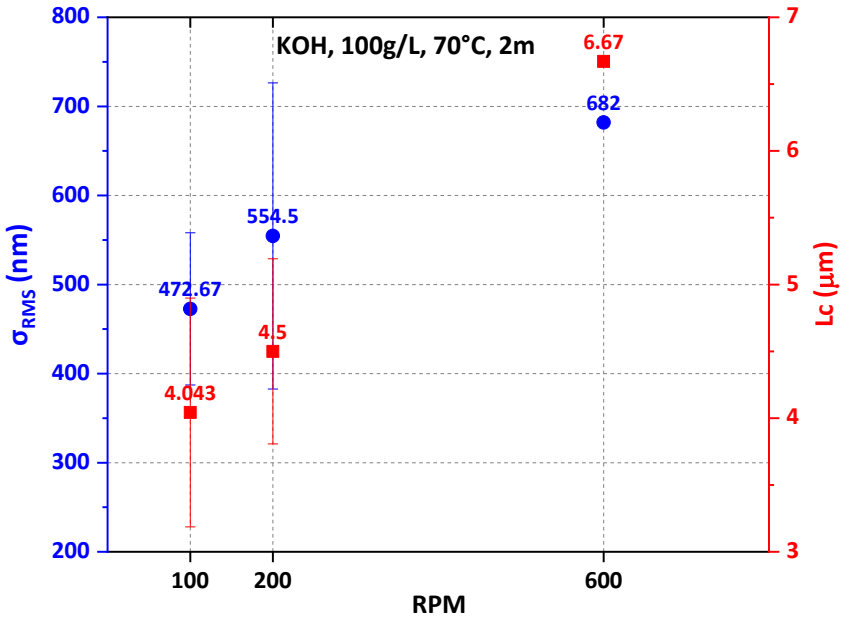

Figure 94: σ_{RMS} and Lc values of KOH etched samples with 100 g/L 70°C for 2m, at 100, 200 and 600 RPM

4.7 Sacrificial layer etching

In this technique an additional layer of TCO (e.g. aluminium doped zin oxide- AZO) is deposited on to the Al foil before etching as described in section 3.1.2.

4.7.1 HF etching

After the AZO is deposited on the Al foil, the sample is wet etched using hydrofluoric acid (HF). The ratio of acid to peroxide to water (HF: H_2O_2: H2O) used is 1:2:10. The sample is etched at room temperature (25°C) for a duration of 3 minutes. An AFM image of the sample is shown in Figure 95.

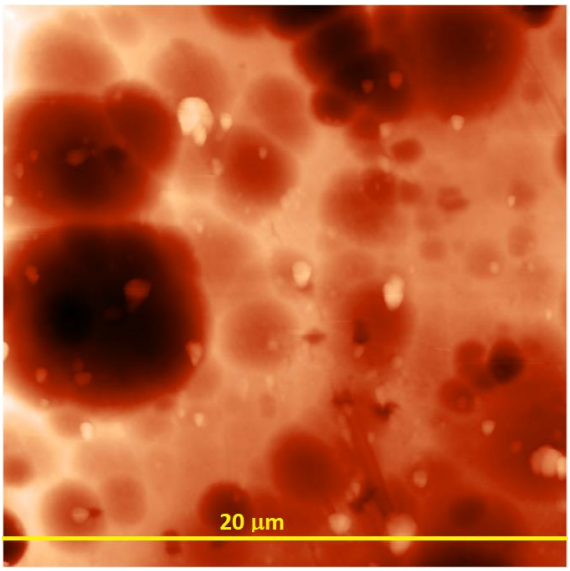

Figure 95: AFM image of AZO on Al etched with HF at 25°C for 3m

From the AFM image, the surface morphology parameters are derived as follows:

- *RMS roughness (σ_{RMS}) (nm) = 249 nm*
- *Correlation length (Lc) (µm) = 2.885 µm*
- *Aspect ratio (AR) (%) = 8.64%*

These parameters are an improvement considering the factory baseline. The AID curves are shown in Figure 96 and Figure 97. The AZO:HF sample has a lower specular peak and a broader scattering due to its higher roughness and aspect ratios compared to the factory baseline.

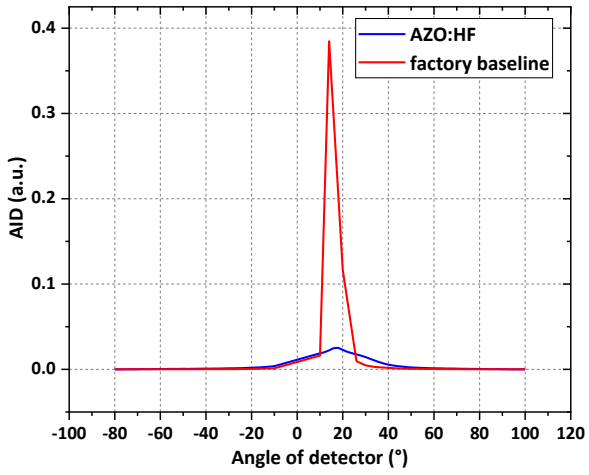

Figure 96: Angular intensity distribution of AZO:HF and factory baseline at 800 nm

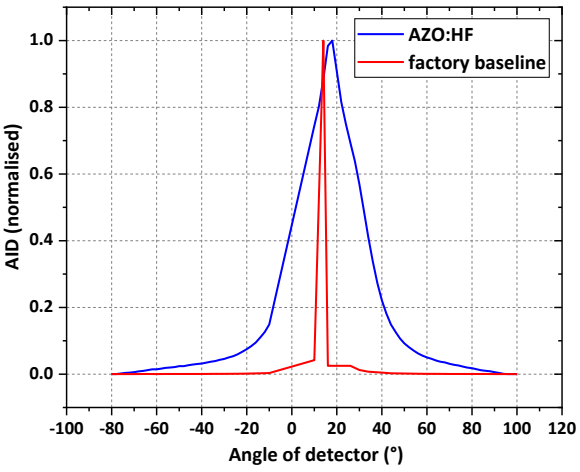

Figure 97: Normalised angular intensity distribution of AZO:HF and factory baseline at 800 nm

However, sacrificial etching with HF resulted in highly non-uniform texturing as compared to sacrificial layer etching with KOH (as shown in the next section). This will also call for the replacement of already existing R2R etching machine which employs NaOH. Additionally, HF is a highly dangerous. Hence, this etching technique is not investigated further.

4.7.2 KOH etching

The AZO deposited Al foil is wet etched using KOH with a concentration of 85 g/L. The etching duration is 3 minutes and the samples are etched at 35, 50 and 70°C. The AFM and SEM images of these samples are shown in Figure 98, Figure 99 and Figure 100.

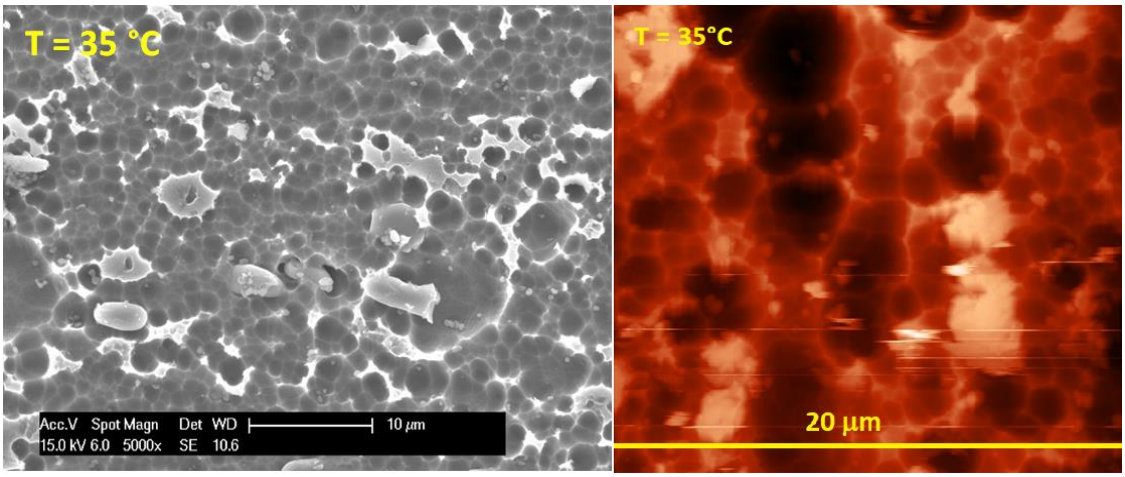

Figure 98: SEM and AFM images of AZO:KOH at 35°C

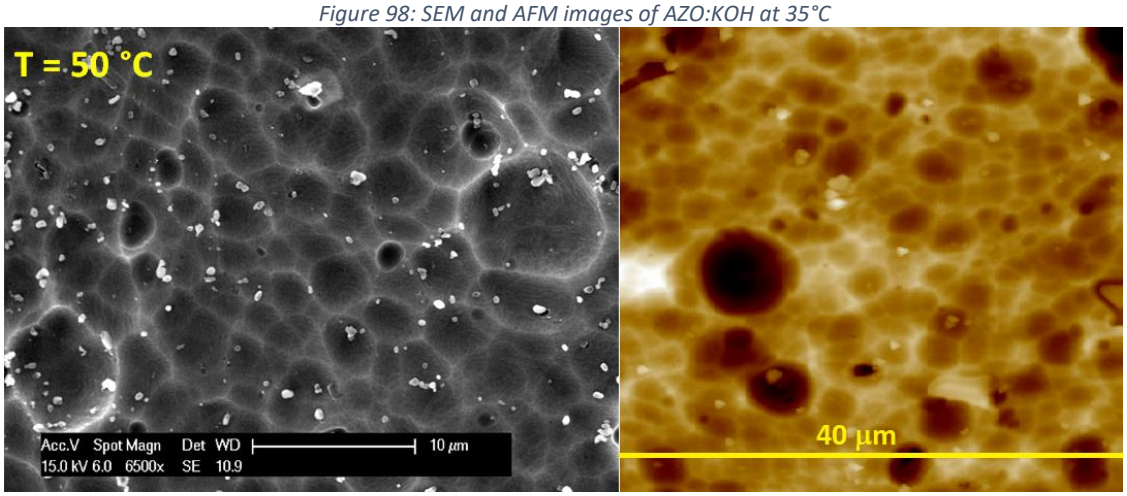

Figure 99: SEM and AFM images of AZO:KOH at 50°C

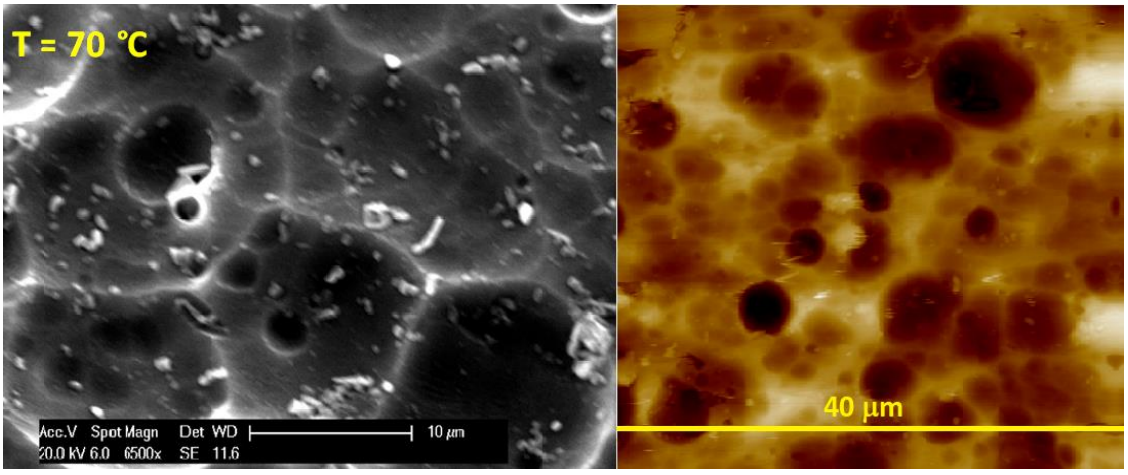

Figure 100: SEM and AFM images of AZO:KOH at 70°C

From these images the following can be derived:

Parameters	AZO:KOH at 35°C	AZO:KOH at 50°C	AZO:KOH at 70°C
RMS roughness (σ_{RMS}) (nm)	408	484 ± 204.18	425.67 ± 67.26
Autocorrelation length (L_C) (μm)	1.86	3.34 ± 0.965	4.66 ± 0.675
Aspect Ratio (σ_{RMS}/L_C) (%)	21.8	14.06 ± 6.39	9.17 ± 1.01

Table 13: Surface morphology characterization of AZO:KOH at 35, 50 and 70°C

These values are listed in Appendix 7.19 and Appendix 7.20. Note that the error bar of parameters listed for AZO:KOH at 35°C does not have any uncertainties as only 1 measurement was taken. From the data, no clear trend of texturing is observed. However, from the SEM images, nature of craters looks slightly different (overlapping and dense) from the samples at 50 and 70°C. This could be because the Al has not started etching and we are still viewing the AZO. The sample at 50°C shows Lc and AR close to the targeted values. Also, compared to HF sacrificial layer etching, etching with KOH resulted in a much more uniform texturing.

However, this type of texturing also resulted in surface morphological values similar to that of bare Al etching using KOH/NaOH. Thus, it is not economically feasible to implement an additional deposition step in the R2R process which does not result in a significant improvement compared to the bare Al etching. Hence, this technique has only been considered for lab depositions and not for further R2R testing recipes.

4.8 R2R industrial testing

As mentioned in section 4.4.4, the following are the best lab samples which can be adapted to the R2R process:

(i) KOH70- Sample etched with 100 g/L (1.78M) KOH at 70°C for 2 minutes
(ii) KOH60- Sample etched with 100 g/L (1.78M) KOH at 60°C for 3 minutes
(iii) NaOH60- Sample etched with 57 g/L (1.42M) NaOH at 60°C for 2.5 minutes

However, the following limitations need to be taken into account while adapting the best lab recipes to an optimum R2R recipe:

(i) The final thickness of the foil should be ~ 95µm to ensure mechanical stability during depositions
(ii) The etching temperature: The factory baseline etching is done at 35°C in the etching machine and hence increasing the temperature should be in a controlled manner
(iii) Etching time needs to take into account the throughput of the etching machine and the capability of the foil transport mechanism. There is a minimum and maximum speed at which the roll can traverse in the machine. All these factors affect the cost of the process as well

Since the machine already employed NaOH for factory baseline etching, for the first test run, the etchant is chosen to be NaOH. The concentration is selected at 57 g/L as it is one of the best lab sample concentrations obtained. A series of lab experiments were done at a reduced temperature of 45 and 50°C and a time interval of 1.5, 1.8, 2 and 2.5 minutes, considering the limitation of the etching

machine. From thickness measurements and through visual observations to determine the reflectance haze of the samples, a final temperature of 50°C and an etching time of 1.8 minutes is selected for the R2R recipe. A time below 1.8 minutes and below 50°C resulted in a highly reflective sample. Whereas, time longer than 1.8 minutes cannot be selected since there is a minimum speed of the R2R machine, even though it resulted in a highly hazy sample. The determination of the selection process is shown in Figure 101.

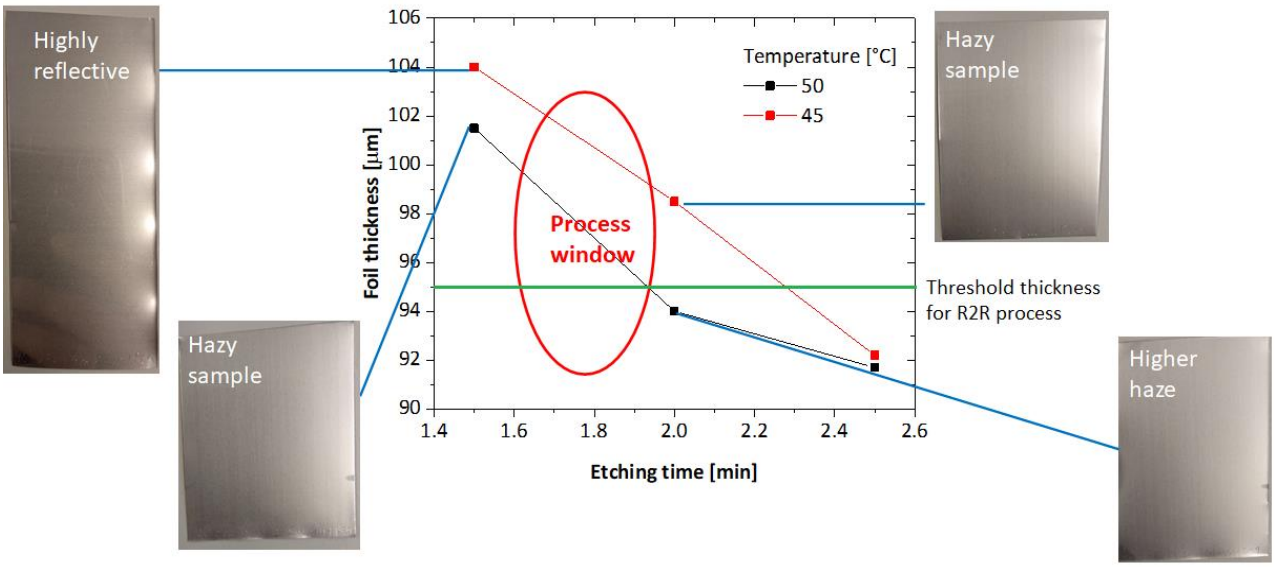

Figure 101: Determination of process window for R2R test run

4.8.1 Comparison between factory baseline and test run

The aforementioned R2R recipe was implemented in R2R etching machine on a 350 mm wide, 250 m long Al foil. A sample taken from this particular foil is labelled as 'test run'. Table 14 lists the surface morphological parameters of the factory baseline and the test run samples. For the test run samples, there is a significant improvement of the parameters compared to the factory baseline. Figure 102 shows the AFM images of the test run foil and the factory baseline.

Parameters	***Factory baseline***	***Test run***
RMS roughness (σ_{RMS}) (nm)	*28.4*	*233*
Autocorrelation length (L_C) (μm)	*0.497*	*2.27*
Aspect Ratio (σ_{RMS}/L_C) (%)	*5.7*	*10.26*
Slope (θ_m)	*12.11°*	*12.32°*

Table 14: Surface morphology characterization comparison between factory baseline and test run

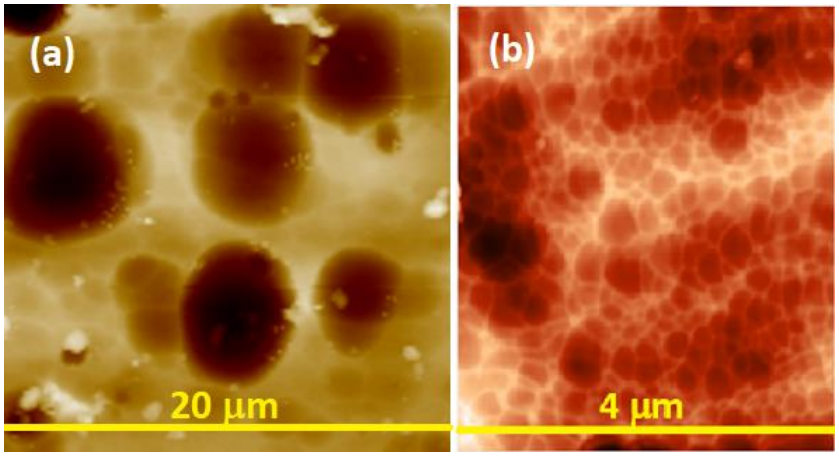

Figure 102: AFM images of (a) test run Al foil (b) factory baseline

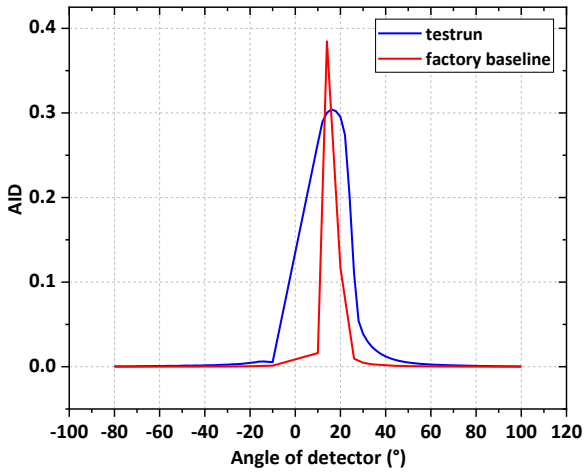

Figure 103: Angular intensity distribution of test run and factory baseline at 800 nm

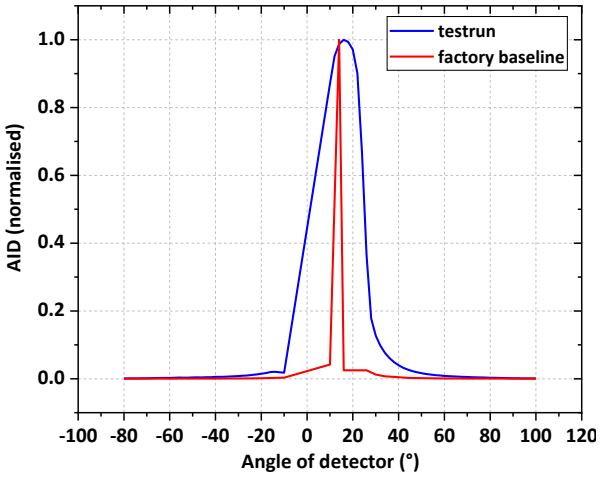

Figure 104: Normalised angular intensity distribution of test run and factory baseline at 800nm

Figure 103 and Figure 104 shows the absolute and normalised AID curves of test run and factory baseline. The test run sample has a lower specular peak compared to the factory baseline which is due to the increased RMS roughness. Also, since the test run sample has a higher aspect ratio, it has a broader AID curve as well, i.e. higher scattering compared to the baseline.

The reflectance and haze measurement of test run and factory baseline are shown in Figure 105 and Figure 106. Test run texturing has a higher haze due to its high diffuse component compared to the factory baseline, especially in the higher wavelengths. This is due to the increased feature sizes of the test run sample compared to the factory baseline. These values are listed in Table 15.

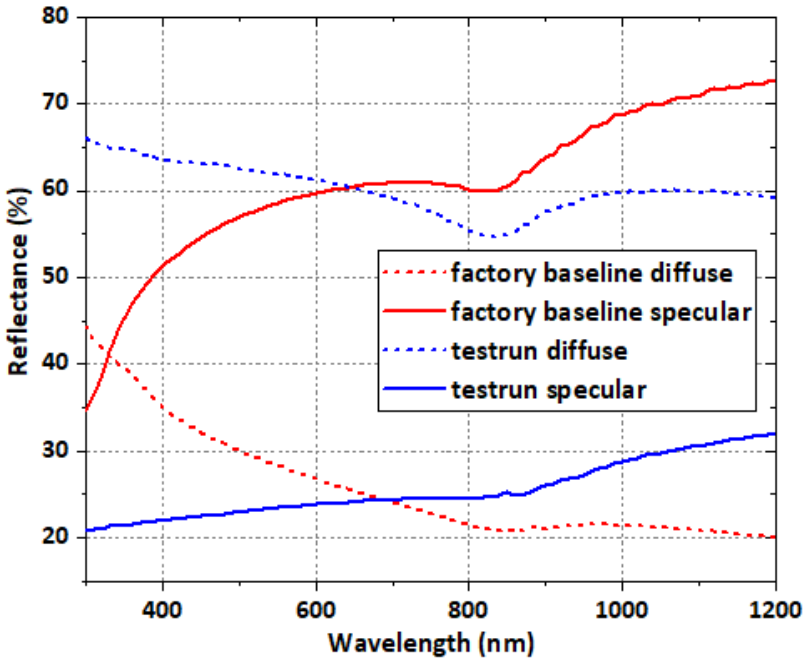

Figure 105: Diffuse and specular reflection comparison between test run and factory baseline

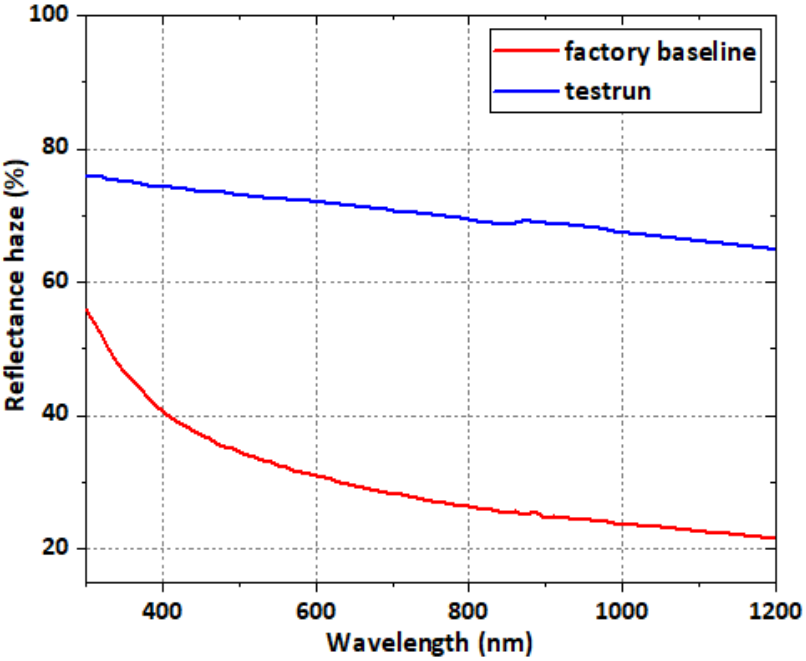

Figure 106: Reflectance haze comparison between test run and factory baseline

Parameters	***Factory baseline***	***Test run***
Average total reflectance	*86.7 %*	*86 %*
Average diffuse reflectance	*25.8 %*	*66.07 %*
Average specular reflectance (total-diffuse)	*60.8 %*	*19.8 %*
Average haze (diffuse/total)	*29.98 %*	*76 %*

Table 15: Reflectance values of test run and factory baseline

As mentioned in section 1.3, to achieve modulated surface texturing, the crater like structures (in the Al foil) needs to be superimposed with the pyramidal texturing of the FTO, while ensuring that the FTO textures follows the texturing of the Al foil. Since the factory baseline features are very small, the

FTO does not adapt the texturing of the Al foil. Thus, the texturing in factory baseline is essentially that of the FTO only. This can be seen in Figure 107.

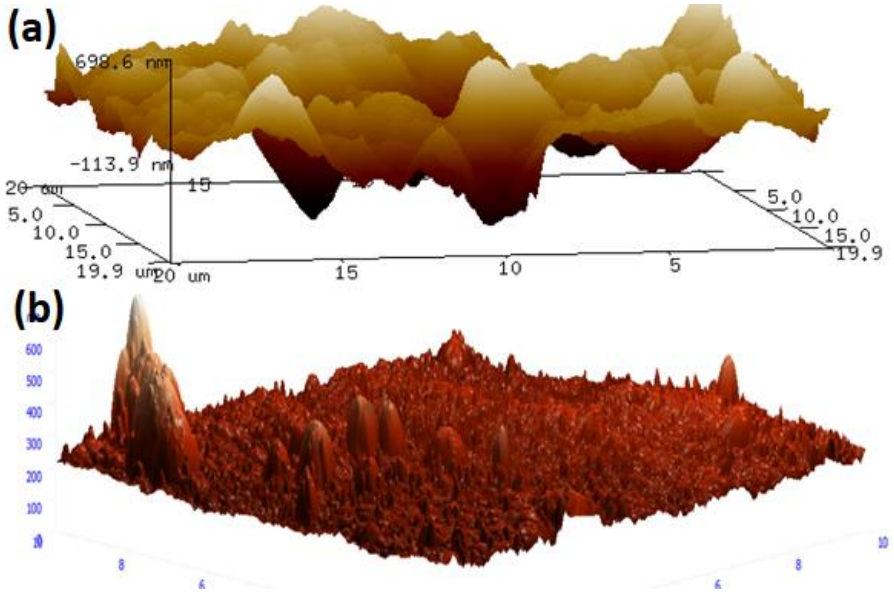

Figure 107: 3D AFM image of (a) test run Al foil with FTO (b) factory baseline foil with FTO

The test run Al foil features are significantly larger than the factory baseline and hence when the FTO is deposited, it adapts the texturing of the Al foil, i.e., 'conformality' of texturing is maintained. This can be clearly seen from the SEM images shown in Figure 108.

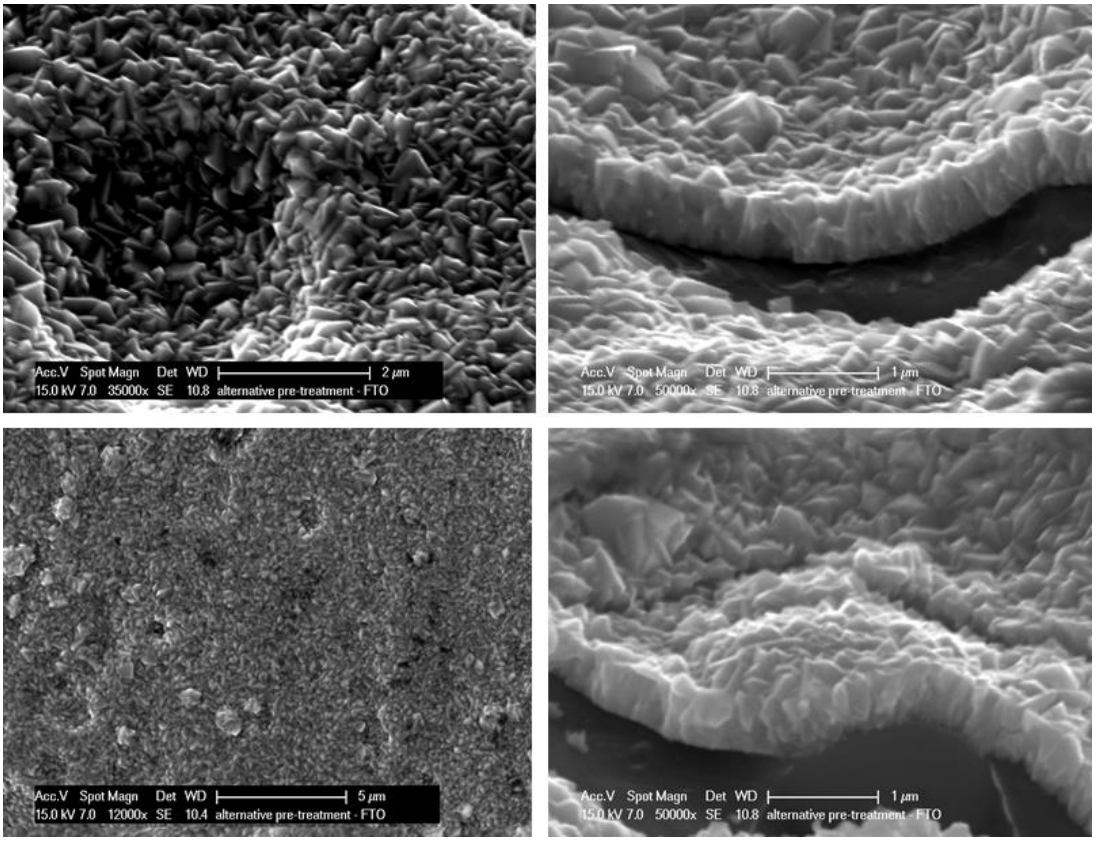

Figure 108: Top and cross-sectional SEM images of test run foil with FTO

Figure 109 shows an a-Si:H/nc-Si:H tandem cell deposited on the test run texturing. Compared to the factory baseline texturing, there are less visible cracks in the nc-Si layer. The texturing of the Al foil is also adapted by the other layers. However, in the next image, some high contrast lines can be seen which can indicate cracks or silicon vacancies. This implies that the texturing is not as uniform as expected.

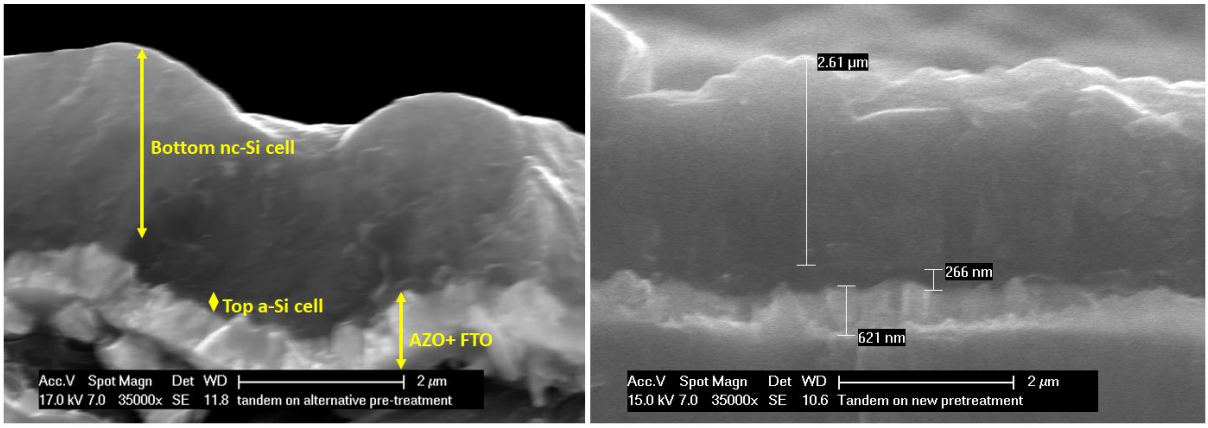

Figure 109: a-Si:H/nc-Si:H tandem cell deposited on test run texturing

While the surface features of test run are larger than the factory baseline texturing, it is not as close to the targeted values as the best lab textures (KOH70, KOH60 and NaOH60). The trade-off here is between the final thickness of the foil and the targeted surface morphology. While the targeted morphology can be achieved by increased temperatures and time, it will result in a foil which is less than 95 µm thick. However, maintaining 95 µm thickness from a starting thickness of 110 µm will not yield the best texturing. This can be solved by using a thicker foil. However, this will also be constrained by the mechanical limitations of the R2R machines. Another solution is to induce single-sided texturing where one side of the Al foil is coated/covered by an etch resistant material. This will ensure more controllability of the etching and will limit the etch rate. This also, brings in an additional processing step in the R2R line which can increase the cost.

4.9 Optical modelling

The AFM data obtained for the above samples are used for optical simulations using GenPro4 to understand the effectiveness of texturing. Using this simulation tool, the current density distribution in each layer of solar cell can be determined. The following assumptions are made for simulation:

- Layers thinner than 1 µm are modelled as 'coatings' where the reflectance is wavelength dependent, and hence there will be presence of interference fringes in the results
- All the layers are assumed to have the same texturing as that of the Al foil
- The factory baseline texturing is modelled using 'wave' model which uses scalar scattering theory, since it has surface features much smaller than the wavelength

4.9.1 Single junction nc-Si:H cells

The model of the single junction nanocrystalline silicon solar cell used for simulation is shown in Figure 110. nc-Si:H i-layer of 2.3 µm is the absorber layer. The *n* and *k* values of the all the layers and the AFM data of the textured Al foil are given as inputs for the simulations. All the layers with thickness greater

than 1 µm are modelled as '*layers*' and the layers with thickness less than 1 µm are modelled as '*coatings*'(theory mentioned in section 3.4). The parameters and thicknesses used for the simulation are listed in Table 16.

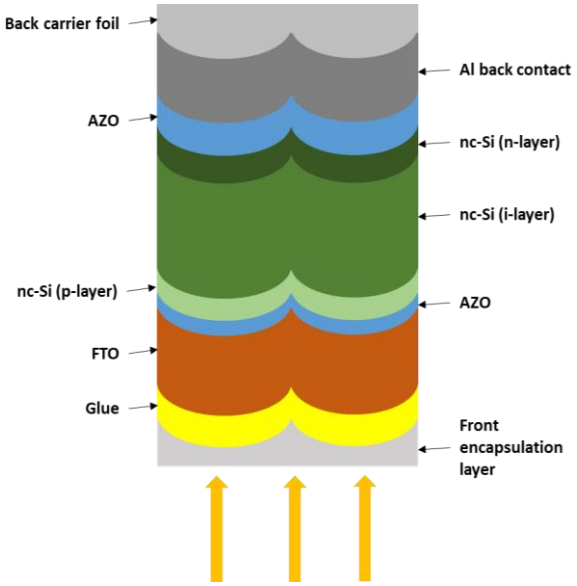

Figure 110: Model of single junction nc-Si cell

Layer	Thickness (µm)	Lay/Coat
Front encapsulant	25	Lay
Glue	500	Lay
FTO	0.7	Coat
AZO	0.005	Coat
p-nc-SiO_X:H	0.025	Coat
i-nc-Si:H	2.3	Lay
n-nc-SiO_X:H	0.025	Coat
AZO	0.08	Coat
Al back contact	0.3	Coat
Back carrier foil	125	Lay

Table 16: Parameters for single junction nc-Si:H cell

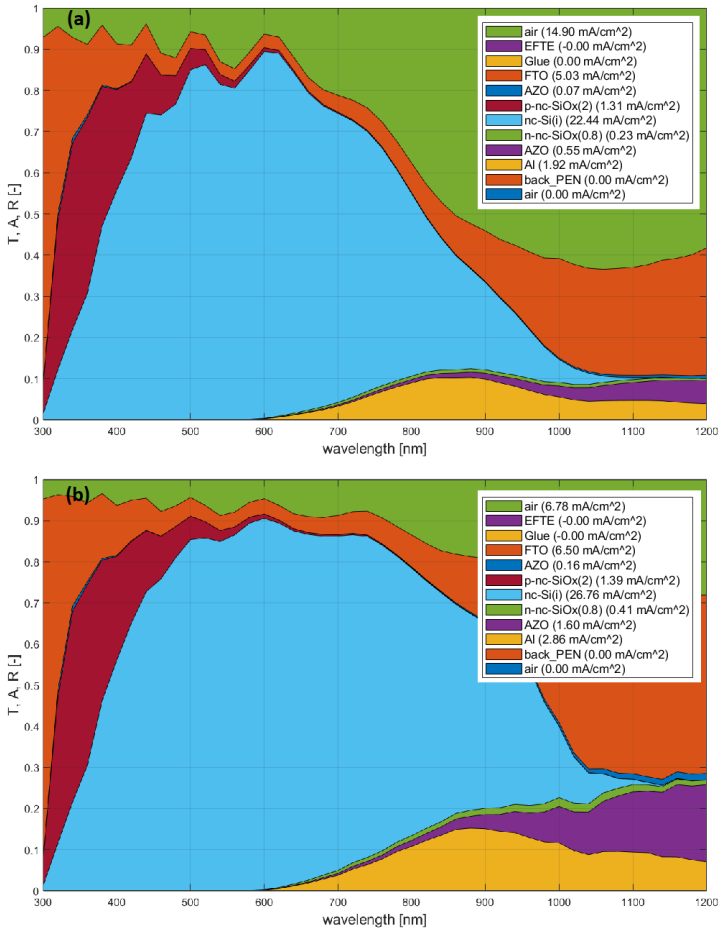

Figure 111: Optical loss/gain curve and generated photocurrent densities of (a) factory baseline (b) KOH60

The simulations were done for Al texturing data based on factory baseline, test run, KOH70, KOH60, NaOH60 and for no-texturing. As mentioned in section 3.4, the Al texturing with very small features (factory baseline) were modelled using wave model which uses scalar scattering theory, and the other textures having larger features were modelled using ray model which uses ray-tracing. The sample with no texturing is simulated using the flat model. An example of the simulation result is shown in Figure 111, where the T, R, A values are shown for each wavelength.

Table 17 lists the generated photocurrent densities in the absorber layer. Compared to the no-texturing sample, all the others have a higher current density. The best texturing- KOH60, NaOH60 and KOH70 have a significant improvement in current density values compared to factory baseline. The absorption is also increased at higher wavelengths (700 nm and above) due to the increase in surface features values (σ_{RMS}, Lc and AR) as shown in Figure 112. These features aid in good light trapping of photons with long wavelengths. A clear correlation between the roughness, aspect ratio and absorption in higher wavelengths (and hence current density) can be seen- higher the roughness and AR value, higher is the absorption in longer wavelengths (and hence higher current densities). KOH60 with the highest surface feature values has the broadest absorption curve and highest current density value. The test run sample shows a significant improvement in absorptance in the higher wavelengths compared to factory baseline due to its improved surface features. However, it is not as good as the best lab samples. This is in line with the expectations, since the test run etching conditions were limited due to thickness and machine constraints. All the GenPro simulation diagrams are shown in Appendix IX.

Texturing	Model	σ_{RMS} (nm)	Aspect Ratio (%)	J_{SC} (mA/cm^2)
No texturing	Flat	-	-	20.82
Factory baseline	Wave	28.4	5.7	22.53
Test run	Ray	233	10.26	25.15
KOH70	Ray	472.62	11.86	25.87
KOH60	Ray	669	14.32	26.02
NaOH60	Ray	594	13.58	25.88

Table 17: Current density values using GenPro4 in the nc-Si:H absorber layer for a single junction cell

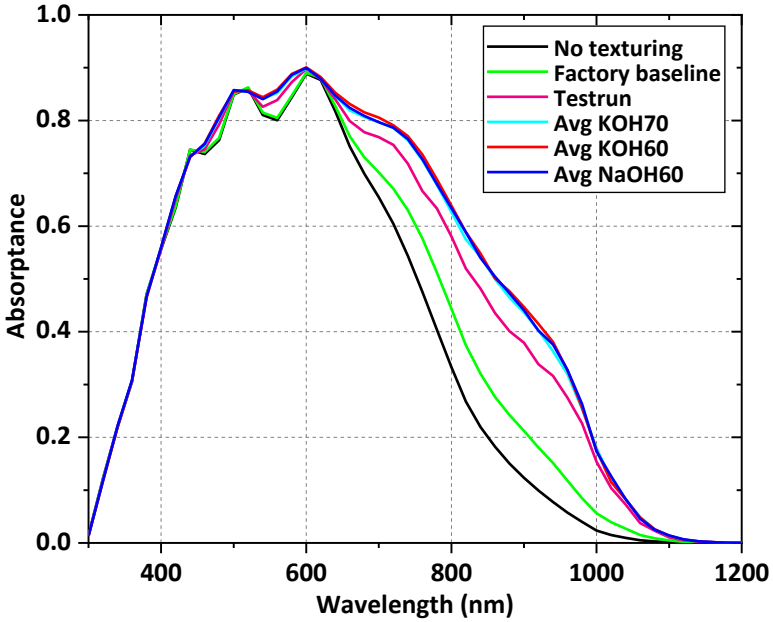

Figure 112: Absorptance curve of single junction nc-Si:H cell generated from GenPro4

4.9.2 a-Si:H/nc-Si:H tandem cell

Similar to the single junction nanocrystalline silicon cell, an a-Si:H/nc-Si:H tandem cell is simulated using GenPro. The model and layer parameters are shown in Figure 113 and Table 18 respectively.

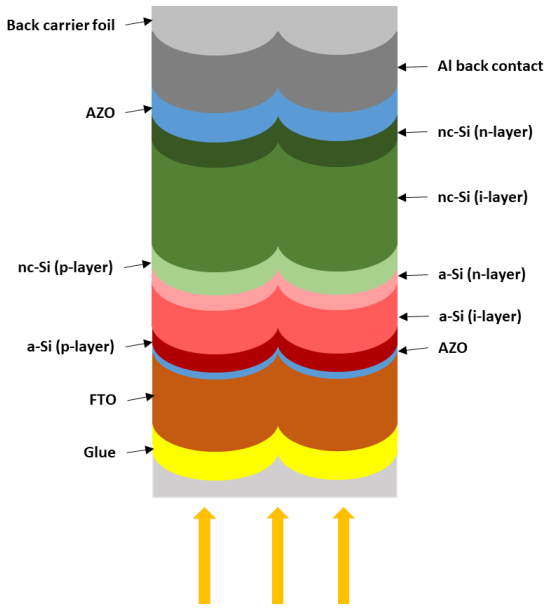

Figure 113: Model of a-Si:H/nc-Si:H tandem cell

Layer	Thickness (μm)	Lay/Coat
Front encapsulant	25	Lay
Glue	500	Lay
FTO	0.7	Coat
AZO	0.005	Coat
p-a-SiC	0.01	Coat
i-a-Si:H	0.28	Coat
n-a-SiO:H	0.01	Coat
p-nc-SiO_X:H	0.025	Coat
i-nc-Si:H	2.3	Lay
n-nc-SiO_X:H	0.025	Coat
AZO	0.08	Coat
Al back contact	0.3	Coat
Back carrier foil	125	Lay

Table 18: Parameters for a-Si:H/nc-Si:H tandem cell

Table 19 lists the current density values in the absorber layers of the tandem cell. There is a noticeable improvement in the current density values in the nc-Si:H layer. As in the case of single junction nc-Si:H cell, due to the increase in surface feature values, the best lab samples show higher absorption and good light trapping in higher wavelengths (above 700 nm) compared to flat and factory baseline textured samples, as shown in Figure 114. The sample with the highest roughness and AR, has the highest current density. It is also interesting to note that the current density in the a-Si:H top cell is not affected by the texturing of the Al foil, which is in line with the expectations.

Texturing	Model	σ_{RMS} (nm)	Aspect Ratio (%)	J_{SC} (mA/cm²) a-Si:H	J_{SC} (mA/cm²) nc-Si:H
Flat		-	-	10.05	9.88
Factory baseline	Wave	28.4	5.7	10.18	11.45
Test run	Ray	233	10.26	10.1	13.67
KOH70	Ray	472.62	11.86	10.12	14.3
KOH60	Ray	669	14.32	10.17	14.46
NaOH60	Ray	594	13.58	10.12	14.36

Table 19: Current density values using GenPro4 in an a-Si:H/nc-Si:H tandem cell

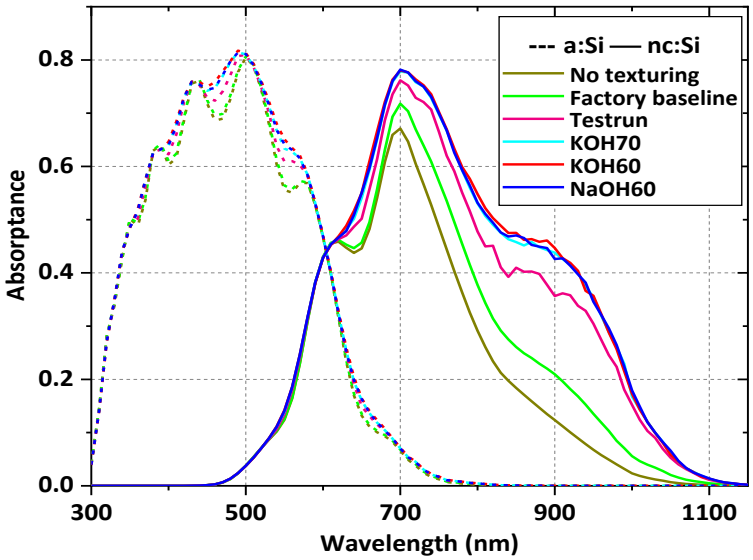

Figure 114: Absorptance curve of a-Si:H/nc-Si:H tandem cell generated from GenPro4

Compared to the factory baseline, the other samples have a lower current density in the a-Si:H cell, i.e. the first sub-cell. The factory baseline has the smallest features of all samples. It has features smaller than the wavelengths and hence scatters short wavelength light into the first sub-cell, resulting in a higher current density in the a-Si:H cell. This is also because the input texturing file to the GenPro consists of only the texturing of Al foil only, i.e. the micro crater-shaped features. The FTO is V-shaped textured which is in the range of few nanometres, which will effectively trap the low wavelengths. This can be verified from absorptance curve comparison between the sub-cells simulated using test run Al texturing and test run Al + FTO texturing as shown in Figure 115. All the interfaces here are assumed to have conformal texturing. With the Al + FTO texturing, the current density in the a-Si:H cell has increased from 10.1 mA/cm^2 to 10.74 mA/cm^2, which shows the effectiveness of trapping low wavelength light by the FTO nano-features. These measurements with FTO deposited Al samples cannot be done for the other lab samples as the facility to deposit FTO on 10*10 cm^2 foils were not available. All the GenPro simulation diagrams for the tandem cell are shown in Appendix IX.

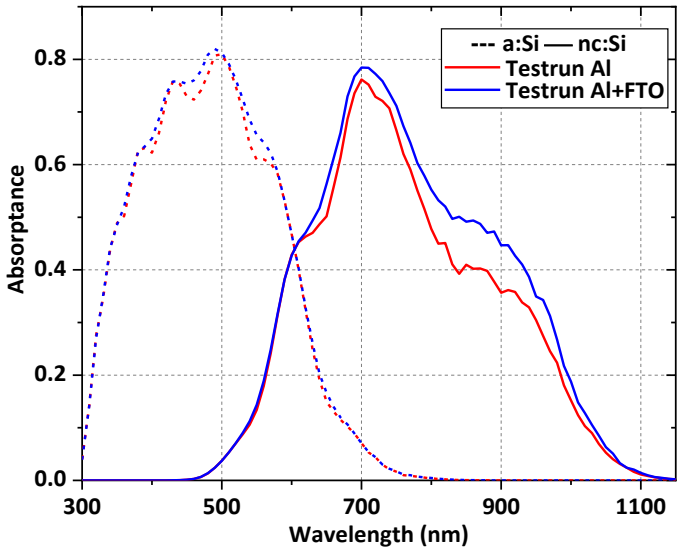

Figure 115: Absorptance curve comparison of a-Si:H/nc-Si:H tandem cell, with test run Al texturing and test run Al+FTO texturing, generated from GenPro4

5 Conclusions

The concept of Modulated Surface Texturing (MST) was successfully achieved by developing micro sized crater-shaped features on temporary Al substrate and superimposing the naturally nano sized V-shaped textured fluorine doped tin oxide (FTO) on the Al foil. The micro-craters were realized on the Al foil using alkaline based etchants such as potassium hydroxide and sodium hydroxide, as acid based etchants resulted in a sharp V-shaped texturing of the Al foil. The temperature and concentration of the etchant and the etching time are crucial in deciding the surface morphology and final thickness of the foil.

The current texturing at HyET, 'factory baseline' has the surface morphological parameters: RMS roughness (σ_{RMS}) 28.4 nm, correlation length (L_C) 497 nm, mean slope(θ_M) 12.11°, and aspect ratio (AR) 5.7%. These parameters are very small to realize MST and will not aid in high quality growth of layers, especially nc-Si:H as it is highly dependent on the substrate morphology. The nc-Si:H layer deposited on the factory baseline texturing was of low quality and did not adapt the morphology of the texturing. The targeted values are 12-14% of AR and L_C of 3-4 μm for a-Si:H/nc-Si:H tandem and a-Si:H/nc-Si:H/nc-Si:H triple junction. Best results are obtained when the features are not too deep (as it will results in cracks in the absorber layers which are detrimental to the device performance) and not too shallow (no light-trapping). Best results are also obtained when the features have L_C comparable to the thickness of the layers deposited.

KOH Etching

The kinetics of etching was studied using KOH, as it has better etching controllability compared to NaOH due to KOH being less reactive. Etch rates were studied for different concentrations (20 g/L to 100 g/L), temperatures (35, 50, 60 and 70°C) and times (0 to 4 minutes). It was realized that the 'induction period' before which the reaction starts varied based on the combination of the above parameters. The induction period was found to be high (~2 mins) for low concentrations (20 g/L) and low temperatures (35°C). As the concentration and temperature was increased, the induction period decreased, for a combination of 100g g/L and 70°C, a clear difference in the etch rate was observed before 1 minute. The thicknesses were measured, and an etching processing window was defined. For the mechanical stability for lab depositions, the foil needs to be thicker than 70 μm. AID and AFM measurements were taken on samples which fit this criterion. The sample etched at 70°C with 100 g/L (1.78M) KOH for 2 minutes ('KOH70') displayed L_C of 4.04 μm, and AR of 11. 86%, which are close to the targeted values. Compared to the factory baseline KOH70 displayed a broader AID curve and a higher reflectance haze (94.5%), which indicates higher scattering, due to its higher surface features. The TCO (AZO)/p-i-n nanocrystalline silicon layers deposited on this texturing resulted in high quality layers. The layers also followed the Al texturing, which indicates that the concept of MST can be realized in Al foils.

The texturing window showed possibility of good texturing at temperatures between 60 and 70°C. Hence, texturing was also investigated at 60°C. Thickness measurements were done for higher concentrations (80 g/L and 100 g/L) for different etching times. Foils with thicknesses higher than 70 μm were subjected to AFM and AID measurements. The best result was obtained for the sample etched at 60°C with 100g/L of KOH for 3 minutes ('KOH60'). This sample had L_C of 4.7 μm and AR of

14.32 %, close to targeted values. Compared to the factory baseline, this sample had a broader AID curve and a high reflectance haze of 94.5% which indicates a higher scattering.

NaOH Etching

Since targeted ARs were obtained with KOH at 60°C, NaOH etching was also investigated at 60°C for 57 and 71.3 g/L corresponding to 80 and 100 g/L (1.42 and 1.78M) of KOH. The process of AFM and AID was done for foils with thicknesses higher than 70 μm. Based on this data, the sample etched with 57 g/L of NaOH at 60°C for 2.5 minutes ('NaOH60') displayed values close to the targeted values: L_C of 4.36 μm and AR of 13.58%. This sample also displayed a broader AID curve and a high reflectance haze of 94.25% compared to the factory baseline due to the increase in the surface features. A a-Si:H/nc-Si:H/nc-Si:H triple junction was deposited on NaOH60. The layers deposited onto NaOH60 followed the texturing pattern, without any visible cracks and resulted in high quality materials.

Influence of additives

Polyethylene glycol 400 (PEG-400), sodium gluconate and sodium nitrate which acts as 'chelating agents' and 'surfactants' were added one by one to the etchant. These were added to increase the wettability of the Al foil resulting in uniform etching. The addition of additives clearly improved the uniformity of texturing, i.e. there were many more craters occupying the same area, and thus vey less empty un-textured spaces in the Al foil. This was confirmed through SEM imaging. This however, resulted in an increased etch rate compared to the ones without additives, and hence a thinner foil.

R2R Industrial tests

The best lab samples were adapted to define a recipe for the R2R process. The recipe was optimized in such a way that the resultant foil is thicker than 95 μm. After a series of thickness measurements and visual observations of the samples, the etching temperature was decided to be at 50°C. Considering the throughput of the etching machine, an etching time of 1.8 minutes was decided. The 'test run' sample displayed larger surface morphological features compared to the factory baseline: L_C of 2.27 μm and AR of 12.23%. The sample also scattered light more compared to the factory baseline as it had a comparatively broader AID curve and higher reflectance haze (76%). FTO was further deposited on it and the AFM and SEM measurements of the combination confirmed that the FTO adapted the morphology of the Al foil, thus successfully creating a modulated surface texture. The FTO/p-i-n tandem layers deposited on the test run also adapted the morphology of the Al foil. And there were less visible cracks as compared to the ones deposited on the factory baseline texturing. However, the morphology was not adapted in some areas where the craters were not big: this implies that the texturing is not uniform. While the test run texturing exhibited higher values of surface features over the factory baseline texturing, it is not as good as the lab samples. There is a trade-off between the required foil thickness and the surface morphology.

Optical modelling using GenPro4

The AFM data obtained for the above samples were used for optical simulations using GenPro4 to understand the effectiveness of texturing. Both nc-Si:H single junctions and a-Si:H/nc-Si:H tandem cells were simulated using this tool. There was a direct correlation between the absorbance in high wavelength region (above 600 nm) in the nanocrystalline cell and the surface morphological parameters. As the roughness, AR and thus the mean slope increased, the absorption in the higher

wavelength region increased, resulting in a higher current density. This indicates the effectives of scattering by micro sized crater shaped features on the Al foil for light trapping in the nc-Si:H sub-cell.

To sum up, various recipes were designed for the purpose of texturing Al to obtain crater-shaped features. In an ideal scenario, to develop a tandem based on a-Si:H/nc-Si:H layers with 300 nm and 3 μm thicknesses respectively, it is advised to use the recipes KOH70, KOH60 and NaOH 60 as it has values close to the targeted values. The recipe can also be used to deposit triple junctions based on a-Si:H/nc-Si:H/nc-Si:H layers as well, since these recipes have an L_C of ~4 μm. To adapt this in the R2R process, the recipes need to be optimized further as the foil thickness needs to be higher than 95 μm. While the surface features of R2R test run is higher than the factory baseline texturing, it is not as close to the targeted values as the best lab textures. The trade-off here is between the final thickness of the foil and the targeted surface morphology. While the targeted morphology can be achieved by increased temperatures and time, it will result in a foil which is less than 95 μm thick. However, maintaining 95 μm thickness from an initial thickness of 110 μm will not result the best texturing. This can be solved by using a thicker foil. However, this will also be constrained by the mechanical limitations of the R2R machines. Another solution is to induce single-sided texturing where one side of the Al foil is coated/covered by an etch resistant material. This will ensure more controllability of the etching and will limit the etch rate. This also, brings in an additional processing step in the R2R line which can increase the cost. The best possible option in the current scenario would be to raise the R2R temperature from 50 to 60°C. This will result in a higher AR and higher L_C compared to the current test run sample as well as a resultant foil which is thicker than 95 μm.

6 References

[1] "RENEWABLES 2019 GLOBAL STATUS REPORT," Paris, 2019.

[2] "Global warming," March 2020. [Online]. Available: https://en.wikipedia.org/wiki/Global_warming#Observed_temperature_rise. [Accessed March 31 2020].

[3] A. H. Smets, K. Jäger, O. Isabella, R. A. van Swaaij and M. Zeman, Solar Energy The Physics and Engineering of Photovoltaic Conversion Technologies and Systems, England: UIT Cambridge Ltf, 2016.

[4] IRENA (2019), "Renewable capacity statistics 2019," International Renewable Energy Agency (IRENA), Abu Dhabi.

[5] R. Folkson, Alternative Fuels and Advanced Vehicle Technologies for Improved Environmental Performance, Woodhead publishing, 2014, pp. 1-15.

[6] HyET Solar, "HyET Soalr Flexible light weight solar modules Production Process," 2018. [Online]. Available: https://www.hyetsolar.com/production-process/. [Accessed 30 September 2019].

[7] E. Spans, "Optimisation of a-Si/nc-Si tandem solar cell on aluminium flexible substrate," 2020.

[8] H. Tan, E. Moulin, F. Tong Si, J.-W. Schüttauf, M. Stuckelberger, O. Isabella, F.-J. Haug, C. Ballif, M. Zeman and A. H. M. Smets, "Highly transparent modulated surface textured front electrodes for high-efficiency multijunction thin-film silicon solar cells," *PROGRESS IN PHOTOVOLTAICS: RESEARCH AND APPLICATIONS,* no. 23, p. 949–963, 2015.

[9] O. Isabella, J. Krč and M. Zeman, "Modulated surface textures for enhanced light trapping in thin-film silicon solar cells," *APPLIED PHYSICS LETTERS,* vol. 97, 2010.

[10] Y. Nasuno, M. Kondo and A. Matsuda, "Effects of Substrate Surface Morphology on Microcrystalline Silicon Solar Cells," *Japanese Journal of Applied Physics,* vol. 40, 2001.

[11] H. Tan, E. Psomadaki, O. Isabella, M. Fischer, P. Babal, R. Vasudevan, M. Zeman and A. H. M. Smets, "Micro-textures for efficient light trapping and improved electrical performance in thin-film nanocrystalline silicon solar cells," *Applied Physics Letters,* vol. 103, 2013.

[12] H. Sai, K. Maejima, T. Matsui, T. Koida, M. Kondo, S. Nakao, Y. Takeuchi, H. Katayama and I. Yoshida, "High-efficiency microcrystalline silicon solar cells on honeycomb textured substrates grown with high-rate VHF plasma-enhanced chemical vapor deposition," *Japanese Journal of Applied Physics,* vol. 54, 2015.

[13] D. Y. Kim, R. Santbergen, K. Jäger, M. Sever, J. Krč, M. Topič, S. Hänni, C. Zhang, A. Heidt, M. Meier, R. A. C. M. M. v. Swaaij and M. Zeman, "Effect of Substrate Morphology Slope

Distributions on Light Scattering, nc-Si:H Film Growth, and Solar Cell Performance," *ACS Applied Materials & Interfaces,* vol. 6, p. 22061−22068, 2014.

[14] T. Matsui, K. Maejima, A. Bidiville, H. Sai, T. Koida, T. Suezaki, M. Matsumoto, K. Saito, I. Yoshida and M. Kondo, "High-efficiency thin-film silicon solar cells realized by integrating stable a-Si:H absorbers to improve device design," *Japanese Journal of Applied Physics,* vol. 54, pp. 08KB10-1-08KB10-4, 2015.

[15] H. B. Li, R. H. Franken, J. K. Rath and R. E. Schropp, "Structural defects caused by a rough substrate and their influence on the performance of hydrogenated nano-crystalline silicon n–i–p solar cells," *Solar Energy Materials and Solar Cells,* vol. 93, no. 3, pp. 338-349, 2009.

[16] M. L. Addonizio and A. Antonaia, "Surface morphology and light scattering properties of plasma etched ZnO:B films grown by LP-MOCVD for silicon thin film solar cells," *Thin Solid Films,* vol. 518, no. 4, pp. 1026-1031, 2009.

[17] H. Sakai, T. Yoshida, T. Hama and Y. Ichikawa, "Effects of Surface Morphology of Transparent Electrode on the Open-Circuit Voltage in a-Si:H Solar Cells," *Japanese Journal of Applied Physics,* vol. 29, no. 4, 1990.

[18] G. Yang, "High-efficient n-i-p thin-film silicon solar cells," Guangtao Yang, Delft, 2015.

[19] A. A. Bayod-Rújula, Solar Hydrogen Production-Processes, Systems and Technologies, Academic PRess, 2019, pp. 237-295.

[20] NCERT, Physics Textbook for Class XII, vol. II, 2016.

[21] D. A. Neaman, Semiconductor Physics and Devices Basic Principles, 4 ed., New York: McGraw-Hill, 2012.

[22] Wikipedia, the free encyclopedia, "Reflection (physics)," 10 January 2020. [Online]. Available: https://en.wikipedia.org/wiki/Reflection_(physics). [Accessed 20 April 2020].

[23] G. Waldman, "Chapter 5 Polarization," in *Introduction to Light: The Physics of Light, Vision, and Color*, Dover Publications Inc., 2002, p. 67.

[24] The Editors of Encyclopaedia Britannica, "Total internal reflection, Encyclopedia Britannica," 24 March 2020. [Online]. Available: https://www.britannica.com/science/total-internal-reflection. [Accessed 20 April 2020].

[25] O. Stenzel, "Planar Interfaces," in *The Physics of Thin Film Optical Spectra, An Introduction*, 2nd ed., vol. 44, Springer International Publishing.

[26] GianniG46. [Online]. Available: https://commons.wikimedia.org/w/index.php?curid=11902338. [Accessed 21 April 2020].

[27] A. K. RoyChoudhury, "Colour and appearance attributes," in *Principles of Colour and Appearance Measurement*, Woodhead Publishing, 2014, pp. 103-143.

[28] A. Wang and Y. Xuan, "A detailed study on loss processes in solar cells," *Energy,* vol. 144, pp. 490-500, February 2018.

[29] J. Poortmans and V. Arkhipov, Eds., in *Thin Film Solar Cells Fabrication, Characterization and Applications*, John Wiley & Sons Ltd, 2006.

[30] R. E. Schropp and M. Zeman, "Deposition of Amorphous and Microcrystalline Silicon," in *Amorphous and Microcrystalline Silicon Solar Cells: Modeling, Materials and Device Technology*, Kluwer Academic Publishers, pp. 14-15.

[31] R. Schropp, C. Van der Werf, M. Zeman, M. Van de Sanden, C. Spee, E. Middleman, L. de Jonge-Meschaninova, P. Peters, A. Van der Zijden, M. Besselink, R. Severens, J. Winkeler and G. Jongerden, "Novel Amorphous Silicon Solar Cell using a Manufacturing Procedure with a Temporary Superstrate," in *MRS Proceedings*, 1999.

[32] Wikipedia, the free encyclopedia, "Rayleigh scattering From Wikipedia, the free encyclopedia," 6 April 2020. [Online]. Available: https://en.wikipedia.org/wiki/Rayleigh_scattering#Small_size_parameter_approximation. [Accessed 20 April 2020].

[33] A. H. M. Smets, *Module 7 – Light management 2.*

[34] K. Jäger, "On the Scalar Scattering Theory for Thin-Film Solar Cells," 2012.

[35] Wikipedia, the free encyclopedia, "Light scattering by particles, From Wikipedia, the free encyclopedia," 16 December 2019. [Online]. Available: https://en.wikipedia.org/wiki/Light_scattering_by_particles#Geometric_optics_(ray-tracing). [Accessed 20 April 2020].

[36] E. Yablonovich and G. Cody, "Intensity Enhancement in Textured Optical Sheets," *IEEE TRANSACTIONS ON ELECTRON DEVICES,* pp. 300-305, February 1982.

[37] N.-T. Nguyen, "Chapter 4 - Fabrication technologies," in *Micromixers- Fundamentals, Design and Fabrication, A volume in Micro and Nano Technologies*, 2nd ed., 2012.

[38] M. Tilli, M. Paulasto-Krockel, M. Petzold, H. Theuss, T. Motooka and V. Lindroos, Eds., "Chapter 16 - Deep reactive ion etching," in *Handbook of Silicon Based MEMS Materials and Technologies- A volume in Micro and Nano Technologies*, 3rd ed., 2020, pp. 417-446.

[39] R. Ghodssi and P. Lin, Eds., MEMS Materials and Processes Handbook, 2011.

[40] "UF Chemical Engineering- Unit Operations Laboratory," [Online]. Available: http://ww2.che.ufl.edu/unit-ops-lab/experiments/semiconductors/etching/Etching-theory.pdf. [Accessed 07 May 2020].

[41] J. X. Zhang and K. Hoshino, in *Molecular Sensors and Nanodevices- Principles, Designs and Applications in Biomedical Engineering*, 2nd ed., 2019Chapter 2 - Fundamentals of nano/microfabrication and scale effect, pp. 43-111.

[42] M. Kadlecková, A. Minarík, P. Smolka, A. Mrácek, E. Wrzecionko, L. Novák, L. Musilová and R. Gajdošík, "Preparation of Textured Surfaces on Aluminum-Alloy Substrates," *MDPI Materials,* 2019.

[43] M. H. M. Zaki, Y. Mohd and N. N. C. Isa, "Surface pre-treatment of aluminium by cleaning, chemical ething and conversion coating," in *ADVANCED MATERIALS FOR SUSTAINABILITY AND GROWTH: Proceedings of the 3rd Advanced Materials Conference 2016 (3rd AMC 2016)*, 2017.

[44] V. Burokas, A. Martushene, G. Bikul'chyus and A. Ruchinskene, "Aluminum alloy etching in phosphoric acid solutions," *Russian Journal of Applied Chemistry,* vol. 82, no. 10, pp. 1835-1839, 2009.

[45] L. Chesterfield, "PF Products finishing, Smut and Desmutting," [Online]. Available: https://www.pfonline.com/articles/smut-and-desmutting. [Accessed 17 May 2020].

[46] J. Wang, "Aluminium surface cleaning – a brief overview," Innoval technology part of Daniel group, [Online]. Available: https://www.innovaltec.com/aluminium-surface-cleaning-overview-blog/. [Accessed 17 May 2020].

[47] J. Davis, Ed., Aluminum and Aluminum Alloys ASM Speciality Handbook.

[48] L. Zhao, "Enhancement of Light Trapping in Thin Film Silicon Solar Cells," Delft, 2009.

[49] S. B. Kaemmer, "Introduction to Bruker's ScanAsyst and PeakForce Tapping AFM Technology," Bruker Corporation, 2011. [Online]. Available: https://www.bruker.com/fileadmin/user_upload/8-PDF-Docs/SurfaceAnalysis/AFM/ApplicationNotes/Introduction_to_Brukers_ScanAsyst_and_PeakForce_Tapping_Atomic_Force_Microscopy_Technology_AFM_AN133.pdf. [Accessed 18 May 2020].

[50] Wikipedia, the free encyclopedia, "Atomic force microscopy From Wikipedia, the free encyclopedia," May 2020. [Online]. Available: https://en.wikipedia.org/wiki/Atomic_force_microscopy#Imaging_modes. [Accessed 17 May 2020].

[51] R. Santbergen, "Manual for solar cell optical simulation software: GENPRO4," 2018.

[52] H. E. Bennett and J. O. Porteus, "Relation Between Surface Roughness and Specular Reflectance at Normal Incidence," *Journal of the Optical Society of America,* vol. 51, no. 2, pp. 123-129, 1961.

[53] D. Rajagopal, "Characterization of texturing for flexible thin film solar cells," 2019.

[54] C. B. Porciúncula, N. R. Marcilio, I. C. Tessaro and M. Gerchmann, "PRODUCTION OF HYDROGEN IN THE REACTION BETWEEN ALUMINUM AND WATER IN THE PRESENCE OF NaOH AND KOH," *Brazilian Journal of Chemical Engineering,* vol. 29, no. 02, pp. 337-348, 2011.

[55] I. Halaša and M. Miadoková, “Influence of alkali metal hydroxides on the reaction of aluminum monocrystals,” *Chemical Papers,* vol. 44, no. 4, p. 543–555, 1990.

[56] I. Boukerche, S. Djerad, L. Benmansour, L. Tifouti and K. Saleh, “Degradability of aluminum in acidic and alkaline solutions,” *Corrosion Science,* pp. 343-352, 2014.

[57] V. N. Alviani, P. Setiani, M. Uno, M. Oba, N. Hirano, N. Watanabe, N. Tsuchiya and H. Saishu, “Mechanisms and possible applications of the AleH2O reaction under extreme pH and low hydrothermal temperatures,” *International Journal of Hydrogen Energy,* vol. 44, no. 57, pp. 29903-29921, 2019.

[58] R. F. Hunter and P. Hohn, “Alkaline etching of aluminum with matte finish and low waste capability”. Patent EP0565544B1.

[59] H. V. Smith.Patent United States Patent 3802973, 9 April 1974.

[60] Wikipedia, the free encyclopedia, “Chelation,” [Online]. Available: https://en.wikipedia.org/wiki/Chelation. [Accessed 29 June 2020].

[61] Wikipedia, the free encyclopedia, “Surfactant,” [Online]. Available: https://en.wikipedia.org/wiki/Surfactant. [Accessed 29 June 2020].

[62] B. Tang and K. Sato, “Advanced Surfactant-Modified Wet Anisotropic Etching,” in *Microelectromechanical Systems and Devices*, 2011.

[63] B. Mills, “Wikipedia,” 10 September 2007. [Online]. Available: https://commons.wikimedia.org/wiki/File:Silicon-unit-cell-3D-balls.png. [Accessed 9 April 2020].

7 Appendix

7.1 Appendix I

KOH etching at 35°C					
Time (min)	**20 g/L**	**40 g/L**	**60 g/L**	**80 g/L**	**100 g/L**
0	107	107	107	107	107
1	107	107	107	107	107
2	107	107	107	107	106.75
3	106	105.25	105	104.5	103
4	106	105	103.5	102.75	102

Appendix 7.1: Thickness of Al foil in μm for KOH etching at 35°C

KOH etching at 50°C					
Time (min)	**20 g/L**	**40 g/L**	**60 g/L**	**80 g/L**	**100 g/L**
0	107	107	107	107	107
1	107	107	107	106.5	103.5
2	106.5	104.75	103.5	103	96.75
3	103.75	100.5	97.75	95	90
4	101.25	97.75	93.75	92	84.5

Appendix 7.2: Thickness of Al foil in μm for KOH etching at 50°C

KOH etching at 70°C					
Time (min)	**20 g/L**	**40 g/L**	**60 g/L**	**80 g/L**	**100 g/L**
0	107	107	107	107	107
1	107	107	107	107	107
2	107	107	107	107	106.75
3	106	105.25	105	104.5	103
4	106	105	103.5	102.75	102

Appendix 7.3: Thickness of Al foil in μm for KOH etching at 70°C

7.2 Appendix II

KOH 100 g/L, 70°C, 2min					
Sample number	**1**	**2**	**3**	**Average**	**Error**
Sample size (μm X μm)	40*40	40*40	40*40		
2D correlation length (Lc) (nm)	4450	4620	3062	4044	854.67
RMS roughness (σ_{RMS}) (nm)	438	570	410	472.67	85.45
Average Roughness (σ_A) (nm)	345	443	306		
Aspect ratio (σ_{RMS}/Lc) (%)	9.84	12.34	13.39	11.86	1.82

Appendix 7.4: σ_{RMS}, Lc and AR values of KOH etched sample at 70°C, 100 g/L for 2m

KOH 80 g/L, 70°C, 2min				
Sample number	**1**	**2**	**Average**	**Error**
Sample size (µm X µm)	40*40	40*40		
2D correlation length (Lc)(nm)	3570	3328	3449	171.11
RMS roughness (σ_{RMS}) (nm)	367	426	396.5	41.72
Average Roughness (σ_A) (nm)	279	338		
Aspect ratio (σ_{RMS}/Lc) (%)	10.28	12.80	11.54	1.78

Appendix 7.5: σ_{RMS}, Lc and AR values of KOH etched sample at 70°C, 80 g/L for 2m

KOH 60 g/L, 70°C, 2min	
Sample number	**1**
Sample size (µm X µm)	40*40
2D correlation length (Lc)(nm)	3225
RMS roughness (σ_{RMS}) (nm)	326
Average Roughness (σ_A) (nm)	263
Aspect ratio (σ_{RMS}/Lc) (%)	10.11

Appendix 7.6: σ_{RMS}, Lc and AR values of KOH etched sample at 70°C, 60 g/L for 2m

7.3 Appendix III

KOH 80 g/L, 60°C, 2min						
Sample number	**1**	**2**	**3**	**4**	**Average**	**Error**
Sample size (µm X µm)	40*40	40*40	40*40	40*40		
2D correlation length (Lc)(nm)	3600	4700	4390	4310	4250	464.83
RMS roughness (σ_{RMS}) (nm)	408	458	475	495	459	37.21
Aspect ratio (σ_{RMS}/Lc) (%)	11.33	9.74	10.82	11.48	10.85	0.79

Appendix 7.7: σ_{RMS}, Lc and AR values of KOH etched sample at 60°C, 80 g/L for 2m

KOH 80 g/L, 60°C, 2.5min					
Sample number	**1**	**2**	**3**	**Average**	**Error**
Sample size (µm X µm)	40*40	40*40	50*50		
2D correlation length (Lc)(nm)	4105	3679	4166	3983.33	265.32
RMS roughness (σ_{RMS}) (nm)	565	405	494	488.00	80.17
Aspect ratio (σ_{RMS}/Lc)	13.76	11.01	11.86	12.21	1.41

Appendix 7.8: σ_{RMS}, Lc and AR values of KOH etched sample at 60°C, 80 g/L for 2.5m

KOH 80 g/L, 60°C, 3min					
Sample number	**1**	**2**	**3**	**Average**	**Error**
Sample size (µm X µm)	50*50	40*40	40*40		
2D correlation length (Lc)(nm)	3930	3875	4071	3958.67	101.10
RMS roughness (σ_{RMS}) (nm)	523	512	535	523.33	11.50
Aspect ratio (σ_{RMS}/Lc) (%)	13.31	13.21	13.14	13.22	0.08

Appendix 7.9: σ_{RMS}, Lc and AR values of KOH etched sample at 60°C, 80 g/L for 3m

KOH 100 g/L, 60°C, 2min					
Sample number	**1**	**2**	**3**	**Average**	**Error**
Sample size (µm X µm)	40*40	40*40	40*40	Average	Std dev
2D correlation length (Lc)(nm)	4094	3687	3896	3892.33	203.52
RMS roughness (σ_{RMS}) (nm)	360	318	472	383.33	79.61
Aspect ratio (σ_{RMS}/Lc) (%)	8.79	8.62	12.11	9.84	1.97

Appendix 7.10: σ_{RMS}, Lc and AR values of KOH etched sample at 60°C, 100 g/L for 2m

KOH 100 g/L, 60°C, 2.5min						
Sample number	**1**	**2**	**3**	**4**	**Average**	**Error**
Sample size (µm X µm)	40*40	40*40	40*40	30*30		
2D correlation length (Lc)(nm)	4410	4590	4720	3480	4300	561.25
RMS roughness (σ_{RMS}) (nm)	414	623	460	465	490.5	91.27
Aspect ratio (σ_{RMS}/Lc) (%)	9.39	13.57	9.75	13.36	11.52	2.26

Appendix 7.11: σ_{RMS}, Lc and AR values of KOH etched sample at 60°C, 100 g/L for 2.5m

KOH 100 g/L, 60°C, 3min					
Sample number	**1**	**2**	**3**	**Average**	**Error**
Sample size (µm X µm)	40*40	40*40	40*40		
2D correlation length (Lc)(nm)	5049	4818	4143	4670.00	470.78
RMS roughness (σ_{RMS}) (nm)	793	612	603	669.33	107.19
Aspect ratio (σ_{RMS}/Lc)	15.71	12.70	14.55	14.32	1.52

Appendix 7.12: σ_{RMS}, Lc and AR values of KOH etched sample at 60°C, 100 g/L for 3m

7.4 Appendix IV

NaOH 57 g/L, 60°C, 2min					
Sample number	**1**	**2**	**3**	**Average**	**Error**
Sample size (µm X µm)	40*40	40*40	40*40		
2D correlation length (Lc)(nm)	3660	4030	5020	4,236.67	703.16
RMS roughness (σ_{RMS}) (nm)	409	572	658	546.33	126.47
Aspect ratio (σ_{RMS}/Lc) (%)	11.17	14.19	13.11	12.83	1.53

Appendix 7.13: σ_{RMS}, Lc and AR values of NaOH etched sample at 60°C, 57 g/L for 2m

NaOH 57 g/L, 60°C, 2.5min					
Sample number	**1**	**2**	**3**	**Average**	**Error**
Sample size (µm X µm)	40*40	40*40	40*40		
2D correlation length (Lc)(nm)	4076	5333	3662	4,357.00	870.22
RMS roughness (σ_{RMS}) (nm)	613	728	441	594.00	144.44
Aspect ratio (σ_{RMS}/Lc) (%)	15.04	13.65	12.04	13.58	1.5

Appendix 7.14: σ_{RMS}, Lc and AR values of NaOH etched sample at 60°C, 57 g/L for 2.5m

NaOH 57 g/L, 60°C, 3min					
Sample number	**1**	**2**	**3**	**Average**	**Error**
Sample size (μm X μm)	40*40	40*40	40*40		
2D correlation length (Lc)(nm)	3817	4105	3608	3,843.33	249.54
RMS roughness (σ_{RMS}) (nm)	516	542	390	482.67	81.30
Aspect ratio (σ_{RMS}/Lc) (%)	13.52	13.20	10.81	12.51	1.48

Appendix 7.15: σ_{RMS}, Lc and AR values of NaOH etched sample at 60°C, 57 g/L for 3m

NaOH 71 g/L, 60°C, 2min					
Sample number	**1**	**2**	**3**	**Average**	**Error**
Sample size (μm X μm)	40*40	40*40	40*40		
2D correlation length (Lc)(nm)	3922	4069	4863	4,284.67	506.22
RMS roughness (σ_{RMS}) (nm)	501	488	520	503.00	16.09
Aspect ratio (σ_{RMS}/Lc) (%)	12.77	11.99	10.69	11.82	1.05

Appendix 7.16: σ_{RMS}, Lc and AR values of NaOH etched sample at 60°C, 71 g/L for 2m

NaOH 71 g/L, 60°C, 2.5min					
Sample number	**1**	**2**	**3**	**Average**	**Error**
Sample size (μm X μm)	40*40	40*40	40*40		
2D correlation length (Lc)(nm)	4072	5012	3294	4,126.00	860.27
RMS roughness (σ_{RMS}) (nm)	490	729	407	542.00	167.18
Aspect ratio (σ_{RMS}/Lc) (%)	12.03	14.55	12.36	12.98	1.37

Appendix 7.17: σ_{RMS}, Lc and AR values of NaOH etched sample at 60°C, 71 g/L for 2.5m

NaOH 71 g/L, 60°C, 3min					
Sample number	**1**	**2**	**3**	**Average**	**Error**
Sample size (μm X μm)	40*40	40*40	40*40		
2D correlation length (Lc)(nm)	4094	4143	4586	4,274.33	271.02
RMS roughness (σ_{RMS}) (nm)	359	420	399	392.67	30.99
Aspect ratio (σ_{RMS}/Lc) (%)	8.77	10.14	8.70	9.20	0.81

Appendix 7.18: σ_{RMS}, Lc and AR values of NaOH etched sample at 60°C, 71 g/L for 3m

7.5 Appendix V

AZO: KOH 50°C					
Sample number	**1**	**2**	**3**	**Average**	**Error**
Sample size (μm X μm)	40*40	40*40	40*40		
2D correlation length (Lc)(nm)	4697	2824	2510	3343.667	965.498
RMS roughness (σ_{RMS}) (nm)	600	655	197	484	204.178
Aspect ratio (σ_{RMS}/Lc) (%)	12.77	23.19	7.85	14.61	6.39

Appendix 7.19: σ_{RMS}, Lc and AR values of AZO on Al sample etched with 85 g/L KOH at 50°C, for 3m

AZO: KOH 70°C					
Sample number	**1**	**2**	**3**	**Average**	**Error**
Sample size (μm X μm)	40*40	40*40	40*40		
2D correlation length (Lc)(nm)	5450	3800	4720	4656.67	675.09
RMS roughness (σ_{RMS}) (nm)	443	336	498	425.67	67.26
Aspect ratio (σ_{RMS}/Lc) (%)	8.13	8.84	10.55	9.17	1.02

Appendix 7.20: : σ_{RMS}, Lc and AR values of AZO on Al sample etched with 85 g/L KOH at 70°C, for 3m

7.6 Appendix VI

60deg, 57 g/L NaOH+ sodium nitrate						
Minute	**Thickness**				**Average**	**Error**
2	77.8	78.4	78.4	78	78.15	0.26
2.5	69	69.6	69.1	69.1	69.23	0.26
3	61.7	62.4	61.9	61.7	62	0.29

Appendix 7.21: Foil thickness (in μm) measurement of NaOH 57 g/L, 60°C, with sodium nitrate

60deg, 57g/L NaOH+ sodium gluconate						
Minute	**Thickness**				**Average**	**Error**
2	82.2	80	79.3	83.2	81.175	1.58489
2.5	72.7	73.6	75.5	71.9	73.93333	1.167143
3	67.5	66.3	65.4		66.4	0.860233

Appendix 7.22: Foil thickness (in μm) measurement of NaOH 57 g/L, 60°C, with sodium gluconate

60deg, 57 g/L NaOH+ PEG400						
Minute	**Thickness**				**Average**	**Error**
2	82	81.2	81.4	81.8	81.6	0.32
2.5	72	73.2	72.4		72.53	0.49

Appendix 7.23: Foil thickness (in μm) measurement of NaOH 57 g/L, 60°C, with PEG400

60deg, 57 g/L NaOH+ sodium gluconate +PEG400						
Minute	**Thickness**			**Thickness**	**Average**	**Error**
2	80	81.4	79.4	79.6	80.1	0.78
2.5	69.9	69	70.2		69.7	0.51

Appendix 7.24: Foil thickness (in μm) measurement of NaOH 57 g/L, 60°C, with sodium gluconate and PEG400

60deg, 57 g/L NaOH+ sodium nitrate + sodium gluconate + PEG400						
Minute	**Thickness**				**Average**	**Error**
2	73.5	72.1	71.9	71.6	72.275	0.73
2.5	69.6	67.1	67.1	67	67.7	1.09

Appendix 7.25: Foil thickness (in μm) measurement of NaOH 57 g/L, 60°C, with all three additives

7.7 Appendix VII

NaOH 57 g/L, 60°C, 2min, PEG + sodium gluconate				
Sample number	**1**	**2**	**Average**	**Error**
Sample size (μm X μm)	40*40	40*40		
2D correlation length (Lc)(nm)	3353	3692	3,522.50	239.71
RMS roughness (σ_{RMS}) (nm)	391	410	400.50	13.44

Appendix 7.26: σ_{RMS} and Lc values of NaOH 57 g/L 60°C, 2m with PEG and sodium gluconate

NaOH 57 g/L, 60°C, 2.5min, PEG + sodium gluconate					
Sample number	**1**	**2**	**3**	**Average**	**Error**
Sample size (μm X μm)	40*40	40*40	40*40		
2D correlation length (Lc)(nm)	3695	4860	4190	4,248.33	584.69
RMS roughness (σ_{RMS}) (nm)	429	462	600	497.00	90.71

Appendix 7.27: σ_{RMS} and Lc values of NaOH 57 g/L 60°C, 2.5m with PEG and sodium gluconate

7.8 Appendix VIII

KOH 100 g/L, 70°C, 2min-100 rpm					
Sample number	**1**	**2**	**3**	**Average**	**Error**
Sample size (μm X μm)	40*40	40*40	40*40		
2D correlation length (Lc)(nm)	4450	4620	3060	4043.33	855.82
RMS roughness (σ_{RMS}) (nm)	438	570	410	472.67	85.45

Appendix 7.28: σ_{RMS} and Lc values of KOH 100 g/L 70°C, 2m at 100 RPM

KOH 100 g/L, 70°C, 2min-200 rpm				
Sample number	**1**	**2**	**Average**	**Error**
Sample size (μm X μm)	70*70	40*40		
2D correlation length (Lc)(nm)	4990	4010	4500	692.96
RMS roughness (σ_{RMS}) (nm)	676	433	554.5	171.83

Appendix 7.29: σ_{RMS} and Lc values of KOH 100 g/L 70°C, 2m at 200 RPM

KOH 100 g/L, 70°C, 2min-600 rpm	
Sample number	1
Sample size (μm X μm)	70*70
2D correlation length (Lc)(nm)	6670
RMS roughness (σ_{RMS}) (nm)	682

Appendix 7.30: σ_{RMS} and Lc values of KOH 100 g/L 70°C, 2m at 600 RPM

7.9 Appendix IX

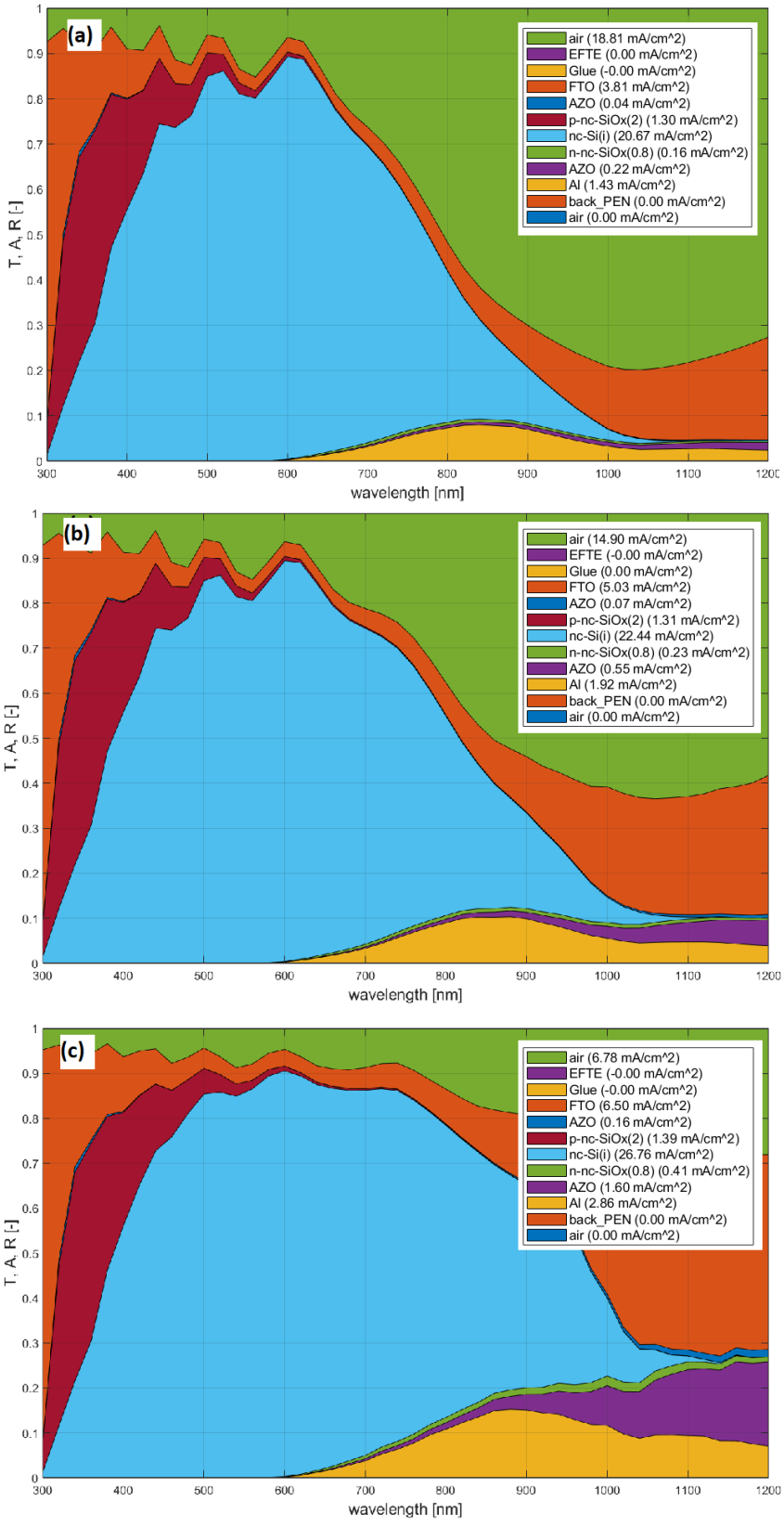

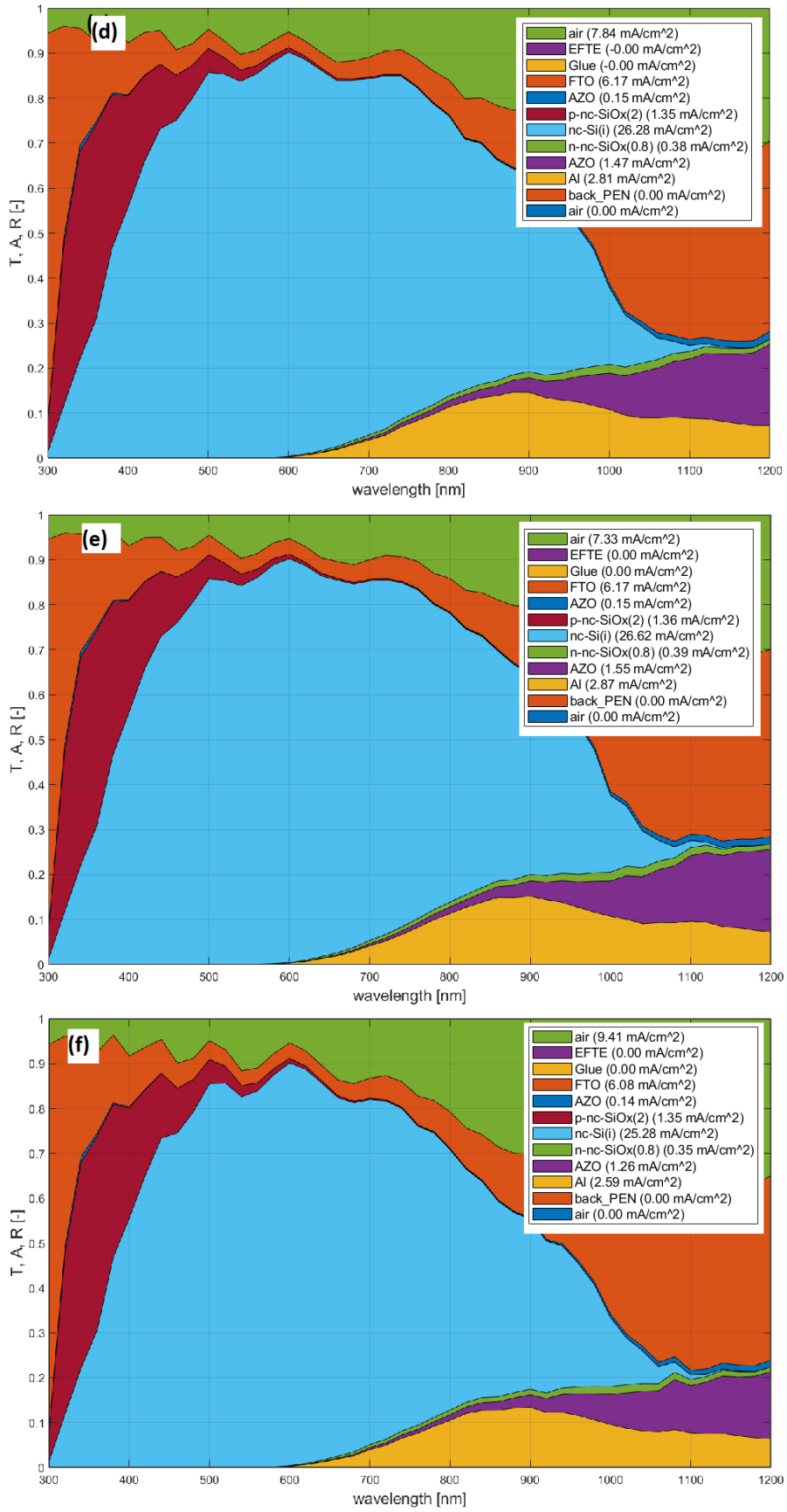

Appendix 7.31: GenPro simulation results for nc-Si:H single junction cell with (a) no texturing (b) factory baseline (c) KOH60 (d) KOH70 (e) NaOH70 (f) test run

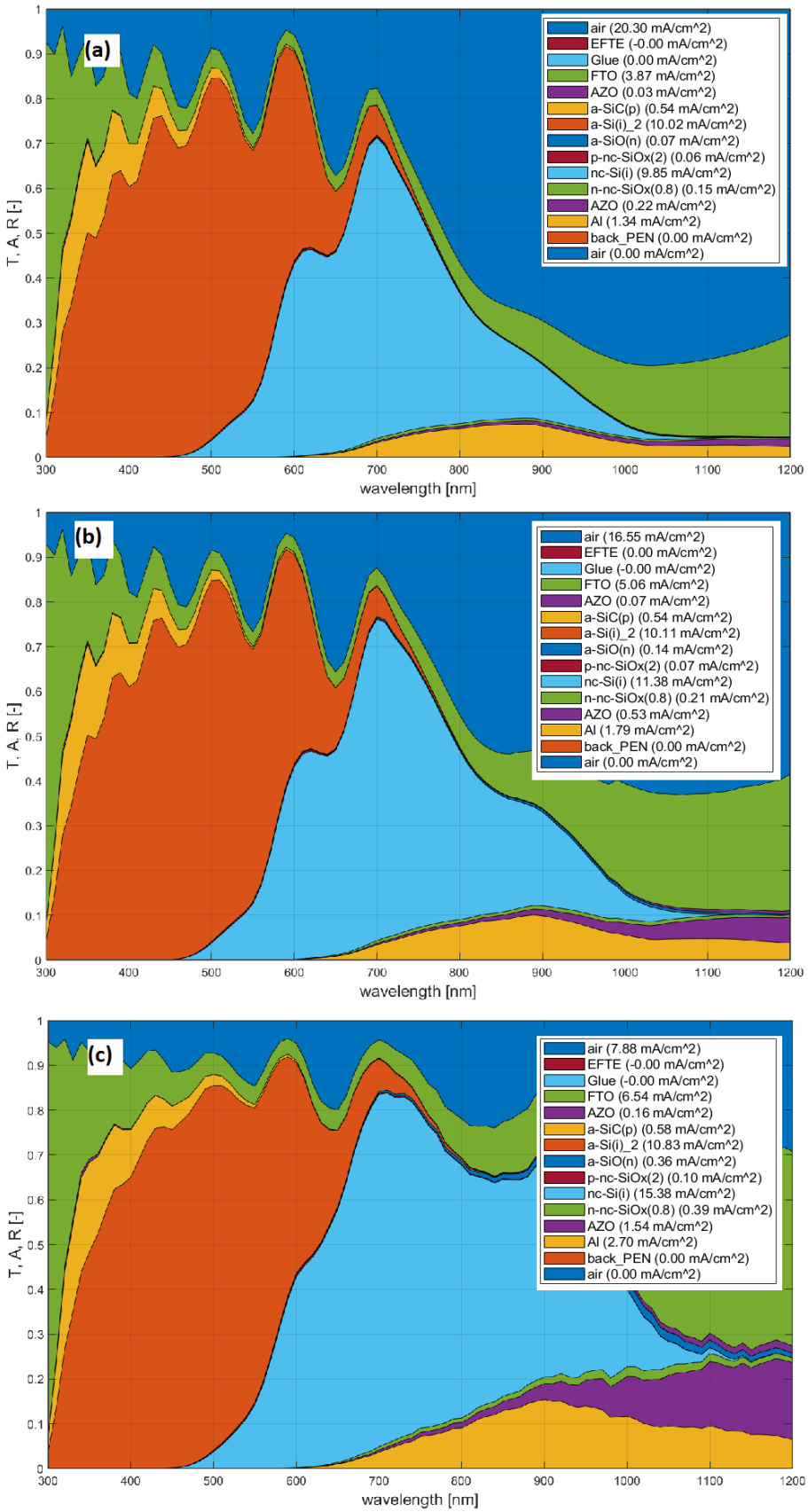
(a)
air (20.30 mA/cm^2)
EFTE (-0.00 mA/cm^2)
Glue (0.00 mA/cm^2)
FTO (3.87 mA/cm^2)
AZO (0.03 mA/cm^2)
a-SiC(p) (0.54 mA/cm^2)
a-Si(i)_2 (10.02 mA/cm^2)
a-SiO(n) (0.07 mA/cm^2)
p-nc-SiOx(2) (0.06 mA/cm^2)
nc-Si(i) (9.85 mA/cm^2)
n-nc-SiOx(0.8) (0.15 mA/cm^2)
AZO (0.22 mA/cm^2)
Al (1.34 mA/cm^2)
back_PEN (0.00 mA/cm^2)
air (0.00 mA/cm^2)
T, A, R [-]
wavelength [nm]
(b)
air (16.55 mA/cm^2)
EFTE (0.00 mA/cm^2)
Glue (-0.00 mA/cm^2)
FTO (5.06 mA/cm^2)
AZO (0.07 mA/cm^2)
a-SiC(p) (0.54 mA/cm^2)
a-Si(i)_2 (10.11 mA/cm^2)
a-SiO(n) (0.14 mA/cm^2)
p-nc-SiOx(2) (0.07 mA/cm^2)
nc-Si(i) (11.38 mA/cm^2)
n-nc-SiOx(0.8) (0.21 mA/cm^2)
AZO (0.53 mA/cm^2)
Al (1.79 mA/cm^2)
back_PEN (0.00 mA/cm^2)
air (0.00 mA/cm^2)
T, A, R [-]
wavelength [nm]
(c)
air (7.88 mA/cm^2)
EFTE (-0.00 mA/cm^2)
Glue (-0.00 mA/cm^2)
FTO (6.54 mA/cm^2)
AZO (0.16 mA/cm^2)
a-SiC(p) (0.58 mA/cm^2)
a-Si(i)_2 (10.83 mA/cm^2)
a-SiO(n) (0.36 mA/cm^2)
p-nc-SiOx(2) (0.10 mA/cm^2)
nc-Si(i) (15.38 mA/cm^2)
n-nc-SiOx(0.8) (0.39 mA/cm^2)
AZO (1.54 mA/cm^2)
Al (2.70 mA/cm^2)
back_PEN (0.00 mA/cm^2)
air (0.00 mA/cm^2)
T, A, R [-]
wavelength [nm]

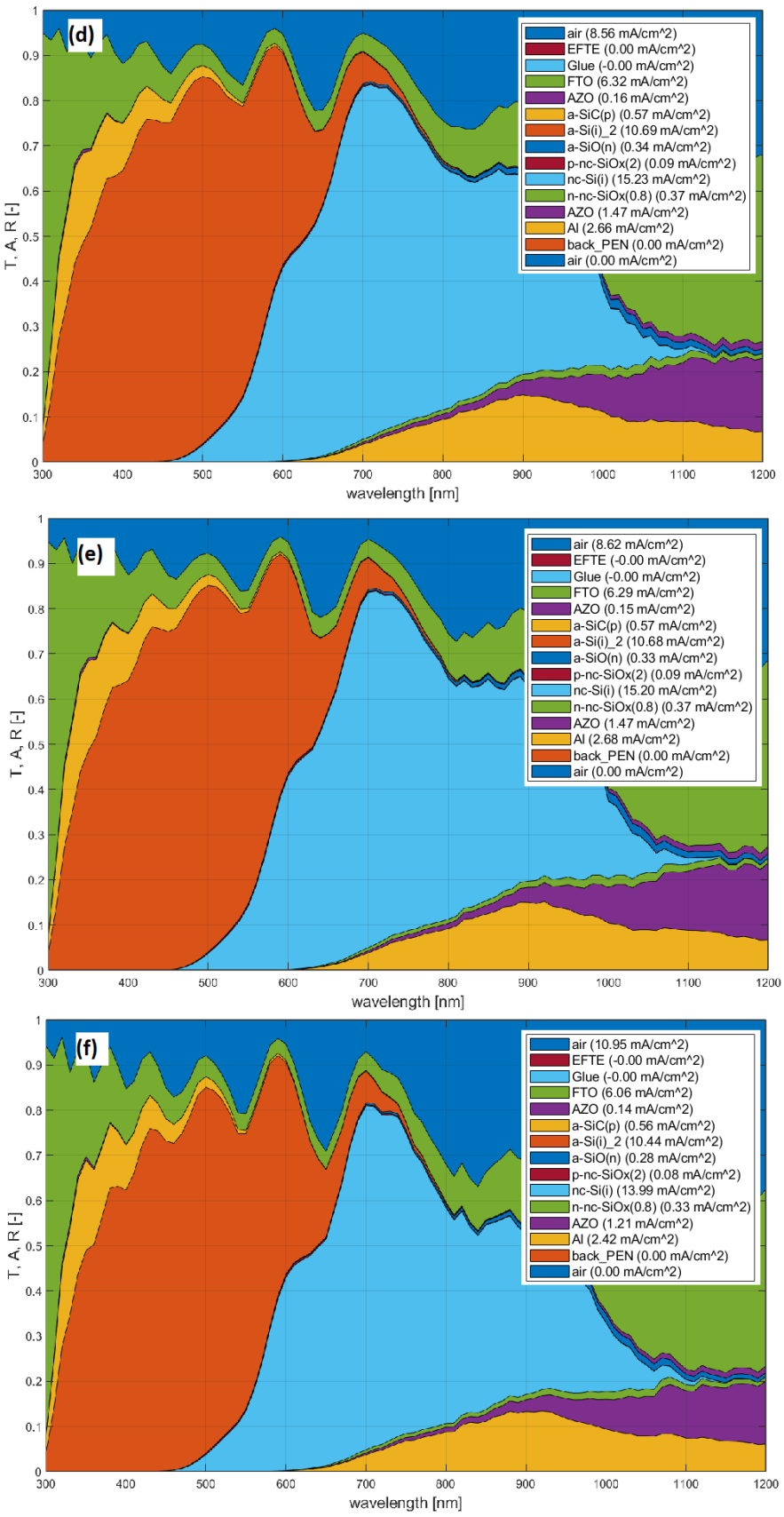
(d)
air (8.56 mA/cm^2)
EFTE (0.00 mA/cm^2)
Glue (-0.00 mA/cm^2)
FTO (6.32 mA/cm^2)
AZO (0.16 mA/cm^2)
a-SiC(p) (0.57 mA/cm^2)
a-Si(i)_2 (10.69 mA/cm^2)
a-SiO(n) (0.34 mA/cm^2)
p-nc-SiOx(2) (0.09 mA/cm^2)
nc-Si(i) (15.23 mA/cm^2)
n-nc-SiOx(0.8) (0.37 mA/cm^2)
AZO (1.47 mA/cm^2)
Al (2.66 mA/cm^2)
back_PEN (0.00 mA/cm^2)
air (0.00 mA/cm^2)
T, A, R [-]
wavelength [nm]
(e)
air (8.62 mA/cm^2)
EFTE (-0.00 mA/cm^2)
Glue (-0.00 mA/cm^2)
FTO (6.29 mA/cm^2)
AZO (0.15 mA/cm^2)
a-SiC(p) (0.57 mA/cm^2)
a-Si(i)_2 (10.68 mA/cm^2)
a-SiO(n) (0.33 mA/cm^2)
p-nc-SiOx(2) (0.09 mA/cm^2)
nc-Si(i) (15.20 mA/cm^2)
n-nc-SiOx(0.8) (0.37 mA/cm^2)
AZO (1.47 mA/cm^2)
Al (2.68 mA/cm^2)
back_PEN (0.00 mA/cm^2)
air (0.00 mA/cm^2)
T, A, R [-]
wavelength [nm]
(f)
air (10.95 mA/cm^2)
EFTE (-0.00 mA/cm^2)
Glue (-0.00 mA/cm^2)
FTO (6.06 mA/cm^2)
AZO (0.14 mA/cm^2)
a-SiC(p) (0.56 mA/cm^2)
a-Si(i)_2 (10.44 mA/cm^2)
a-SiO(n) (0.28 mA/cm^2)
p-nc-SiOx(2) (0.08 mA/cm^2)
nc-Si(i) (13.99 mA/cm^2)
n-nc-SiOx(0.8) (0.33 mA/cm^2)
AZO (1.21 mA/cm^2)
Al (2.42 mA/cm^2)
back_PEN (0.00 mA/cm^2)
air (0.00 mA/cm^2)
T, A, R [-]
wavelength [nm]

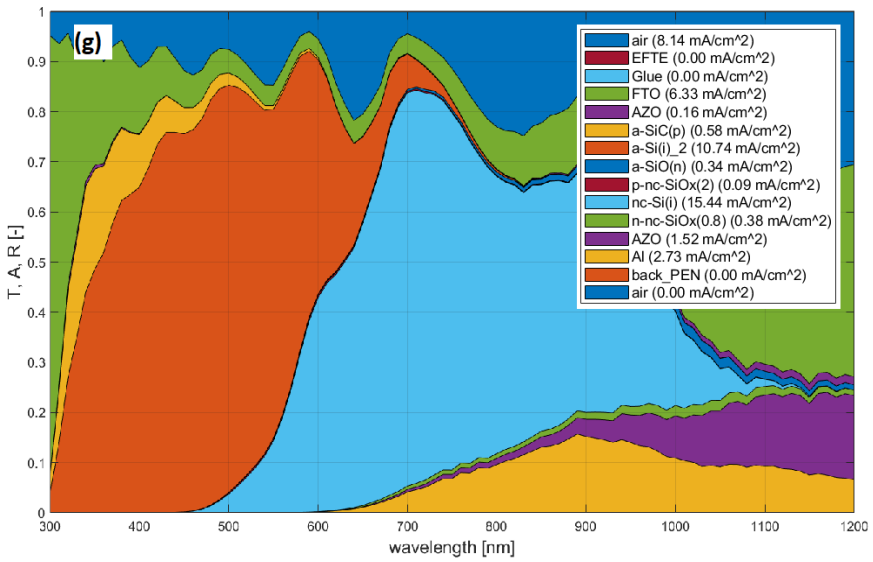

Appendix 7.32: GenPro simulation results for a-Si:H/nc-Si:H tandem cell with (a) no texturing (b) factory baseline (c) KOH60 (d) KOH70 (e) NaOH70 (f) test run (g) test run Al+FTO